Department of Physics and Astronomy

University of Heidelberg

Bachelor Thesis in Physics

submitted by

Álvaro Lozano Onrubia

born in Madrid (Spain)

2018

Vacuum ultraviolet spectroscopy of highly charged oxygen ions

This Bachelor Thesis has been carried out by lvaro Lozano Onrubia

at the Max Planck Institute for Nuclear Physics in Heidelberg

under the supervision of

Priv.-Doz. Dr. José Ramón Crespo López-Urrutia

Abstract

Spectroscopic observations constitute a very powerful means to inquire about diverse phenomena of fundamental physics. From research about a possible spatial variation in the fine-structure constant value to the benchmarking of astrophysical observations that may shed light on star formation and evolution - the application range of spectroscopy is wide and diverse. Spectroscopy of highly charged ions in electron beam ion traps (EBITs) in particular draws special attention due to the contributions that many yet uncharted ionic spectra can provide to many areas of physics. In this work, a recently installed 3-meter normal incidence monochromator spectrometer was commissioned at the FLASH-EBIT that opens the previously inaccessible range of 30-200 nm. The present measurements of oxygen spectra up to O^{4+} provide a calibration and a resolution analysis necessary to obtain viable data. Line identification of oxygen states up to O^{4+} served as a check of the achieved precision. Lastly, the identification of O^{5+} lines was also strived for.

Zusammenfassung

Spektroskopische Beobachtungen stellen ein mächtiges Mittel dar, um diverse Phänomene von fundamentalem physikalischem Interesse zu untersuchen. Von der Forschung einer möglichen räumlichen Variation im Wert der Feinstrukturkonstante bis zur Referenzbildung für astrophysikalische Beobachtungen, die Licht werfen könnten auf Sternentstehung und -entwicklung - die Anwendungsreichweite von Spektroskopie ist breit und divers. Spektroskopie hochgeladener Ionen in Elektronenstrahl-Ionenfallen (EBITs) zieht besondere Aufmerksamkeit auf sich aufgrund der Beiträge, welche die vielen noch unbekannten ionischen Spektren in vielen Bereichen der Physik leisten können. In dieser Arbeit wurde ein kürzlich installierter 3-Meter-Normalinzidenzmonochromator an der FLASH-EBIT beauftragt, der den zuvor unzugänglichen Bereich zwischen 30-200 nm aufdeckt. Die gegenwärtigen Messungen von Sauerstoffspektren bis hin zu O^{4+} erlaubten eine Kalibration und eine vorläufige Auflösungsvermögen-Analyse, notwendig um brauchbare Daten zu erhalten. Die Linienidentifikation von Sauerstoff bis zum Ladungszustand O^{4+} diente als Überprüfung der erreichten Genauigkeit. Zuletzt wurde auch die Identifikation von O^{5+} Linien angestrebt.

Contents

1 Introduction

Often at the heart of scientific breakthroughs when not an object of study in itself, electromagnetic radiation has been crucial to the development of science and its methods.

Newton's experiments with light (1672) form an important milestone in physics and started to shape our modern understanding of electromagnetic radiation, showing that a prism could split a ray of light into a *spectrum* (*lat.*, image, apparition) of components just like in a rainbow [1]. It would take until the 19$^{\text{th}}$ century for Joseph von Fraunhofer to apply his knowledge in optical lens manufacturing to delve into a thorough study of the solar spectrum. His efforts resulted in a further milestone, already foreshadowed by Wollaston's observations (1802) [2, 3]: the discovery of the so-called *Fraunhofer lines*, which consist in a series of dark bands in the otherwise continuous black-body spectrum of the Sun. Almost half a century later, Bunsen and Kirchhoff realized that these bands match with the emission lines of heated elements led to an ultimately correct conclusion: the Fraunhofer lines result from the absorption of light by elements in the solar atmosphere [4]. In such a way, spectroscopy as the study of the interaction between matter and electromagnetic radiation was formally born. As a relatively young scientific discipline, it was yet to yield its most impressing results. In particular, the discovery of hydrogen's discrete emission spectrum - Balmer (1885), Paschen (1908), etc. - resulted in a series of atomic theories from which quantum mechanics would ultimately emerge in the dawn of the 20$^{\text{th}}$ and change our understanding of nature at its most fundamental level [5, 6].

In more recent times, spectroscopy has kept its prominent role in providing discoveries and benchmarking observations. In this aspect, electron beam ion traps (EBITs) have proven to be a valuable asset. First developed by Morton Levine and Ross Marrs, EBITs are devices which not only permit the creation of highly charged ions (a feat already achieved by the predecessor, the electron beam ion source) but also allow for direct spectroscopic analysis of the ions [7]. Since the first EBIT was built at Livermore, the construction of several others ensued all over the world. One of the newer devices is the FLASH-EBIT, currently at the Max Planck Institute of Nuclear Physics in Heidelberg.

One specific branch of physics that has profited from spectroscopical research has been astrophysics, where some of its uses have been the measurements of the dark matter content in a galaxy, the masses of galaxy clusters or the rate of expansion of the Universe [8]. In particular, spectroscopy has been employed to analyze stars and nebulae for chemical composition and temperatures, which has yielded clues about star formation and evolution. A paradigmatic example

of the latter is the detection of technetium (Z=43) in the atmospheres of red giants [9]. Tc is the lightest element with no stable isotopes, with a greatest half-life of 4.2 million years for ^{99}Tc. Red giants however constitute one of the last evolutionary stages of stars and are much older. This rules out the possibility of finding technetium dating from the early stages of the stellar life cycle. The detection of this element in red giants therefore suggests that even in evolved stars, s-process nucleosynthesis processes resulting in technetium still occurs.

This hypothesis would explain the overabundance and "unusually rich diversity" of trans-iron elements [10] (see Fig.1). In this context, the finding of technetium may as well shed light the unusual hydrogen-deficiency in objects like the He-rich white dwarf [11] RE 0503-289, discovered by Barstow *et al.* in 1994 [12].
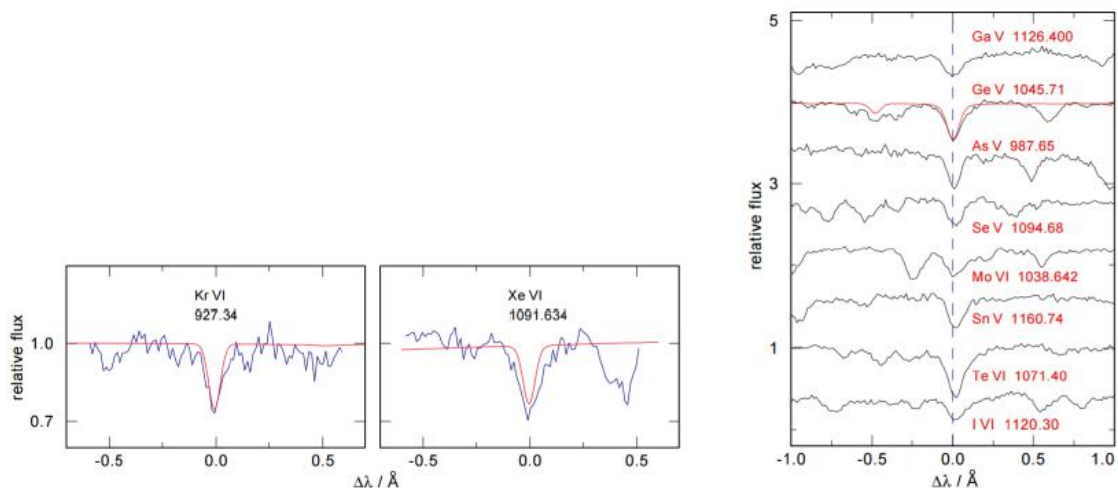

Figure 1: To the left, detected Kr^{5+} and Xe^{5+} lines (blue) plotted against theoretical models (red). To the right, a depiction of detected lines of up to eight trans-iron elements in the star RE 0503-289 (from [10]).

RE 0503-289 belongs to a fraction of stars beyond the asymptotic giant branch ("post-AGB stars", as in [13]) whose evolution took a different path than the usual one. Instead of experiencing a cooldown after the end of the H-shell and He-shell burning, the progenitor star of RE 0503-289 may have been able to resume He-shell burning in what is known as a late helium-flash. This renewed activity is thought to underlie the mixing into deeper layers and burning of remaining surface hydrogen, causing the abnormal hydrogen-deficiency. Another effect of the

late He-flash would be the dredging-up of heavy trans-iron elements from internal layers of the star into the surface, making their spectra accessible to astronomical observations [10]. Whereas these observations strongly suggest the occurrence of the late helium-flash, the detection of technetium ions in RE 0503-289 would be a conclusive proof.
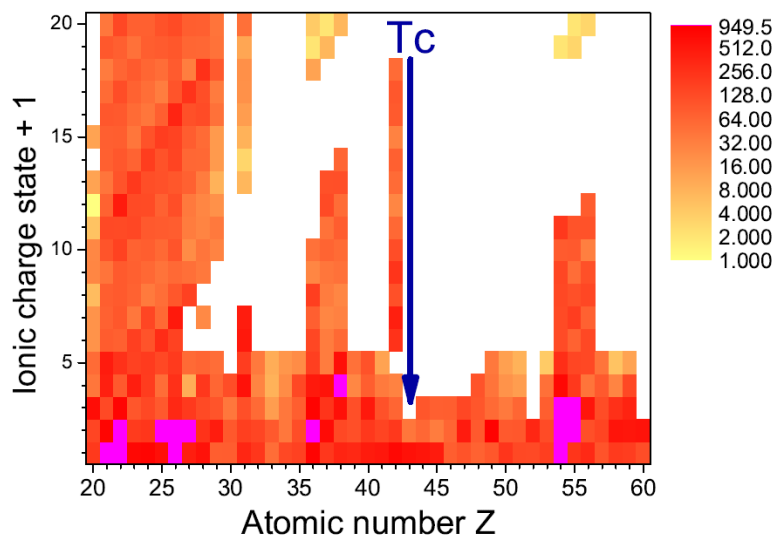

Figure 2: Representation of "sea of ignorance" that the spectra of many trans-iron ions constitute. The number of known lines per species is noted by the coloured rectanges. In white, the charged states for which no data are available so far (from [13]).

The use of technetium as an indicator for a late helium-flash occurrence entails a practical problem: atomic data of the element are so far incomplete, especially for the charged states Tc^{3+}-Tc^{6+} expected on the hot surface of the star. This problem is not unique to technetium, "since the few HCI spectroscopy groups have mostly focused their efforts on the highest possible charge states in few-electron systems" ([13]). Hence, the technetium species expected on the star surface are still uncharted territory (Fig.2). Without a precise knowledge of energy levels, line positions and oscillator strenghts in the ultraviolet regime it is not possible to identify the element.

As a means of filling the gap in knowledge about highly charged technetium transitions it has been suggested to perform spectroscopic measurements on the element under laboratory

conditions. In this context, EBITs constitute a very promising setup to provide the missing data needed in the ultraviolet regime. Previous measurements with an extreme ultraviolet spectrometer attached to the EBIT allowed for data intake up to a wavelength of 30 nm, which is clearly insufficient (Fig.3). The updated setup of the FLASH-EBIT, with the latest addition of a 3 m normal incidence monochromator spectrometer, would allow for spectroscopic measurements in the range between 30 nm and 200 nm. However, any planned measurements with this setup require a previous study of its properties. In particular, a reliable calibration and a resolution analysis are mandatory in order to obtain viable data. Facing this challenge successfully is the principal aim of this thesis.
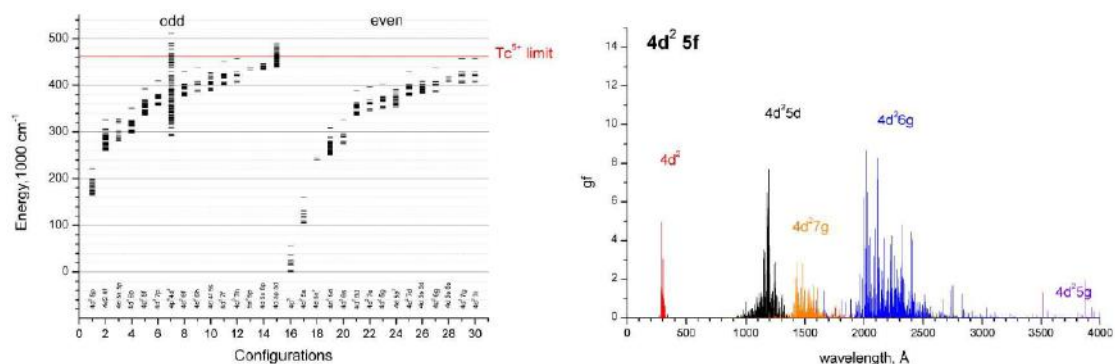

Figure 3: To the left: representation of the energy levels of Tc^{5+}. To the right: lines associated to the transition between the levels [13].

A way of corroborating the goodness of the setup and the chosen calibration is by line comparison of well-studied elements like oxygen with corresponding literature values. Furthermore, any new data on uncharted transitions would constitute a huge success and a valuable addition to existing databases.

Outline of the thesis

The experiments analyzed and discussed in this Bachelor thesis provide a first setup for planned technetium, ruthenium and iridium measurements in a region of the vacuum-ultraviolet (VUV) regime still uncharted and of extreme interest. A calibration of the 3 m monochromator performed by measuring oxygen spectra is proposed, whereas a resolution analysis showcases the goodness of the setup in the time span between November 2017 and January 2018. As a test

of the setup, line identification of oxygen lines up to O^{4+} was performed. The structure of this thesis is presented below:

- Chapter 2 contains a brief introduction into atomic physics and electronic transitions. The basic theory needed in order to understand the physics of the experiment is presented. This includes brief recapitulations of the selection rules and the main processes of atomic ionization and excitation, as well as a short foray into the shape of spectral lines.

- Chapter 3 consists in a detailed description of the setup employed to detect the oxygen spectra. The major components of the FLASH-EBIT and the VUV spectrometer are introduced.

- Chapter 4 details the measurements performed in order to establish the proposed setup.

- Chapter 5 addresses the oxygen spectra that form the core of this thesis, including a discussion of the calibration procedure.

- Chapter 6 provides a thorough analysis of the resolution of the setup.

- In chapter 7, the measured oxygen lines are listed and compared with literature values. The first part delves into the lines that were easily identified up to O^{4+}. The second part discusses the lines that were identified after a more thorough analysis, including proposals of O^{5+} lines and peaks originating from impurities in the setup.

- Chapter 8 summarizes the results of the measurements.

2 Theory

2.1 Hydrogen atom

The quantum mechanical description of the hydrogen atom is one of the milestones in modern physics and paved the way for a whole new way of looking at nature. Consisting of one proton and one electron, the hydrogen atom constitutes essentially a two-body system and is therefore one of the few that can be solved analytically.

In order to describe the state of a quantum mechanical system, one makes use of the so-called *wavefunction* $\Psi(\mathbf{r}, t)$, with the position vector $\mathbf{r}$ and the time t. A very special interpretation is assigned to this wavefunction: it is a probability amplitude that, when squared, provides the probability of a system being in the state $\Psi(\mathbf{r}, t)$ describes. In order to obtain $\Psi(\mathbf{r}, t)$, one has to solve the eigenvalue problem posed by the famous Schrödinger equation,

$$H\Psi(\mathbf{r}, t) = E\Psi(\mathbf{r}, t), \tag{1}$$

where H is the Hamiltonian of a system and E the energy of the system. A solution of the hydrogen system requires the knowledge of its Hamiltonian, which is given by

$$H = \frac{-\hbar^2}{2m_e}\overrightarrow{\nabla}^2 - \frac{Ze^2}{4\pi\epsilon_0 r}, \tag{2}$$

with $r := |\mathbf{r}|$ as the distance between nucleus and electron, e the elementary charge, ϵ_0 the electric permeability, m_e the mass of the electron and $-\hbar^2\overrightarrow{\nabla}^2$ the square of the momentum operator $\hat{p} = -i\hbar\overrightarrow{\nabla}$. This Hamiltonian describes the behaviour of the system: the first part encodes the kinetic energy of the electron with respect to the nucleus, while the second part models the Coulomb interaction between the elementary charge of the electron e and the charge of the nucleus Ze, where Z represents the number of protons. For hydrogen, $Z = 1$ holds.

The isotropy of the system is crucial: the rotational symmetry it entails allows to separate the wavefunction into a radial part $R(r)$ and an angular part $Y(\theta, \phi)$, such that

$$\Psi(r, \phi, \theta) = R(r) * Y(\phi, \theta) \tag{3}$$

with ϕ and θ describing the azimuthal and polar angles in spherical coordinates. $Y(\phi, \theta)$ represents the spherical harmonics of the system. Since $\overrightarrow{\nabla}^2$ entails no derivatives with respect to any of the angles, the leftover is essentially a one-dimensional problem where the distance r carries all the dependency. The solutions are energy eigenstates of the Hamiltonian given by

$$E_n = -R_y \frac{Z^2}{n^2}, \tag{4}$$

with the Rydberg constant

$$R_y = \frac{m_e e^4}{8h^2 \epsilon_0^2} \tag{5}$$

and the *principal quantum number* n any natural number except zero. Once again, $Z = 1$ holds for hydrogen. For hydrogen-like ions, i.e. ions with one valence electron, the absolute value of E_n increases quadratically with the number of protons in the nucleus. However, the increased number of electrons, especially in ions with more than one valence electron, makes calculations more inexact - closed analytical solutions are precluded, and computational methods need to be applied in order to solve the Schrdinger equation. Despite this circumstance, predictions about energy levels and electronic transitions between them can still be made for multi-electron systems.

2.2 Selection rules

A powerful theoretical tool to make predictions about transitions for all kinds of electronic configurations consists in the so-called selection rules. Selection rules arise from the calculation of the transition moment integral M_{if}, whereof the square corresponds to the probability of a transition from an initial state Ψ_i to a final state Ψ_f. Using the appropriate transition moment operator μ, M_{if} is defined as

$$\int_{\mathbb{R}^3} \Psi_f^*(\mathbf{r}) \mu \Psi_i(\mathbf{r}) d^3 r. \tag{6}$$

Transitions where μ equals the dipole moment operator are especially important, since the electric dipole is the dominant means of interaction between a bound electron and an electromagnetic field. If $M_{if} = 0$ for the electric dipole, the transition is deemed (electric dipole) *forbidden*. Forbidden transitions may still occur by means of higher order electric multipole moments, usually at comparatively low rates. Magnetic multipole interactions may as well channel transitions not allowed otherwise, and vice versa.

Selection rules impose constraints, essentially "selecting" which transitions may take place. In this sense, they constitute shortcuts by which to find out if the probability of a transition vanishes or not. They make use of the properties of the implicated wave functions, which in multi-electron systems greatly depend on the following quantum numbers:

- total Azimuthal quantum number L,

- total spin quantum number S,

- total angular momentum quantum number $J = L + S$,

- projection of the total angular momentum M_J.

Another characteristic of wave fuctions is their parity π, which describes the behaviour of the former under a flip in the sign of the spatial coordinates. If the overall sign of the wave function flips as well, then the initial parity π_i changes to $\pi_f = -\pi_i$. The change in parity, or lack thereof, is also regarded by the selection rules, a summary of which is presented in Tab.1.

Table 1: Rigorous selection rules for the electric and magnetic dipoles and the electric quadrupole [14].

	El. dipole (E1)	Mag. dipole (M1)	El. quadrupole (E2)
ΔJ	$0, \pm 1$	$0, \pm 1$	$0, \pm 1, \pm 2$
	(no $0 \leftrightarrow 0$)	(no $0 \leftrightarrow 0$)	(no $0 \leftrightarrow 0, 1$; no $\frac{1}{2} \leftrightarrow \frac{1}{2}$)
ΔM_J	$0, \pm 1$	$0, \pm 1$	$0, \pm 1, \pm 2$
Parity change	yes	no	no

2.3 Processes in an electron beam ion trap

An electron beam ion trap (EBIT) allows to induce certain atomic processes; it is the detection of electromagnetic radiation emitted during some of these processes that makes it possible to recover information and infer on the electronic transitions of ions. In this section the most relevant processes for our purposes, of which a visual representation can be found in 4, will be summarized.

- **Induced and spontaneous transitions**

  An atom with an electron at an energetic state E_{g} in an electromagnetic radiation field may absorb energy and end up in an excited energetic state. This is achieved by absorption of a photon of frequency ν; simultaneously, an electron is promoted to a quantum state energetically higher to its ground state by $E_{\gamma} = h\nu$, h being the Planck constant. In total, the energetic state of the atom after absorption is given by

  $$E_{\mathrm{e}} = E_{\mathrm{g}} + h\nu = E_{\mathrm{g}} + E_{\gamma}, \tag{7}$$

  where g and e stand for the ground and the excited state, respectively.

  Let us assume the radiation field to have a spectral energy density given by

  $$\omega_{\nu}(\nu) = n(\nu)h\nu, \tag{8}$$

  where $n(\nu)$ is the number of photons per volume in the unit interval of ν. In that case, the probability for a spontaneous absorption corresponds to

  $$W_{\mathrm{eg}} = B_{\mathrm{eg}}\omega_{\nu}(\nu). \tag{9}$$

  B_{eg} is called the Einstein coefficient for absorption.

  Emission of photons fundamentally occurs in two different ways: it can be induced, but it can also happen spontaneously.

  An excited atom of energy E_{e} in a radiation field may serve as a scattering partner for a photon. The process may happen such that a second photon of the same energy is emitted into the same direction as the scattered photon by the now de-excited atom at

state E_g. Simultaneously, an electron is degraded to an energetically lower quantum state. The energy of the emitted photon is given by

$$E_{\gamma,\text{emitted}} = h\nu = E_e - E_g = E_{\gamma,\text{scattered}}. \tag{10}$$

The probability for this process is given by

$$W_{eg} = B_{eg}\omega_\nu(\nu), \tag{11}$$

where B_{eg} is the Einstein coefficient for induced emission. The probability for spontaneous emission, corresponding to the spontaneous demotion of an excited electron in an atom to a lower state, is given by

$$W_{eg}^{\text{sp}} = A_{eg}, \tag{12}$$

where A_{eg} is the Einstein coefficient for spontaneous emission [15]. It should be noted that, as opposed to for induced emission, the spontaneous process is isotropic, i.e. the direction of emitted photons is unconstrained.

For the sake of completeness it may be useful to know the relations between the different Einstein coefficients. These are given by

$$B_{eg} = \frac{g_g}{g_e}B_{ge} \tag{13}$$

and

$$A_{eg} = \frac{8\pi h\nu^3}{c^3}B_{eg}, \tag{14}$$

with $g = (2J+1)$ corresponding to the number of degenerate sub-levels of the states e and g [15].

- **Photoionisation**

Photoionisation is the ultimate stage of the excitation process described above. When an electron bound by the energy I_p interacts with an incoming photon γ of energy $E_\gamma \geqslant I_p$, the former can escape the binding potential of the nucleus. Schematically, the process is described by:

$$\mathrm{A}^{q+} + \gamma \rightarrow \mathrm{A}^{(q+1)+} + \mathrm{e}^-. \tag{15}$$

To photoionize already highly charged ions, very energetic photons in the UV and X-ray domain are necessary.

- **Radiative recombination**

  When a free electron with kinetic energy E_e is captured by an ion with an ionization potential I_p, a photon of energy $h\nu = E_e + I_p$ is emitted. This process, which can be written as

  $$A^{q+} + e^- \to A^{(q-1)+} + \gamma, \tag{16}$$

  and understood as time-reversed photoionisation, is called radiative recombination (RR).

- **Dielectronic recombination**

  Dielectronic recombination (DR) occurs when a free electron is captured by the nucleus potential of an ion while one of its bound electrons is promoted to an excited state. The instability of the latter prompts the demotion of the electron to its ground state all while a photon is emitted:

  $$A^{q+} + e^- \to [A^{(q-1)+}]^{**} \to A^{(q-1)+} + \gamma. \tag{17}$$

  With E_e as the kinetic energy of the free electron and I_p as the ionization potential, energy conservation requires that

  $$E_e + I_p = \Delta E_{eg} = h\nu, \tag{18}$$

  where ΔE_{eg} corresponds to the energy difference between the state e with an excited second electron and the ground state g. This constraint defines dielectronic recombination as a resonant process.

- **Electron impact excitation**

  We call electron impact excitation the process by which a free electron with kinetic energy $E_{e,1}$ excites an ion by promoting one of its electrons to a higher state. Albeit with an energy $E_{e,2} \leqslant E_{e,1}$, the first electron remains free. The bound electron is demoted to a lower state, while as a last step it prompts the emission of a photon:

  $$A^{q+} + e^- \to [A^{q+}]^* + e^- \to A^{q+} + \gamma + e^-. \tag{19}$$

  The requisite for this process is that the initial kinetic energy of the free electron be larger than the energy difference between the excited ion and its ground state.

14

Electron impact excitation is the main excitation process in an EBIT. The kinetic energy of the beam electrons can be adjusted to allow for different ions and transitions with energy intervals up to the kinetic energy of the beam. By statistics alone, most if not all of the accessible states are induced - the typically high density of states and the variety of different electron impacts guarantees this. Predictions of the distribution of state occupation numbers are usually provided by collisional radiative models. Experimentally, it is the (relative) intensities of the different peaks in the detected spectra which yield information about these distributions.

- **Electron impact ionisation**

Electron impact ionisation is the process by which a free electron with sufficient kinetic energy E_e ionizes an atom through collision with one of its bound electrons. This is only possible if E_e is greater than the ionisation potential I_p of the bound electron. Energy conservation then demands

$$E_\mathrm{e} - I_\mathrm{p} = E_1 + E_2, \tag{20}$$

where E_1 and E_2 are the energies of the two electrons after the scattering process. Schematically, we can express it as

$$\mathrm{A}^{\mathrm{q}+} + \mathrm{e}^- \rightarrow \mathrm{A}^{(\mathrm{q}+1)+} + 2\mathrm{e}^-. \tag{21}$$
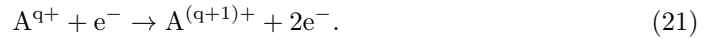
This is the main process by which atoms are ionized in an EBIT. EBITs are capable of producing highly charged ions (HCIs), which - the lack of a clear and delimitating definition notwithstanding [16] - consist of a positively charged nucleus surrounded by relatively few electrons. In order to tag the ions, the typical nomenclature can be employed, where an ion A with a positive charge q is expressed by $A^{(\mathrm{q}+)}$. However, there exists a second traditional spectroscopic nomenclature which may be encountered in the literature: the charge q of the ion is expressed in Roman numerals by the number equivalent to (q + 1). This implies that a neutral atom, e.g. neutral oxygen, is displayed as O I.
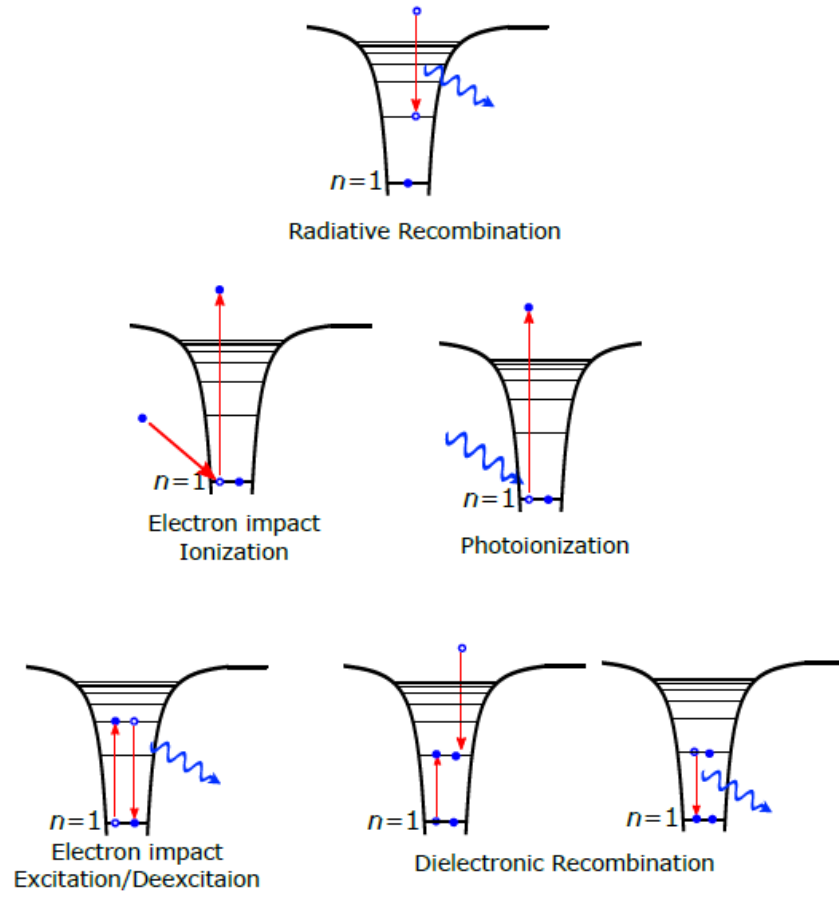
Figure 4: Representation of the processes in an electron beam ion trap (modified from [17]).

2.4 Shape and width of spectral lines

The core of this thesis consists in the analysis of spectral lines, therefore it is only natural to consider their features. While the most important aspect may be the position of a line in a spectrum, line shape and width play an important role in spectroscopy as well.

Observed line widths are the result of, at least, three different physical processes. The most fundamental one, from which the so-called *natural line width* arises, is due to quantum mechanical uncertainty. The finite life time τ_j of any state j entails a finite energy width $\delta E = \frac{\hbar}{\tau_j}$. For any transition of radiative nature between states i and k, this implies an uncertainty in the photon frequency of

$$\delta\nu_{ik} = \frac{\delta E_i + \delta E_k}{h},\tag{22}$$

with the line following a marked Lorentzian profile [15]. If no other effects were at play, this would be the minimal width possibly measurable.

Another effect to take into account is the Doppler broadening arising from the kinematics of the atoms involved. For a radiation emitting atom, the emitted frequency as seen by the observer is given by

$$\omega_e = \omega_0 + \mathbf{k} * \mathbf{v},\tag{23}$$

with ω_0 being the frequency in the rest frame of the atom, $\mathbf{v}$ and $\mathbf{k}$ the velocity and wave vectors in the observer's frame, respectively. Incidentally, the absorption frequency is the same, hence $\omega_a = \omega_e$. If we further model the emitting substance as a gas in thermal equilibrium, we can apply Maxwell's velocity distribution to gain some insight into how the statistics at play affect a spectral line at ω_0. In first order and at a finite temperature T, these yield an unshifted Gaussian of the width

$$\delta\omega_D = \frac{\omega_0}{c}\sqrt{\frac{8k_B T \ln 2}{m}},\tag{24}$$

where we used the Boltzmann constant k_B and the mass m of the atoms.

Finally, there exists the so-called collisional line broadening that results from the interactions between atoms. These enforce slight shifts - positive as well as negative - in the energy levels of the electrons which do not fundamentally change the Lorentzian shape of an emission line, but however increase its width. This is only natural, as the additive contribution to the transition probability due to atomic interactions increases monotonously with the number of interactions. When all of these processes make a significant contribution, the result is the so-called *Voight profile*. Mathematically, it follows from the convolution of the Gaussian and the Lorentzian contributions to the line shape. This can also be retraced in the final profile: while the tip is

typically Gaussian, towards the sides the curve takes on a more Lorentzian descent [18].
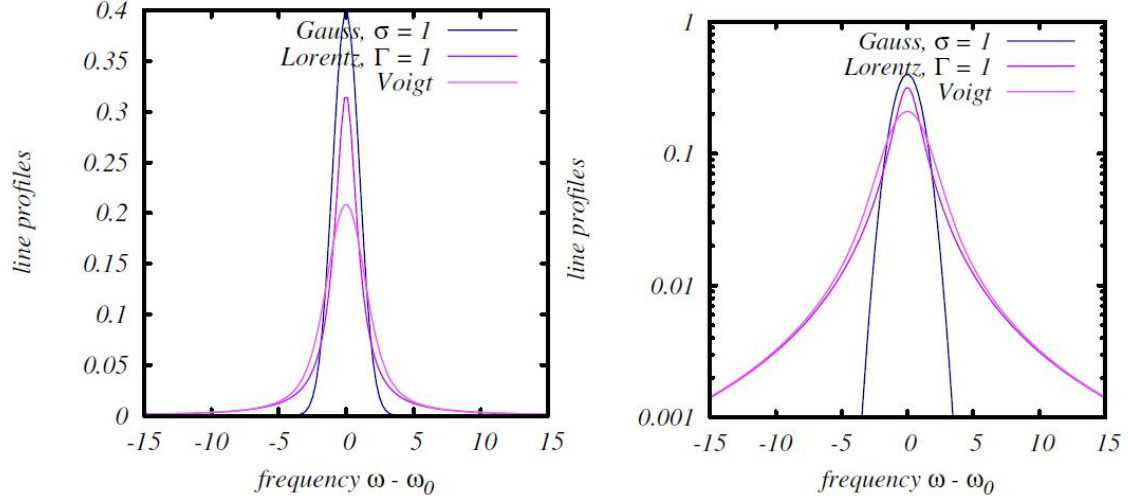

Figure 5: Representation of the Gauss, Lorentz and Voigt profiles as a function of the angular frequency difference $\omega - \omega_0$. A decay rate Γ and a Gaussian width σ of 1 in arbitrary units were employed [18].

In spite of these very fundamental contributions to line shape, in the end our observations are limited by the resolving power of the setup. It is this factor which results in measurements of typically Gaussian-like peaks. This will be of relevance later on, since it justifies the use of Gaussians for the fitting procedures to the lines in the data analysis section.
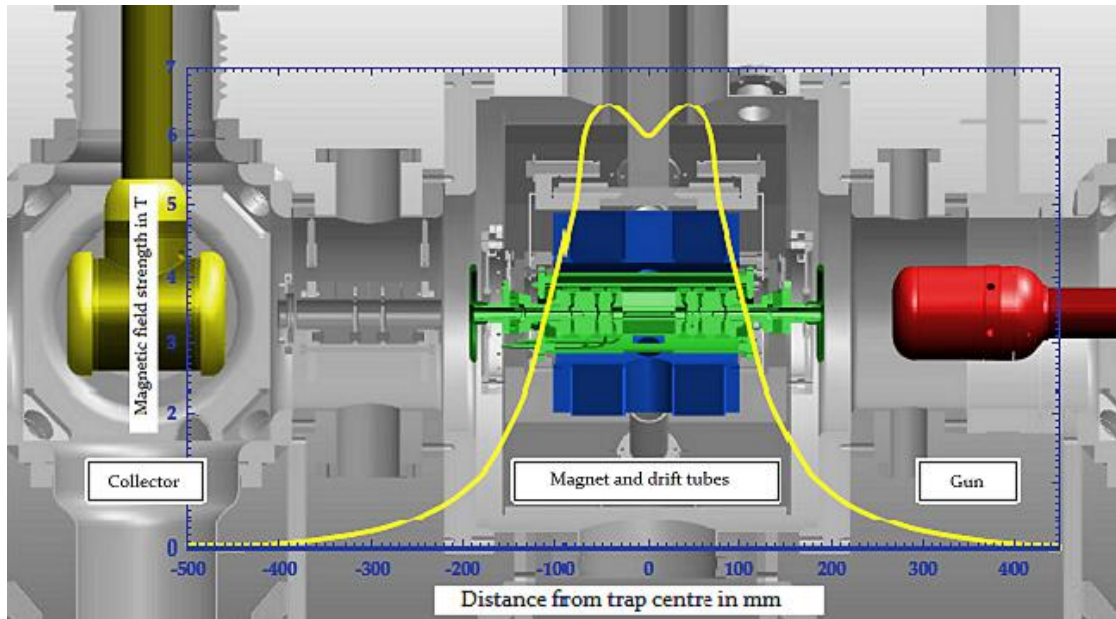
3 Experimental setup

Figure 6: Representation of an EBIT with some of its notable components and features (from [19]).

3.1 Electron beam ion trap

All of the measurements carried out for this thesis were performed on an electron beam ion trap (EBIT) at the Max Planck Institute for Nuclear Physics in Heidelberg (see Fig.6). Unlike its predecessor the EBIS (short for electron beam ion source), the EBIT not only allows the creation of an ionizing electron beam but is also designed to trap the ions produced in its interior and permits their observation. The electrons for the beam are generated in the electron gun. The magnet chamber allows to focus them, thus creating a tightly focused beam which is finally captured by the collector. In the trap, the space charge potential of the electron beam traps the ions radially. The axial electrostatic trapping potential is provided by the drift tubes (see Fig.7).
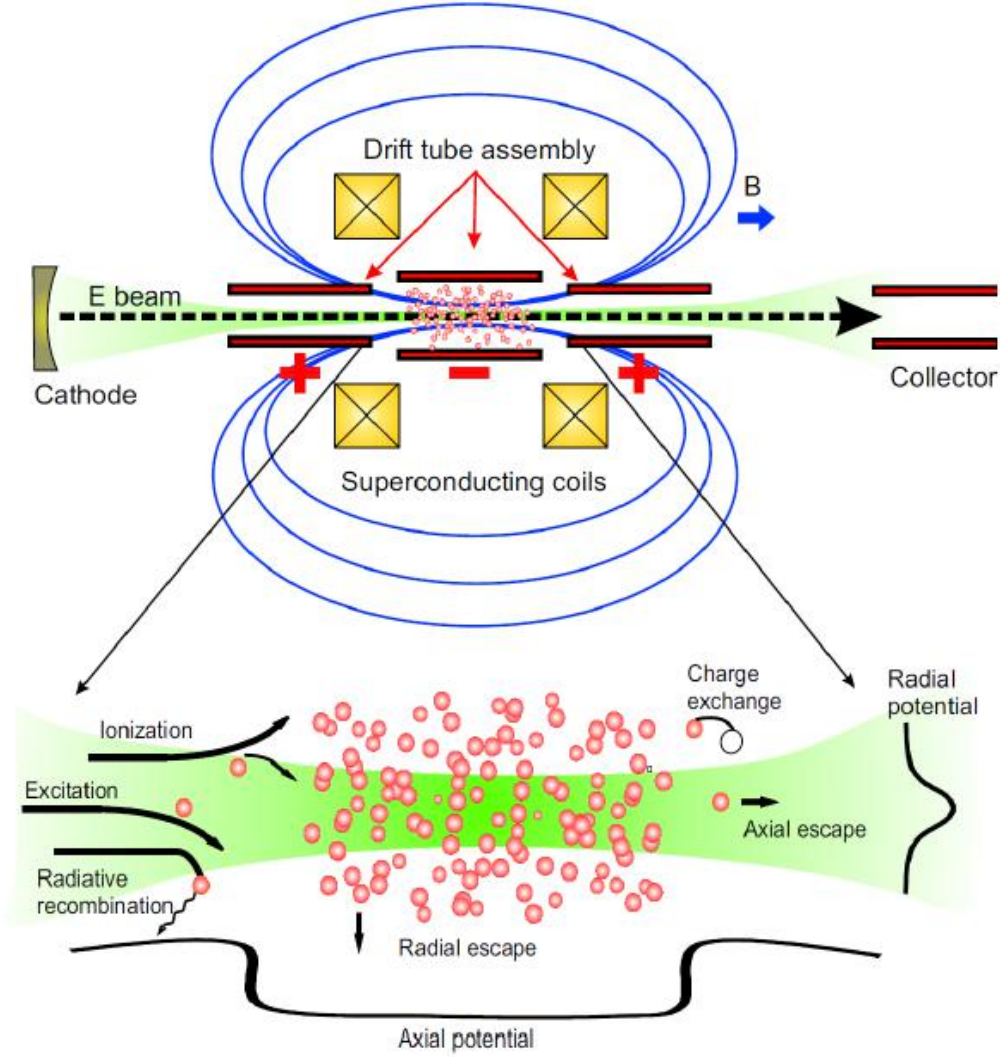
Figure 7: Schematic visualization of the EBIT and its axial potential. Furthermore, the processes taking place in its interior are displayed (from [20]).

3.1.1 Electron gun

The process by which electrons are emitted from the cathode is thermo-ionic emission in the so-called electron gun (Fig.8). This is achieved by heating the cathode, made out of a porous tungsten matrix containing barium, to between 1300 K and 1500 K. It is then the combined electric field of the anode and the focus electrode present in the gun which has the task of pulling away the electrons from from the cathode surface. At this stage it is necessary to cancel

out external magnetic fields, such as the magnetic field needed for the focusing of the electron beam. In order to do this, a set of trimming and bucking coils neutralizing any external fields with their own magnetic field were built in surrounding the cathode [21]. Another feature of the electron gun are its own vacuum chamber, which allows any kind of operations in the rest of the EBIT (e.g. additional mountings or changes of components) without disrupting the vacuum in the gun [19].
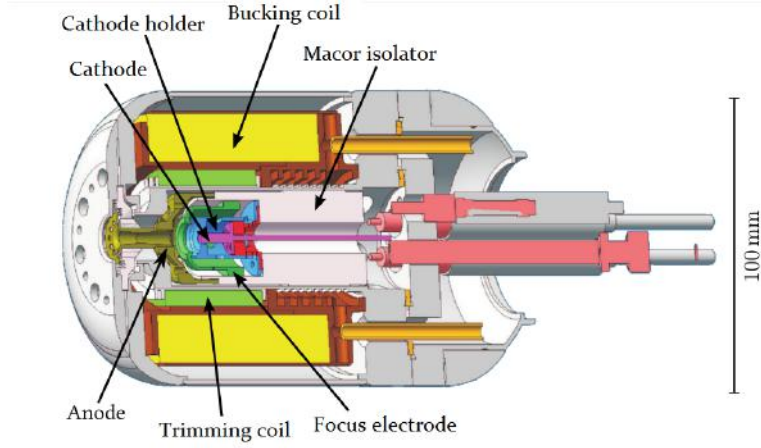

Figure 8: Sketch of the electron gun showing the different components that allow for a straight electron beam [22].

3.1.2 Ion trap

The ion trap is the distinctive feature of the EBIT. It consists primarily of nine drift tubes cylindrical in shape (see Fig.9). These are enclosed by superconducting Helmholtz coils (made of Nb_3S by the company Cryogenics), which focus the electrons into a beam width of less than $50\,\mu m$ [23]. The negative space charge of this electron beam is the source of the radial trapping potential. Although slightly at the cost of the homogeneity of the magnetic field, the disposition of the Helmholtz coils was chosen such that radial access to the trap was enabled. Seven slits were drilled into the magnetic chamber of the trap to allow for visual access (Fig.10).

The drift tubes (Fig.9) form the axial part of the trap, the strength of the confinement depending on the voltage at which they are set. Collectively they can reach a voltage of up to $30\,kV$; however, they may also be varied individually, thus allowing to create trapping potentials of different shapes with depths and gradients as required for each measurement. Of the nine drift
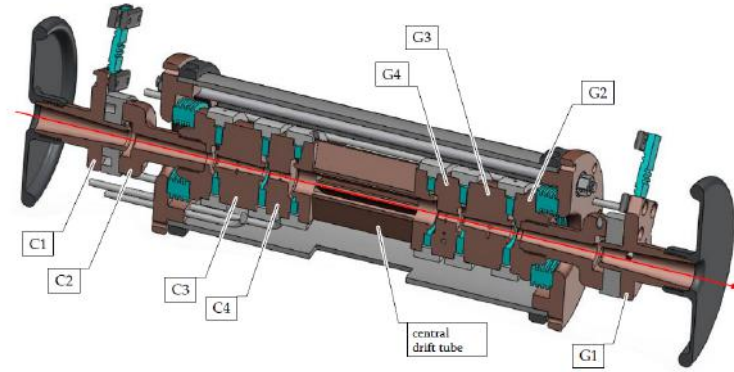
Figure 9: Axial sectional representation of the drift tubes. The electrodes closer to the gun are labeled as G1 to G4, those on the collector side as C1 to C4. The electron beam is emitted at the gun and decelerated at the collector, i.e. the electrons travel from right to left in this picture [19].

tubes, the central one plays a special role. It possesses eight slits which may be aligned with the priorly discussed apertures in the magnet. This construction allows the necessary visual access into the centre of the trap for electromagnetic radiation detectors. A positive aspect of this design is that several detectors can be mounted at once, therefore allowing for simultaneous scans of several different wavelength domains. Some further electrodes between the collector and the drift tubes assist in refocusing the electron beam or the ion coud when needed.
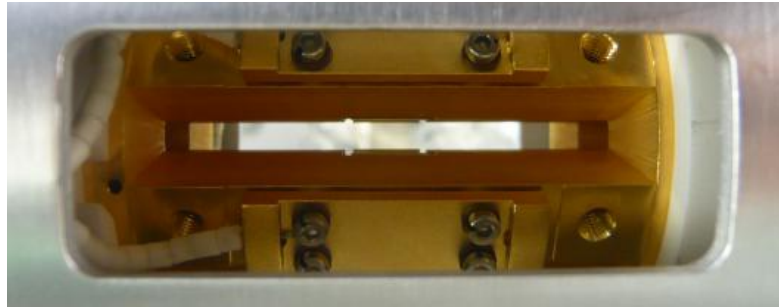

Figure 10: Image of the central trap electrode. The picture was taken through one of the slits drilled into the magnetic chamber [24].

3.1.3   Collector

The task of the collector is to capture the electron beam after traversing the trap. It comprises the following components: a magnetic coil; several electrodes; front and back shields; a supressor and an extractor (see Fig.11). The collector is insulated and grounded through a $10\,\Omega$ resistance. The magnetic coil serves to compensate the magnetic field from the trap region, effectively making it weaker. This entails a widening of the beam, assisted by the mutual repulsion of the electrons comprising it. The electrons finally reach the interior of the collector. All throughout this process heat builds up in these components; to counteract this, both the collector interior and the coil are cooled by water.
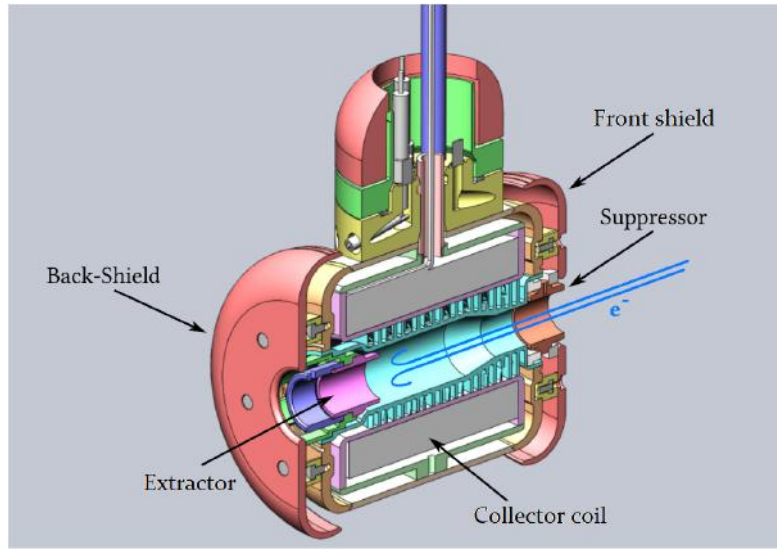

Figure 11: Axial sectional representation of the collector. Its different electrodes and coils are shown [22].

The extractor is set to a potential more negative than that of the cathode. This means electrons will be slowed down when approaching the extractor, thus stopping them from passing the collector and allowing them to be directed towards its interior. Furthermore, the escape towards the trap of any secondary electrons emitted by the collector during the dumping process is prevented by setting a supressor potential even more negative than the collector potential. A measurand of interest is the electron beam current I_{beam}, which can be obtained by measuring the voltage of the collector.

3.1.4 Injection system

To inject the gaseous compounds containing the ions to be studied a needle valve is used. It is mounted onto the FLASH-EBIT perpendicularly to the electron beam and it is employed to regulate the injection pressure. In order to avoid drastic variations in the magnet chamber pressure during the injection process, a two-step differential pumping system was implemented. This results in a pressure of up to 10^{-7} mbar in the primary stage, 10^{-9} mbar in the secondary stage, dropping to an overall cryogenic pressure of 10^{-12} mbar at the centre of the trap in the EBIT [21]. A representation of the injection system can be seen in Fig.12.
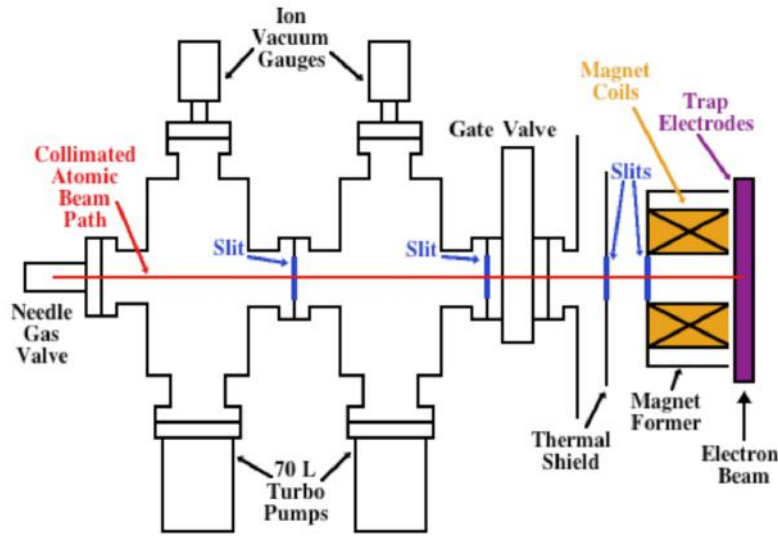

Figure 12: Sketch of the gas injection system. Two-stage differential pumping allows to introduce a collimated beam of gas molecules into the trap. There, the atoms in the compound are ionised by the electron beam. [22]

3.2 Electron beam properties

3.2.1 Electron beam radius

An approximate calculation for the electron beam radius was provided by L. Brillouin in 1945 [25]:

$$r_{\mathrm{B}} = \sqrt{\frac{2m_{\mathrm{e}}I_{\mathrm{beam}}}{\pi\epsilon_0 v_{\mathrm{el}}B^2}},\tag{25}$$

with the electron mass m_{e}, the amperage I_{beam} of the beam, the electric permeability ϵ_0, the electron velocity v_{el} and the magnetic field strength B. While providing a starting point for theoretical calculations of the beam radii, this formula fails to take into account the finite temperature - and thus the thermal energy - of the beam at the cathode. The assumption of a laminar flow used to derive this expression, i.e. the assumption of non-intersecting electron trajectories emitted from a region of zero magnetic field, does not hold when examined in detail.
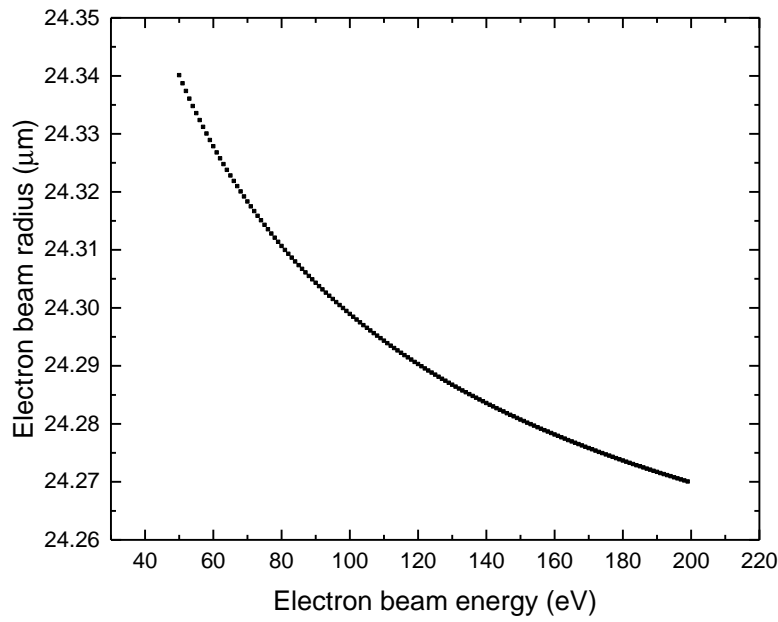

Figure 13: Exemplary evolution of the beam radius r_{H} depending on the electron beam energy with a constant beam current of $5\,\mathrm{mA}$.

G. Herrmann presented a more realistic theory which takes into account both the magnetic field B_c and the thermal energy through the cathode temperature T_c [26]:

$$r_{\mathrm{H}} = r_{\mathrm{B}} \sqrt{\frac{1}{2} + \frac{1}{2}\sqrt{1 + 4(\frac{8 m_{\mathrm{e}} k_{\mathrm{B}} T_{\mathrm{c}} r_{\mathrm{c}}^2}{e^2 B^2 r_B^4} + \frac{B_{\mathrm{c}}^2 r_{\mathrm{c}}^4}{B^2 r_{\mathrm{B}}^4})}}, \tag{26}$$

(see Fig.13). The importance of the beam radius resides in the relationship it bears to the processes taking place in the EBIT: the smaller the beam radius, the higher the current density

$$j = \frac{I_{\mathrm{e}}}{\pi r_{\mathrm{H}}^2} \tag{27}$$

at a given current I_{e}, thus higher the ionization rates, i.e., increasing the interaction rate between the electron beam and the injected compound.

3.2.2 Electron beam energy

The electron beam possesses an energy dictated by the potential difference

$$E_{\mathrm{beam}} \approx |V_{\mathrm{cathode}}| + |V_{\mathrm{platform}}| + |V_{\mathrm{trap}}| - |V_{\mathrm{sp,electrons}}| + |V_{\mathrm{sp,ions}}|, \tag{28}$$

where V_{cathode} is the cathode voltage, V_{platform} describes the voltage the drift tubes are set to and V_{trap} represents the voltage of the central drift tube. $V_{\mathrm{sp,electrons}}$ is the space charge potential of the electron beam, i.e. the potential arising from the repelling interactions of the electrons among themselves (see Fig.25). It is, of course, repulsive, which explains the negative sign preceding it. This potential can be estimated using

$$V_{\mathrm{sp,electrons}}[V] \approx \frac{30 I_{\mathrm{beam}}[\mathrm{A}]}{\sqrt{1 - (\frac{E_{\mathrm{e}}[\mathrm{keV}]}{511} + 1)^{-2}}} (\ln(\frac{r_{\mathrm{H}}}{r_{\mathrm{dt}}})^2 - 1), \tag{29}$$

where I_{beam} is the beam current, r_{H} the beam radius and r_{dt} the radius of the drift tubes [27]. This contribution is counteracted by the space charge potential of the trapped ions. Depending on the trap depth, the latter can go from being negligible to almost fully compensating the electron beam space charge potential.
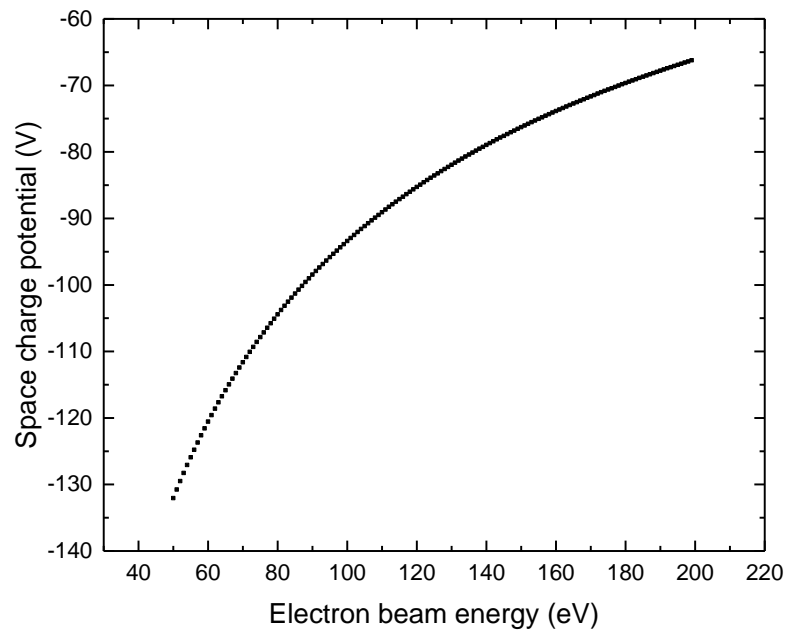
Figure 14: Exemplary evolution of the space charge of the electron beam depending on the beam energy.
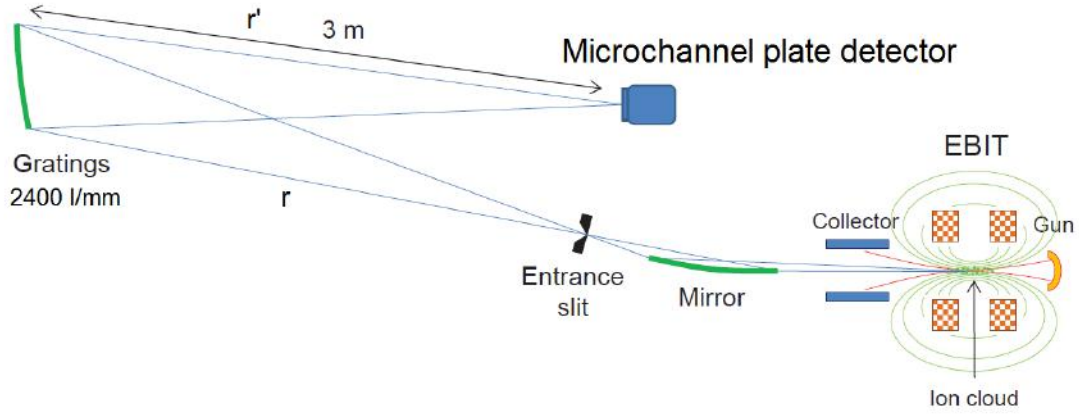
3.3 VUV spectrometer

Figure 15: Labeled sketch displaying the layout of the different setup components. It should be noted that the current setup does not include the grazing incidence mirror entrance slit. Hence, the ion cloud in the trap acts as the point source of the radiation.

The measurements in this thesis were performed with the newly installed 3 m normal incidence monochromator in the vacuum ultraviolet (VUV) range. The basic principle of the setup can be seen in Fig.15: radiation exiting the EBIT enters the first spectrometer arm, is then dispersed by a concave grating into the second spectrometer arm and focused onto a microchannel plate detector. This chapter provides detailed descriptions of the concave blazed grating and its properties, the principle of the Rowland circle underlying the measurements described in this thesis and the microchannel plate detector.

3.3.1 Blazed grating

The grating equation of a concave blazed grating is given by [28]

$$n\lambda = d(\sin\alpha + \sin\beta), \qquad (30)$$

where n is the diffraction order, d is the width of a groove, α and β are the angles of incidence and reflection, respectively (see Fig.16 and 17).

Blazed diffraction gratings are optimized for a particular wavelength. Optimally efficient reflection happens when the angle of incidence ϕ_i with respect to the blaze normal equals the angle of reflection ϕ_r. With respect to the grating normal, using $\phi_i = \alpha - \theta_b$ and $\phi_r = \beta + \theta_b$, the condition is

$$\alpha - \theta_b = \beta + \theta_b. \qquad (31)$$

Optimal reflection requires simultaneous fulfillment of this condition and the grating equation, which is only possible for one unique, so-called blaze wavelength. This is showcased in Fig.16.
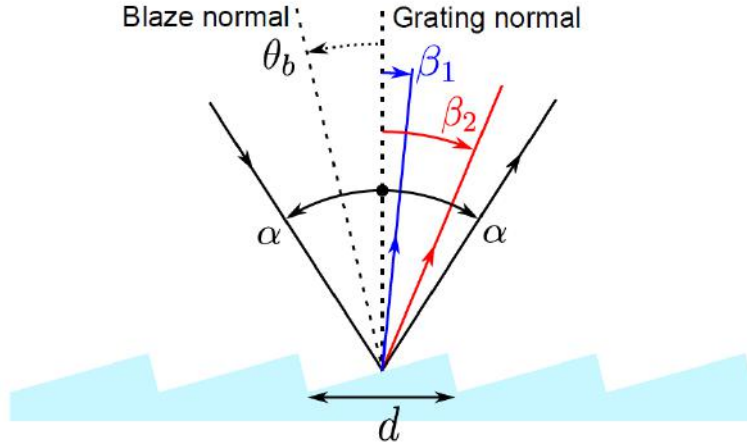
Figure 16: Sketch of a plane blazed grating with blaze angle θ_b showcasing the diffraction of an incoming beam (from [29]). The outgoing blue ray goes though specular reflection at the facet surface, its diffraction is therefore much more efficient than that of the red ray.

Another important quantity is the angular dispersion. It describes how well different diffraction lines can be resolved for a fixed incident angle: the greater the angular separation of two lines corresponding to different wavelengths, the better the resolution. Angular dispersion can

Table 2: Specifications of the grating (from [30]).

Parameter	Value/Specification
Grating length	150 mm
Radius of curvature R	3000 mm
Groove density $g = 1/d$	2400 lines/mm
Blaze wavelength λ_{b}	80 nm
Blaze angle θ_{b}	5.5°
Coating	Pt-coated

be expressed as [28]

$$\frac{\partial \beta}{\partial \lambda} = \frac{n}{d \cos \beta}. \tag{32}$$

The reciprocal angular dispersion,

$$D(\lambda) = \frac{\partial \lambda}{\partial \beta} = \frac{d \cos \beta}{n}, \tag{33}$$

is also known as the dispersion function and describes the change in wavelength with the reflection angle along the dispersive axis. Intgration with respect to β yields

$$\lambda(\beta) = \lambda_0 + \int_{\beta_0}^{\beta} D(\lambda) d\beta' = \lambda_0 + D(\beta - \beta_0), \tag{34}$$

where the second equality only holds if D is independent of λ [31]. The dispersion can then be approximated by a polynomial of the form

$$\lambda(\beta) = \mathrm{A} + \mathrm{B} * \beta + \mathrm{C} * \beta^2 + O(\beta^3). \tag{35}$$

In order to characterize a grating, calibration measurements are usually performed in order to obtain the values of the free parameters A, B and C. Their knowledge allows to predict at what angle a wavelength is detectable.

Finally, it should be noted that the spectrometer at the FLASH-EBIT uses a concave blazed grating. This means it inherits an optical aberration, astigmatism, already present in concave mirrors [28]. For this reason, the light stemming from a point source, e.g. the ion cloud in our setup, appears as a vertical line with respect to the dispersive axis on the focus plane. Therefore, the raw spectra taken in are in fact two-dimensional. This will be of importance in chapter 4.

The specifications for the grating currently in use, with which the measurements discussed in this thesis were carried out with, are detailed in Tab.2.

3.3.2 Rowland circle

Since the inception of spectroscopy, various techniques devoted to improving measurements were developed. A fundamental advance to the science, relevant to the presently discussed experiment, consists in the theoretical notion of the Rowland circle (see Fig.17).
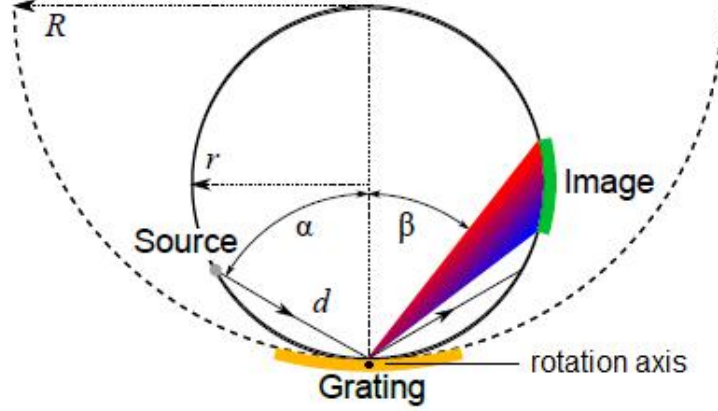

Figure 17: Sketch of the Rowland circle (from [29]).

Let an illuminated point source placed on a circle of the diameter R shine on a concave grating with curvature radius R that lies tangentially to the circle. The spectrum of this point source will thus be focused along this so-called Rowland circle. From the theory developed by Rowland himself and making use of Fermat's principle of least time, a condition for the focus distance is attained [28]. This condition can be recast into an expression for the focus distance r' (see Fig.15):

$$\frac{\cos^2\alpha}{r} - \frac{\cos\alpha}{R} + \frac{\cos^2\beta}{r'} - \frac{\cos\beta}{R} = 0$$

$$\Longleftrightarrow \; Rr'\cos^2\alpha - rr'\cos\alpha + Rr\cos^\beta - rR\cos^2\beta = 0$$

$$\Longleftrightarrow \qquad r'(R\cos^2\alpha - r(\cos\alpha + \cos\beta) = -rR\cos^\beta$$

$$\Longleftrightarrow \qquad r' = \frac{rR\cos^2(\beta)}{r(\cos(\alpha) + \cos(\beta)) - R\cos^2(\alpha)}$$

where r is the distance between the light source and the grating; R is the radius of the Rowland circle; α (alternatively β) corresponds to the angle between the incident (reflected) light beam and the grating normal. For a constant incidence angle α, the expression may be approximated

by a polynomial of the form

$$r' = \text{A} - \text{B} * \beta^2(\lambda) + O(\beta^3), \tag{36}$$

with the free parameters A and B and the angle β. This rough approximation for the focus distance as a function of the reflection angle will bear importance in chapter 4.

In practice, only three specific 'points' of this abstract construction are accomplished at a time: the ion cloud acting as point source, the grating and the detector (as displayed in Fig.15). Due to the chosen experimental setup, the angle between the two spectrometer arms remains fixed at a value of 15° by construction. Thus, at any given moment, only the part of the diffraction spectrum focused onto the detector is visible.

For spectral lines in different wavelength regimes to be detectable, they have to be specifically focused onto the detector. This is achieved by undertaking changes in the only degree of freedom left: the relative position along the Rowland circle of the grating with respect to the entrance slit and the detector. Rotating the grating around a central axis has exactly this effect. By rotating this grating, the incidence angle α with respect to the grating normal is changed. The reflection angle β needs to vary such that the sum of angles remains 15°; thus, different wavelengths are redirected onto the detector. In order to focus these wavelengths well, relation (36) is used.

3.3.3   Microchannel plate detector

The radiation reflected by the grating is registered by a microchannel plate detector (MCP). The photons are directed towards one of many microscopically small electron multiplier channels that go from one side of the plate to the other. The sides are taken by a pair of electrodes set at a certain voltage difference, thus creating an electric field.

In the interior of the channels, the photons can prompt the emission of electrons from the semiconducting material. These electrons eventually collide with the channel walls again but with increased energy due to the electric fields between the electrodes and also in the channels, thus secondary electrons will be emitted (see Fig.18). This process is iterated several times such that an electron cloud of typically 10^4 electrons exits one channel alone [32].

 The electron cloud reaches two superimposed delay line anodes (Fig.19). Both of them are set at a positive potential with respect to the MCP back end electrode such that the electron cloud travels as straight as possible to them. When the electron cloud hits an anode, an electrical signal is released towards both ends of the wire. By comparing the arrival times of the signal, it is possible to identify the position of the electron cloud along the wire, and thus to assign it
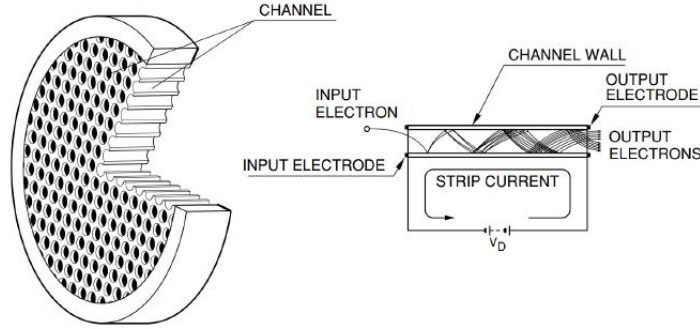
Figure 18: Sketch of an exemplary MCP detector and its channels. Notice the electrical field inside the channels creating an electron cascade (from [33]).

a physical coordinate. Two delay line anodes are used to capture the two coordinates on the anode plane. In this way the position of incoming particles can be registered.
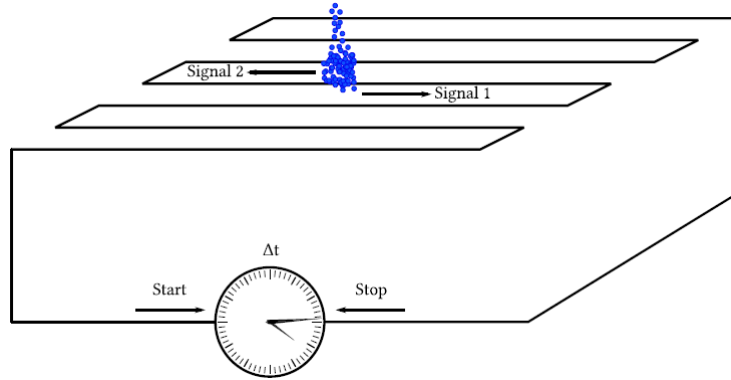
Figure 19: Sketch of a delay lines anode. In blue, the electron cloud prompting the emission of two electric signals travelling along the wire at nearly the velocity of light. From the time difference between the arrival of the two signals, the position along the wire can be calculated (modified from [22]).

3.3.4 Data acquisition system

The data of the MCP are acquired by the software MPA3 (Multiparameter Data Acquisition System) by FAST ComTec [22]. This system possesses eight channels with a digital resolution of up to thirteen bits, which corresponds to 8192 channels. In order to allow for different measure-

ments, each of these channels can be operated using up to three distinct modes. For this thesis, only the TDC (Time-to-Digital Converter) mode was used. TDC mode allows time differences to be encoded (this can be done with time differences between $50\,\text{ns}$ to $20\,\mu\text{s}$ with a resolution of up to $0.025\,\text{ns}$).

In order to visualize the spectrum, the MPANT software is used. With it, measured spectra can be viewed in one and two dimensions. Furthermore, it creates the listfile with all the spectral information necessary for further processing.

The two signals from the MCP indicating the hit position are not directly fed into MPA3 system. At first, they run through the module DLA-TR6 for discrimination and amplification, and afterwards through the GG8020 gate and a delay generator by Ortec. The latter ensures that the start and stop signals from the delay anodes arrive in the correct order such as to obtain a correct hit position from a precise runtime measurement. After the signals are processed by two TDCs they enter the MPA3 system. The intensities associated to the coordinates result from the number of hits, i.e. the number of detected photons, at a certain position on the MCP plane.

4 Data analysis technique

In essence, the core measurements performed for this thesis consist oxygen spectra taken with the FLASH-EBIT at diverse electron beam energies between $50\,\text{eV}$ and $200\,\text{eV}$. This entails the creation of different charged states of oxygen, ranging from O up to O^{4+}, which appear in different relative amounts as the electron beam energy is altered. This is expected to be traceable in the spectra as the relative abundances of transitions from different charge states and hence the intensity of spectral lines change. The ultimate aim was to provide a useful calibration of the spectrometer for future measurements using a well-studied element like oxygen. Lines in the spectra were compared with literature values, and eventual impurities were studied with the help of background measurements.

However, before proceeding to carry out the core measurements of this thesis, the FLASH-EBIT and the data analysis software had to be set up. For this, a series of preparatory measurements were carried out. Their aim was to help establish the values of two parameters of decisive importance for the quality of the data intake and analysis. This chapter will deal first with the measurements performed in order to correct the tilt of the spectral lines with respect to the axes of the MCP. Furthermore, it will delve into the process by which the one-dimensional spectra to be analyzed were created. This chapter will also be devoted to the measurements that helped establish a relation between the wavelength and the optimal focus distance between the grating and the MCP.

Before proceeding with the chapter it should be noted that the preparatory measurements described in this chapter were performed on iridium, which was being injected at the time for the purposes of a different research not linked to this thesis.

4.1   Techniques of spectral recording

The spectrum reflected by the diffraction grating along the Rowland circle is detected by the MCP at the end of the second spectrometer arm. The raw, two-dimensional spectrum is ideally projected onto the dispersive axis, i.e. all the counts at a certain dispersive axis position are summed and plotted against the very same horizontal axis position. This yields the intensity of the radiation as a function of the position along the dispersive axis, which is dependent on the wavelength.

The above procedure holds when measuring only the part of the spectrum covered by the grating at a fixed position, i.e. a static grating. In order to detect a spectrum over the span of several hundreds of nanometers, the grating needs to rotate in order to redirect different wavelength windows onto the detector. For each time step, chosen small enough such that the part of the spectrum projected onto the MCP can be said not change, a two-dimensional image is recorded and projected onto the dispersive axis as described before. It is then possible to represent the evolution of the image projected onto the detector as a function of the grating rotation angle, which can be encoded either in so-called time bins or in a voltage between $0\,\mathrm{V}$ and $10\,\mathrm{V}$ that is fed to the analog-to-digital converter. As long as the rotation occurs at a perfectly constant rate, both representations are essentially equivalent. These procedures allow establishing the rotation angle of the grating at which spectral lines were projected onto the MCP and enable the measurement of a wider range of the spectrum than measurements with a static grating permit. A calibration assigning the time steps (henceforth time bins or time channels) or the voltage bins to wavelengths yields the desired wavelength-dependent intensity spectra.

4.2   Corrections of line tilts

However, two fundamental problems arise when applying the measurement technique described in 4.1. Firstly, it is not possible to set up the delay line of the MCP in a parallel fashion with respect to the dispersive axis. This results in a first tilt of the detected spectral lines that is present already in measurements with a static grating, but affects those with a rotating grating equally (see Fig.20). The software used in order to project the spectral lines performs the projection onto the vertical axis of the MCP image. If the vertical axis and the dispersive axis are not well aligned, the resulting projection does not correctly represent the intensity distribution along the dispersive axis. Therefore, the tilt of the lines needs to be corrected. This is implemented

36

by a Python program. With the help of this program, the two-dimensional spectra - fed in as binary listfiles - are rotated by a certain angle Φ with respect to the horizontal MCP axis such that the lines in output spectra stand parallel to the latter. After this rotation, the spectrum may be projected onto the dispersive axis (which now coincides with the vertical MCP axis) and its the time-/angle-dependent evolution may be plotted.
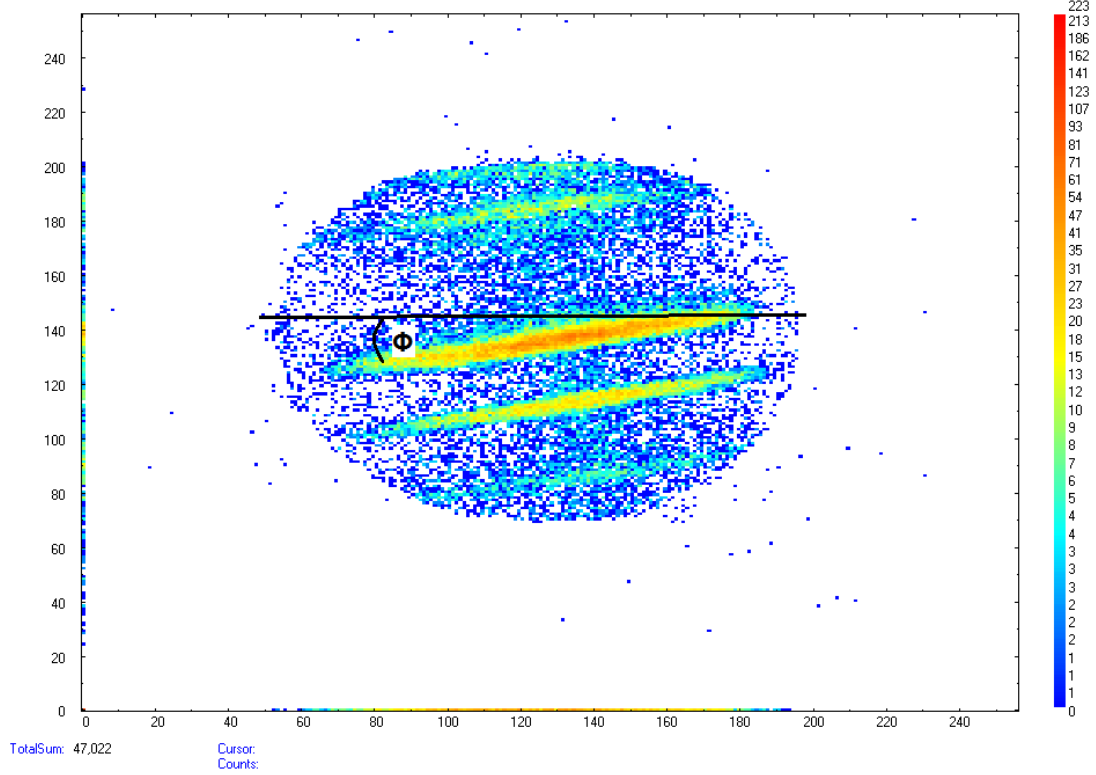

Figure 20: Image of the spectrum detected around a clear iridium line at $570\,\text{eV}$ with a static grating as displayed by the MPANT software. The colour scale on the image goes from blue (low counts) to red (high counts). The line of interest is placed in the optimal region of the MCP, its centre. The black line is perpendicular to the vertical MCP axis.

As outlined in detail in [22], the angle Φ can be obtained using an autocorrelation process. However, it was suggested that the angle obtained prior to the start of the thesis could still be improved. Incidentally, when the vertical MCP axis and the dispersive axis stand parallel to each other, the projected spectral lines attain minimal width. Hence, the idea was to measure a

37

single spectral line, process it with the Python program using different values for Φ and obtain a plot of the peak width as a function of the angle employed.

An attempt at obtaining Φ was made by measuring a random peak in a yet uncalibrated iridium spectrum at 570 eV. The grating was kept at a fixed angle such as to focus the peak onto the center of the MCP (see Fig.20). The two-dimensional spectrum was saved as a listfile and fed into the Python program 25 times with 25 different angles for Φ. The resulting one-dimensional spectra were plotted in Origin. With the help of the fitting tool, Gaussian curves with the centroid, amplitude and width as free parameters were fitted onto the same peak in the different plots. The widths obtained were plotted against the angle Φ employed in the Python program.
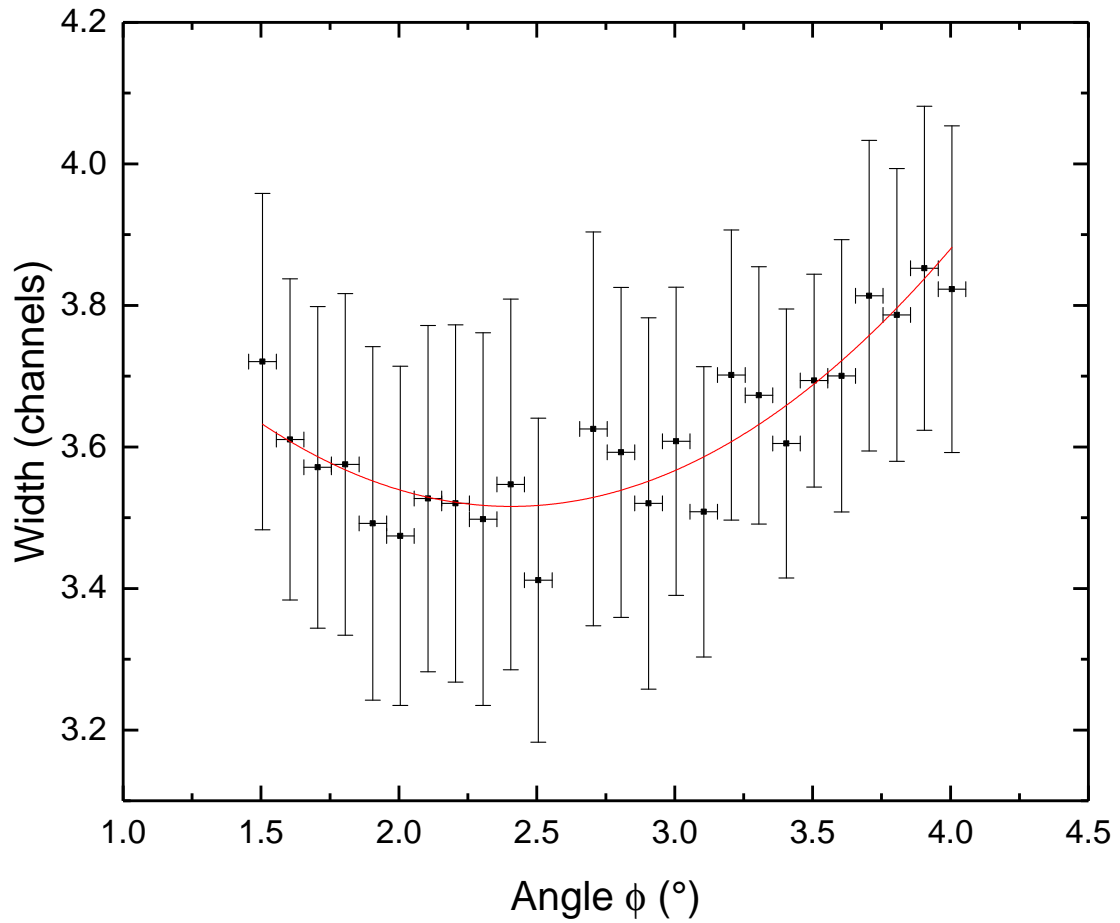

Figure 21: Plot of the widths of the peak depending on the angle Φ employed in the Python script to correct the slant. The horizontal error bar corresponds to an estimate of 0.05°, the vertical error bar stems from the width uncertainty of the Gaussian fit.

A quadratic fit was applied onto the resulting data set, and from the parameters obtained, the angle yielding the minimal peak width was calculated (Fig.21). This yielded a value of

$$\Phi = 2.41(5)\,^\circ, \tag{37}$$

where the uncertainty was calculated using Gaussian error propagation. It would henceforth be the value employed in the Python script for the rest of the measurements performed in the context of this thesis.

A second issue arises from the rotation of the grating alone. After each time step, the positions of the peaks along the vertical MCP axis change as the grating rotates: the spectral peaks are shifted upward (or downward, depending on the rotation of the grating). When plotting the one-dimensional projections onto the dispersive axis as a function of the rotation angle, the shift in the position of a peak along the MCP axis results in a further tilt.

This tilt, the slope of which depends on the rotation velocity of the grating, can again be corrected through the use of autocorrelation methods. For this, the lowest dispersive axis bin (parallel to the time axis) is fixed. With the help of Gaussians, the positions of the peaks in this horizontal bin are obtained. The positions of the peaks in the rest of the bins are obtained in the same manner. Then, the horizontal bins are all shifted such that the peak positions coincide with the positions fixed by the lowest bin. This correction provides a plot with lines perpendicular to the time axis, onto which they are then projected in the last step of the Python program. This results in a one-dimensional spectrum where the position along the dispersive axis is encoded in the time bins. It is the step from time bins to wavelengths which will require a calibration for future line identification.

It should be noted that the correction procedure in case of plotting the dispersive axis against the grating angle is the same, with one clear advantage: the tilt will always be the same, since the slope does not depend on the rotation velocity of the angle anymore.
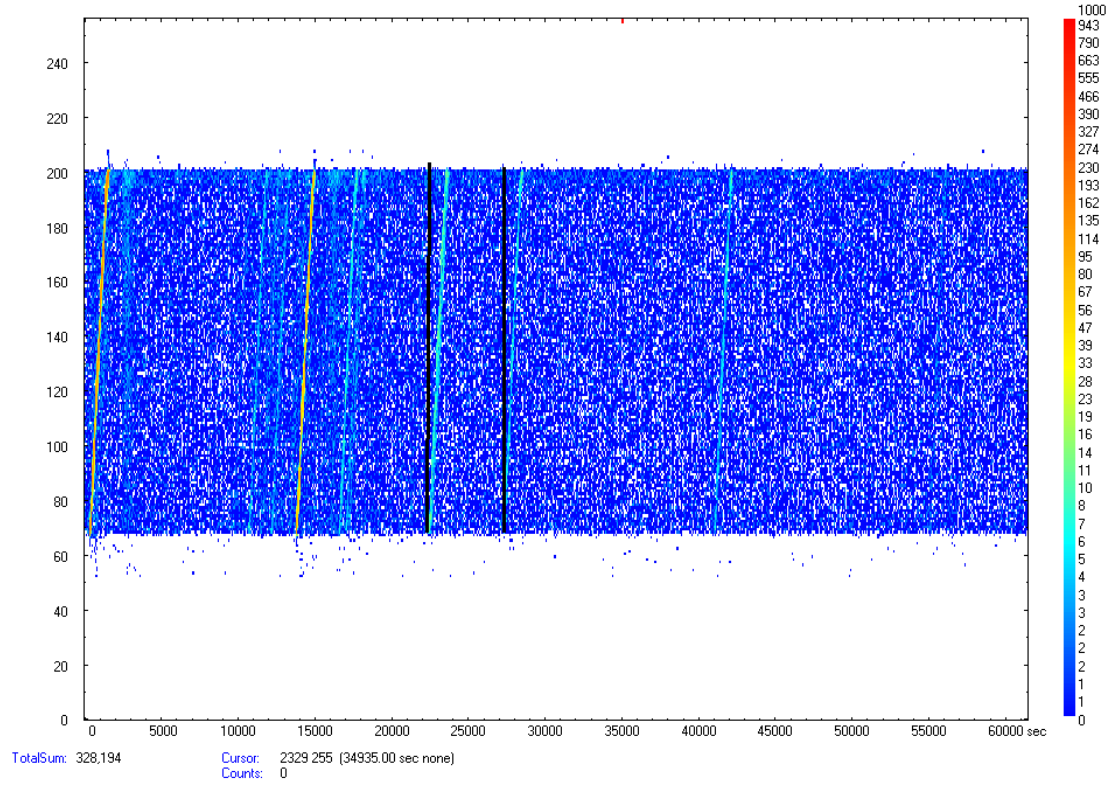
Figure 22: Two-dimensional, tilted plot of the dispersive axis as a function of the rotation angle of the grating. The x-axis displays the angle in terms of time bins, the y-axis indicates positions along the dispersive axis. The black lines showcase the ideal disposition of the lines before the vertical projection. In later measurements (chapters 5 and 7), the settings allowed to take in data from $0\,\mathrm{nm}$ up to $280\,\mathrm{nm}$.

4.3 Repositioning of the MCP with respect to the grating

The position of the MCP is an important parameter for the resolving power of the setup. As discussed previously, its distance to the grating surface has to change in order to observe a well-focused image at different wavelengths. This section deals with the experimental finding of the relation between wavelength and optimal MCP position.

The core idea behind the measurements carried out in this part is that, at the optimal focus distance between the grating and the detector plane, the width of a spectral line should be minimal. Therefore, the measurements consisted in recording single lines of the spectrum up to ten times each under nearly identical conditions. The only variation would be the distance of the detector with respect to the grating. The distance was measured with respect to two selected reference points: the frontal plate of the MCP, and the frontal plate of the casing into which the second spectrometer arm falls. The distance between the MCP itself and its frontal plate is 16.9 ± 0.1 cm. By this time, changes in the MCP position were still performed manually, since the MCP motor was yet to be mounted. The reference distance was, in any case, measured with a vernier caliper.
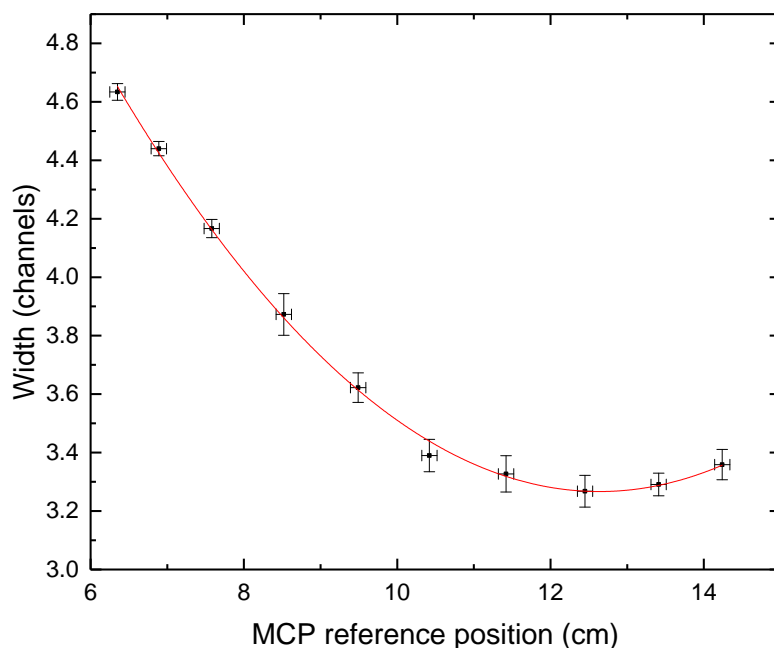

Figure 23: Exemplary plot of the zeroth-order line width depending on the MCP reference position.

In order to obtain the spectra for each of the ten measurements performed for the different lines, we chose to encode the grating rotation angle into voltages. Furthermore, the data analysis procedure of the spectra was similar to the procedure described and used in the previous subsection.

For each of the recorded lines, the ten peak widths obtained from the Gaussian fits were plotted against the respective reference distances of the MCP. The data points on these plots would outline parabolic shapes for all the lines analyzed (an example of this can be seen in Fig.23). Therefore, quadratic fits of the form

$$\text{width} = \text{a} * (\text{MCP position})^2 + \text{b} * \text{MCP position} + \text{c} \tag{38}$$

with three free fitting parameters a, b and c were applied onto these data sets. The outcome values of the parameters were used to obtain the position of the parabola minima on the plots, i.e. the reference distance of the MCP allowing a line to be detected at its narrowest width. These quadratic minima mark indeed the optimal distance of the MCP with respect to the grating for a given wavelength, since at perfect focus the width of the line is expected to be minimal. The uncertainties in the minima positions were estimated using Gaussian error propagation.

In the final step, the positions of the minima that were obtained from the analysis were plotted against the wavelengths of the respective peaks. At this point, the wavelengths could only be roughly estimated by using a preliminary calibration of the spectrometer. This calibration stemmed from previous measurements on highly charged helium and oxygen ions. It first allows converting the grating angle into a time bin value through a linear polynomial of the form

$$\text{time bin} = \text{offset} + \text{r} * \text{angle}, \tag{39}$$

with an offset of -2600 time bins and a constant r of -200 time bins/degrees. This time bin value (# time bin) is then transformed into a wavelength through a second-order polynomial,

$$\text{wavelength} = \text{wavelength offset} + \text{s} * (\text{\# time bin}) + \text{t} * (\text{\# time bin})^2, \tag{40}$$

where

$$\text{wavelength offset} = -0.52020 \, \text{nm}, \;\; \text{s} = 0.07133 \frac{\text{nm}}{\text{time bin}}, \;\; \text{t} = -5.70048 * 10^{-8} \frac{\text{nm}}{(\text{time bin})^2}. \tag{41}$$

The lack of uncertainties provided with this rough calibration further consolidated the need for a proper calibration process. For the sake of these measurements however, the error bars

were estimated in the following way: fixing the grating at an angle which would yield a line at the centre of the MCP image, one would find out an upper threshold for the relative angle of the grating compatible with the line still being visually perceived in the centre. This was the only way of taking into account both the estimated width of the detected line as well as the error in the perception of the line position in the image. An overall change in the relative angle of approximately $0.05°$ - around $0.7\,\text{nm}$ in the range of our data, according to the rough calibration - was deemed a sensible overall uncertainty value given the preliminary nature of this measurement. Nonetheless, from the size of the error bars it is clear that the uncertainty stemming from the MCP position prevails.
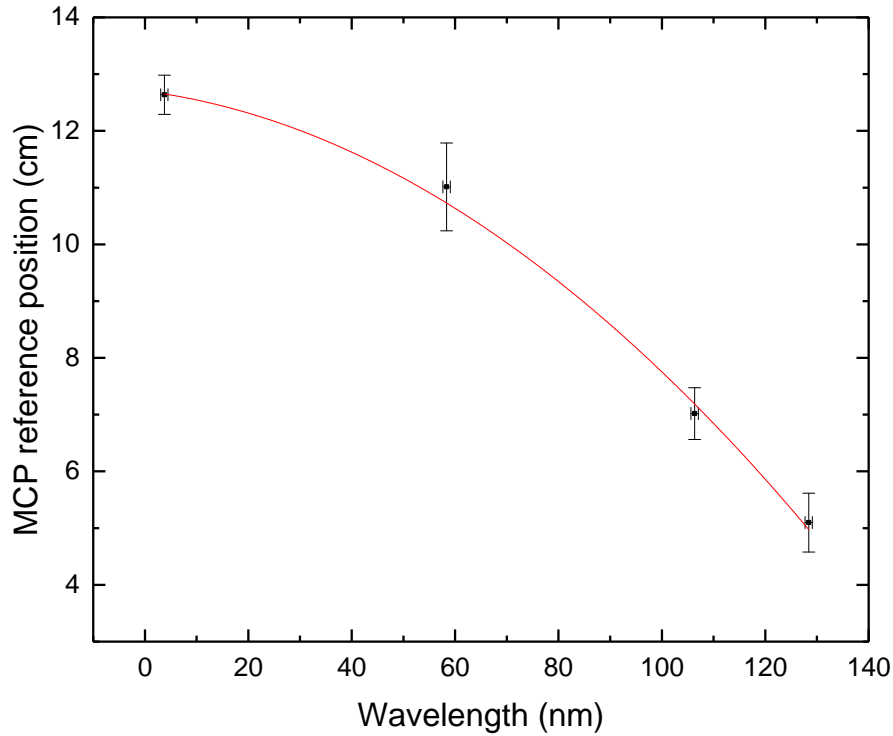

Figure 24: Plot of the MCP reference positions yielding minimal wavelengths against a rough estimate of the wavelength of the analysed peaks. The quadratic fit results in an inverse parabola. As discussed, the horizontal error bars originate both from a rough estimate of how good a line was positioned at the centre of the MCP as well as from the rough line width. Although the adjusted R-square value of approximately 0.993 seems to indicate a good fit, one should take into account the comparatively large uncertainties for the coefficients a and b. The analysis of more lines would have helped to improve the values and suppress the errors.

The final outcome of this procedure was a set of data points outlining an inverse parabola (see Fig.24), which was in turn fitted by yet another quadratic function of the form

$$\text{MCP referece position} = \text{MCP position offset} + a * \text{wavelength} + b * \text{wavelength}^2. \qquad (42)$$

The values of the coefficients were

$$\text{MCP position offset} = 12.7(2), \;\; a = -0.01(1), \;\; b = -4(1) * 10^{-4}. \qquad (43)$$

Using these parameters it was possible to fix the MCP position at the optimal distance in subsequent measurements. More importantly, in the future, these parameters can be used in the program that is to regulate the MCP position automatically as a function of the grating rotation angle.

5 Recording of oxygen spectra

5.1 Measurement conditions

The core measurements of this thesis consisted of the spectroscopy of oxygen ions up to O^{5+} in the FLASH-EBIT. The conditions of injection include a constant injection pressure of $2.2*10^{-6}$ mbar at room temperature. The shape of the trapping potential formed by the drift tubes was kept constant throughout all the measurements (see Fig.25). However, changes in the electron beam energy took place: it was varied from $50\,\mathrm{eV}$ to $110\,\mathrm{eV}$ in steps of $20\,\mathrm{eV}$, then in steps of $10\,\mathrm{eV}$ until $200\,\mathrm{eV}$. This entailed changes in the electron beam current and radius. Moreover, two background measurements at $110\,\mathrm{eV}$ and $150\,\mathrm{eV}$ were performed in order to obtain some hints about possible impurities in the observed spectra. Further information on the measurement conditions and parameters can be retrieved from Tab.3 and Fig.25.
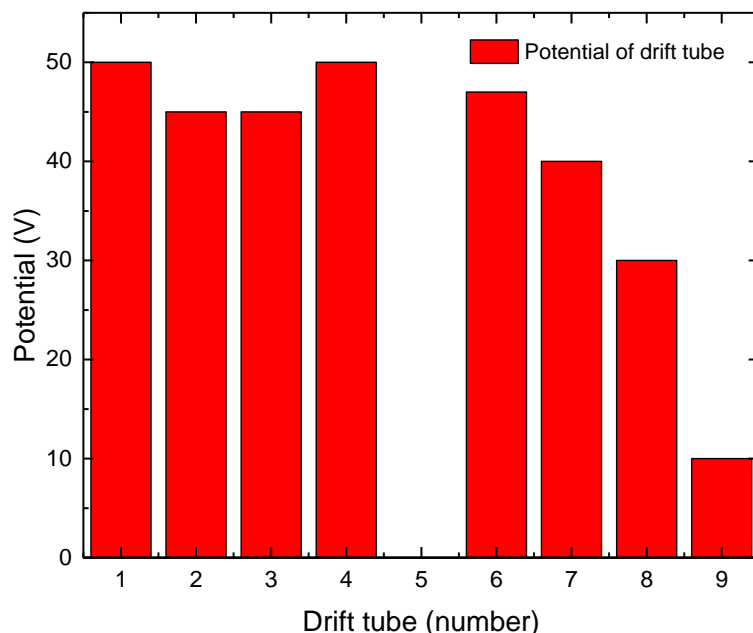

Figure 25: Shape of the potential for the oxygen measurements. The drift tubes are labeled in a numerically increasing order going from the cathode side to the collector side. The height of the bars indicates the potential at which each tube was set. The central drift tube (number 5) was set at $0\,\mathrm{V}$ for these measurements.

Table 3: Specifications of the measurements

Parameter	Value/Specification
Energy range	$50\,\text{eV}$ - $200\,\text{eV}$
Beam current	$3.0\,\text{mA}$ - $6.5\,\text{mA}$
Beam radius	$24.3\,\mu\text{m}$
Scanned angle interval	$[-13.0°\,;\,-33.0°]$
Grating rotation velocity	$3.25 * 10^{-4}\,°/\text{s}$
Injection pressure	$2.2 * 10^{-6}$
Magnetic field	$6\,\text{T}$

5.2   Spectral recording procedure

For the typical measurement, the grating was set to scan an angle interval at a constant velocity while the MCP was fixed at a reasonable distance to optimally detect lines in the densest part of the spectrum observed (at around $60\,\text{nm}$). The rotation of the grating for these measurements carried all the implications - necessary corrections of the spectra - described in the previous chapter. However, and as opposed to the measurements described in chapter 4, for the measurements performed on oxygen the grating angle would be encoded directly into time bins.

Another important remark is that, ideally, the MCP position would have been continuously adjusted to the optimal focus distance. This would allow for a much better resolution in a wide band of wavelengths. However, due to time constraints the implementation of a script allowing an automatic focus adjustment was not carried out.

5.3   Spectral calibration

After projecting a plot of the temporal evolution of the dispersive axis onto the time channels, the next step is to map the time channels onto wavelengths. The goal is to obtain a spectrum as a function of the wavelength. As discussed in 3.3.1, it turns out that the relation between reflection angle and wavelength can be approximated by a polynomial that, for our purposes, can be cut off at the second degree term. Since the reflection angle and the time channels encoding the rotation angle of the grating are related linearly, the wavelength focused onto the MCP as a

function of the latter is

$$\lambda(\text{time channel}) = x * (\text{time channel})^2 + y * (\text{time channel}) + z, \qquad (44)$$

with the constants x, y and z. To find out the value of the coefficients, the setup needs to be calibrated. A calibration can be performed by using elements whose ions have well-studied transitions. Oxygen is one of those elements. Using oxygen, the observed lines in a spectrum as a function of the time channels can be assigned to well-established wavelengths of e.g. the National Institute of Standards and Technology (NIST) database. A quadratic fit allows obtaining the values of the coefficients. For subsequent measurements, (44) is applied onto the measured peaks in the time channel spectra to obtain the wavelength values.
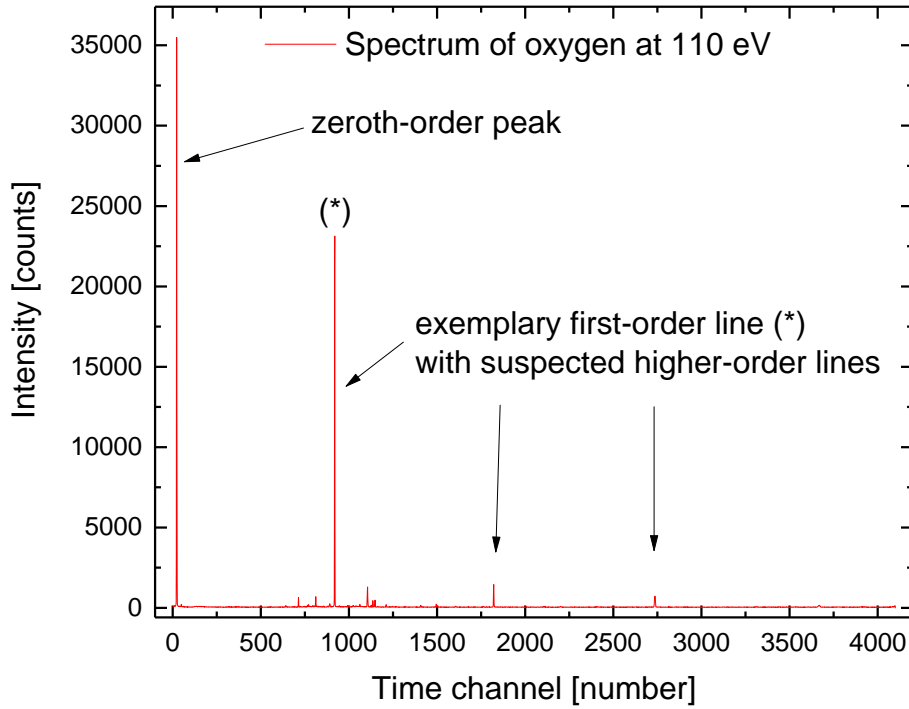

Figure 26: Example of a time channel-intensity spectrum as measured at 110 eV. Some notable features are the zeroth-order peak (image of the ion cloud) as well as a first-order line with some suspected higher-order lines.

In our case, the calibration procedure and subsequent analysis were carried out using the Origin software. Each spectrum was imported into an Origin file and a time channel-intensity spectrum was plotted. The goal was to find a solid calibration that would also ensure the possibility of a direct comparison between different spectra. A way of achieving this was by exploiting the fact that the image of the ion cloud, the zeroth-order peak, is to be found at exactly $0\,\text{nm}$. In the plotted time channel-intensity spectrum, this peak was found usually between channel numbers 20 and 40 (see Fig.27). The best estimate of its position would be obtained by fitting a Gaussian onto it. In a new column of the Origin worksheet, the value of the Gaussian centroid was subtracted from all the time channel numbers, thus resulting in what could be called *corrected* time channel numbers. Plotting the measured intensities against these yielded a shifted time channel-intensity spectrum with the zeroth-order peak at time channel number 0.
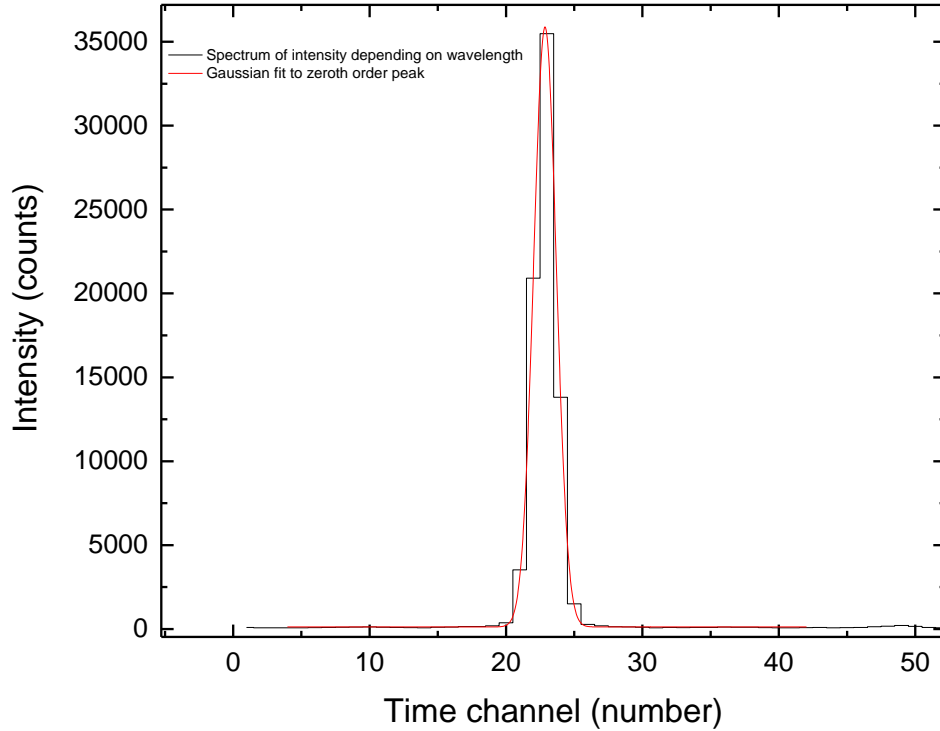

Figure 27: Position of the zeroth-order peak in the measurement at $110\,\text{eV}$ (uncorrected channel-intensity spectrum). For further analysis, the channel value of the Gaussian centroid is subtracted from all the channel values. When performed for all spectra, this allows applying one same calibration onto all the recorded data and thus direct comparison between the spectra.

In theory, this procedure should help overcome any minor variations affecting the reproducibility of the measurements, i.e. if the positions of the spectral peaks of two identical measurements vary globally by a certain number of time channels, this procedure corrects the difference, thus making both spectra comparable. Indirectly, this also gives further means to judge the goodness of a calibration: if as a result of applying the calibration onto these corrected channel numbers the zeroth-order peak is not nearly close to $0\,nm$ (in terms of centroid error), the calibration can be dismissed.

In order to determine the precise time channel value (i.e. position) of a spectral peak which is to be assigned to a wavelength in the calibration procedure, the centroid of a Gaussian fit to the peak in the time channel-intensity spectrum is needed. To carry out a good calibration it is necessary to perform as many - correct - assignments to the diverse Gaussian centroids as possible. This should help reduce the uncertainty of the fitting parameters of the quadratic polynomial. Ideally one tries to identify higher-order lines besides the main peaks (see Fig.26); this not only usually eases the identification of the transitions but also ensures a valid and trustworthy calibration over a wider range of the spectrum.

As long as it is performed correctly, a calibration procedure needs to be performed only once. In practice, however, several calibrations with varying degrees of success were performed until a definitive one was attained. The reason for the latter was that, for the most part, higher-order lines were hard to identify if existent at all. There are two reasons for this:

- the optimal wavelength regime of the grating lies at around $80\,nm$, the diffraction of wavelengths far beyond that value being inefficient in any case;

- it was not yet possible to continuously and automatically adjust the MCP position to achieve optimal focus at all wavelengths. The MCP position was therefore specifically fixed at a distance allowing optimally focused measurements at around $60 - 80\,nm$, since it is a region of high line density for the charged states of oxygen that were observed.

Due to this lack of higher-order lines, the high variability in the outcomes of the calibration procedure was a problem for some time. A particularly good example of this is found in two calibrations that were carried out following a measurement at $50\,eV$ of electron beam energy. The two calibrations were essentially identical in spite of minor differences regarding the choice of identified lines. While two spectra using each one of the calibrations would match considerably well in the region that provided most of the identified lines, they would differ in their larger

49

wavelength ranges significantly 28. What is more, none of the two calibrations was inherently and decisively *better* than the other one abiding by the usual standards for judging fits: size of fit parameter errors, sum of squares of residuals, adjusted R-squared, fit bias and the likes. Thus, none could be formally excluded - and none could be deemed a definitive calibration.
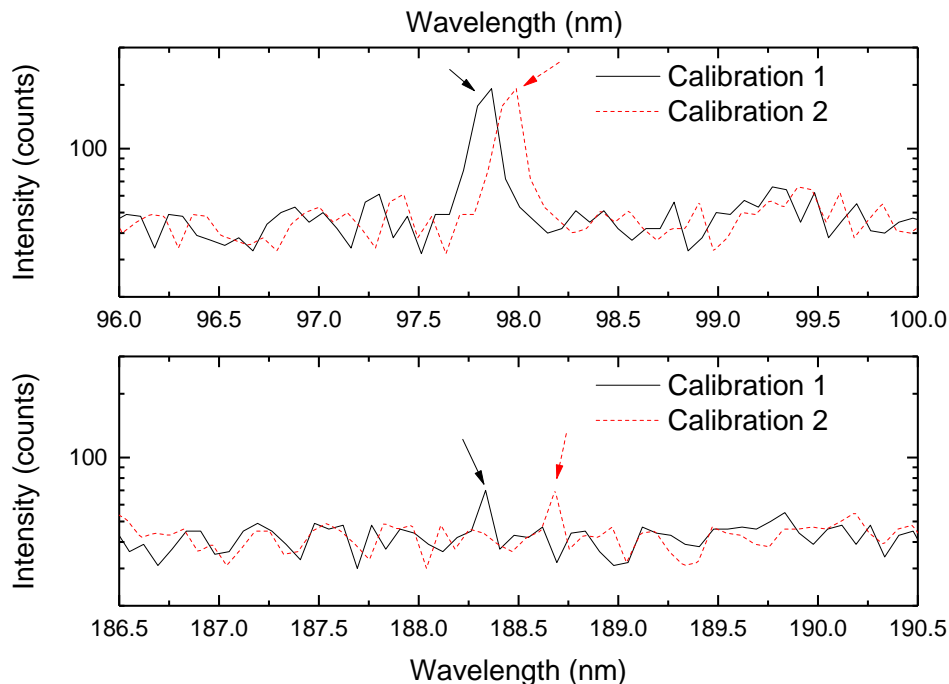

Figure 28: Visualization of the shift of one same spectrum onto which two different calibrations have been applied. The shift increases with the wavelengths as the quality of at least one of the calibrations decreases. The arrows mark two features which display this shift the best.

It was a measurement at an electron beam energy of $110\,\mathrm{eV}$ that yielded the sought-after higher-order reflections. Consisting of O^{3+} and O^{4+} transitions (see Tab.4), the spectrum showed up to three clear peaks in ranges that had appeared flat so far in lower-energy measurements. These peaks could not be assigned to any sensible first-order lines found in the *NIST* database. Furthermore, a mere visual analysis suggested similar intervals between the peaks - therefore the possibility of them being higher-order peaks was considered. The highest peak in the spectrum besides the zeroth-order was proposed as the corresponding first-order peak. In this spirit, it was assigned to the O^{4+} line at $62.973\,\mathrm{nm}$ of the NIST database [34]. The three next integer multiples of the given wavelength were then assigned to the suspected higher-order peaks. A simplified calibration using only these four assignments resulted in a sensible fit judged by the

standards mentioned previously. The successive calibration attempts using additional identified lines aimed at reducing the uncertainty of the fit parameters and thus improving the quality of the calibration. High variability in the outcome spectra was largely suppressed thanks to the higher-order peaks helping to anchor the calibration around sensible values (Fig.29).
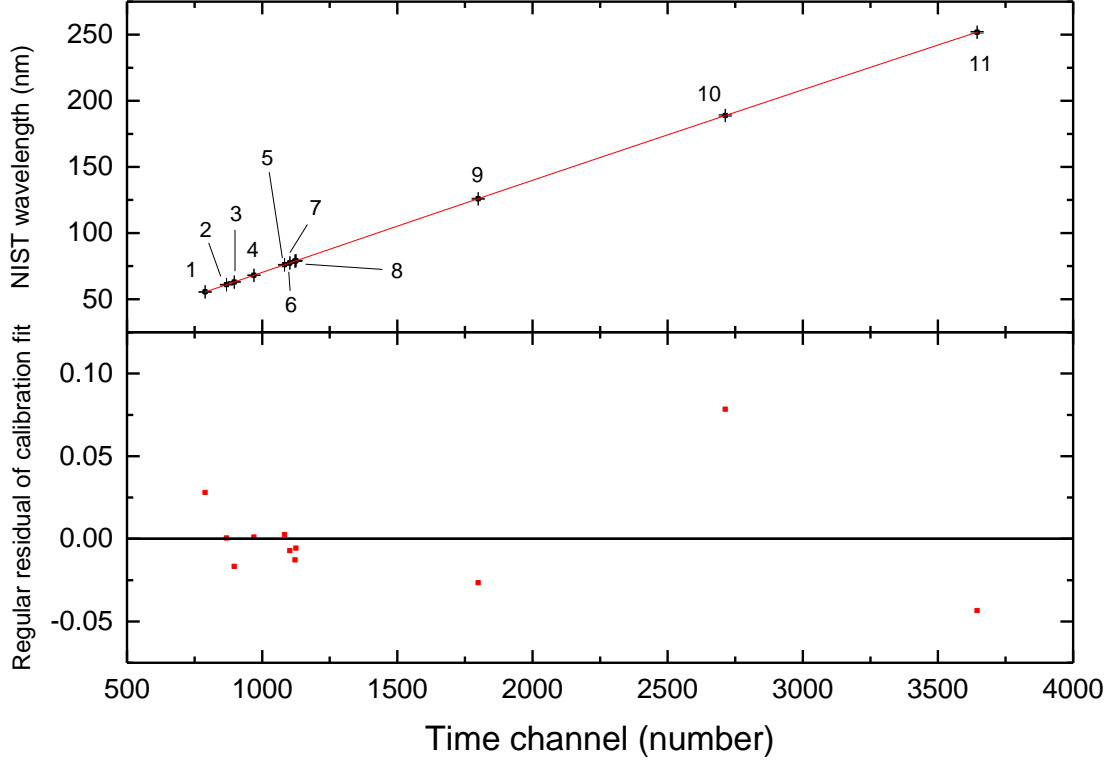

Figure 29: Definitive calibration of the spectrometer using a measurement at $110\,\text{eV}$ together with a plot of the regular residual of the calibration fit. The latter shows there was no particular bias in the calibration. For the fitted data points, see Tab.4.

The quadratic fit to the data set yielded the following values for the parameters of the new calibration:

$$x = -5.7(2) * 10^{-7}, \ \ y = 0.07136(7), \ \ z = -0.54(5), \tag{45}$$

The calibration seemed to be trustworthy, its quality being showcased in particular by the adjusted R-Squared [1] value of 1 according to Origin and the absence of a bias as shown by Fig.29.

_____
[1] The adjusted R-Squared is defined as [35]

$$R_{adj}^2 = 1 - \left[\frac{(1 - R^2)(n - 1)}{n - k - 1}\right], \tag{46}$$

Table 4: Peak positions at an electron beam energy of 110 eV used for calibration. Time channel and ΔTime channel represent the peak positions and their uncertainties in time channels. The columns λ (nm) and $\Delta\lambda$ (nm) indicate the wavelengths and errors of the peak positions (in nanometers). The wavelength uncertainties were obtained from Gaussian error propagation using the parameter uncertainties from previous calibration attempts with approximate parameter values.

Line	Time channel	ΔTime channel	NIST λ (nm)	$\Delta\lambda$ (nm)	Charged state
1	789.20322	0.03719	55.4514	0.24841	O^{3+}
2	868.15317	0.19388	60.9829	0.25991	O^{3+}
3	896.68562	0.00636	62.9730	0.26395	O^{4+}
4	969.75929	0.06163	68.1272	0.27405	O^{4+}
5	1082.54571	0.06124	76.0445	0.28900	O^{4+}
6	1102.75751	0.10714	77.4518	0.29161	O^{4+}
7	1121.66114	0.06888	78.7711	0.29403	O^{3+}
8	1125.10926	0.04928	79.0199	0.29447	O^{3+}
9	1798.82669	0.01531	125.9460	0.37243	O^{4+}
10	2712.98593	0.06949	188.9190	0.46721	O^{4+}
11	3644.81998	0.18064	251.8920	0.56709	O^{4+}

Likewise, a residual sum of squares (0.05882) which did not increase significantly with the addition of new lines after the original four further supported the claim of its trustworthiness, which is the reason this calibration forms the basis of all ensuing results obtained for this thesis. Wavelengths of detected peaks were obtained by applying Gaussian fits onto the time channel spectra. The data resulting from the fit - namely the peak position and width, together with their uncertainties - would be converted into wavelengths by applying the calibration as detailed in (44) with the values displayed in (45). The wavelength error was then calculated from the time channels i by applying the Gaussian error propagation:

$$\Delta\lambda(\text{i}) = \sqrt{(\Delta z)^2 + (\text{i} * \Delta y)^2 + (\text{i}^2 * \Delta x)^2 + ((y + 2x\text{i}) * \Delta \text{i}^2)} \qquad (47)$$

At first instance, this procedure eases the task of applying future calibrations onto peaks which have already been found, as opposed to fitting Gaussians on wavelength spectra which

where n is the number of data points in the sample and k the number of variables. It is usually employed as a goodness-of-fit parameter.

would have to be plotted anew. Furthermore: the use of the uncertainty calculation above allows to sensibly account for the overall uncertainty that is added to the procedure due to the calibration. This uncertainty, in fact, dominates over the uncertainty stemming from the choice of the fit interval and procedure. This explains the large uncertainties at larger wavelengths, since in that regime the quadratic approximation employed to describe the angular dispersion starts to veer off; the lack of calibration points in this regime only adds to this. Hence, the calibration becomes less precise, naturally yielding larger uncertainties.

6 Resolution analysis of the spectrometer

A useful concept in spectroscopy is that of the spectral resolution, which is a measure of how well two lines can be distinguished in a spectrum. The better the resolution, the smaller the spectral distance of two independent lines that may be resolved as such. Following Rayleigh's criterion, this is the case when the diffraction maximum of the second line falls onto the minimum of the first. This minimal distance at which spectral features can still be resolved independently is generally represented by $\delta\lambda$. In experimental physics, $\delta\lambda$ is usually approximated with the full width at half maximum (FWHM) of the lines. Closely related to the concept of spectral resolution is that of the resolving power, usually given as

$$R = \frac{\lambda}{\delta\lambda},$$
(48)

where λ is the wavelength of a spectral line and $\delta\lambda$ the aforementioned resolution [36].

In practical terms, an estimate of these quantities can be provided by obtaining the FWHM from Gaussian plots onto a significant number of peaks along the spectrum. Plotting the FWHM and R against the wavelength λ gives an indication as to how the goodness of measurements changes with the wavelength regime analyzed. A unique analysis should be enough to yield a meaningful statement as long as the setup does not undergo any significant changes.

It should be noted that the peak widths (w) displayed by the Origin software do not correspond to the FWHMs, which were obtained as follows:

$$\text{FWHM} = \text{w} * \sqrt{2\ln 2}, \ \Delta\text{FWHM} = \Delta\text{w} * \sqrt{2\ln 2},$$
(49)

with Δw and ΔFWHM being the width and FWHM uncertainties, respectively.

In order to perform an analysis of the resolution, ideally, the FWHM of all the spectral peaks are plotted against their respective wavelengths. At first instance, however, this procedure might not be appropriate, the reason being that many of the peaks have not yet been identified at this stage. A spectral peak composed of several lines, blended due to the resolution limit of the setup, may be interpreted as a single line with a large FWHM. Should there exist many of these blended lines, the results of the resolution analysis would suffer from severe distortion. Therefore, a first approximation to the analysis was carried out by taking into account only one very clearly identified peak with likewise clearly resolved higher order reflections. At 110 eV, the prominent line at 62.9730 nm fulfilled these conditions. This allowed for a very rough analysis of the resolution over a wide range of the spectrum. The four points outlined a parabola, hence a

quadratic fit function was used in order to obtain a mathematical expression for resolution along the spectrum (Fig.30). From the fit parameters it was possible to calculate the minimum of the parabola, corresponding to the resolution limit of the setup, which is

$$\delta\lambda = (0.14 \pm 0.01)\,\text{nm} \tag{50}$$

at a wavelength of approximately $67.80\,\text{nm}$.
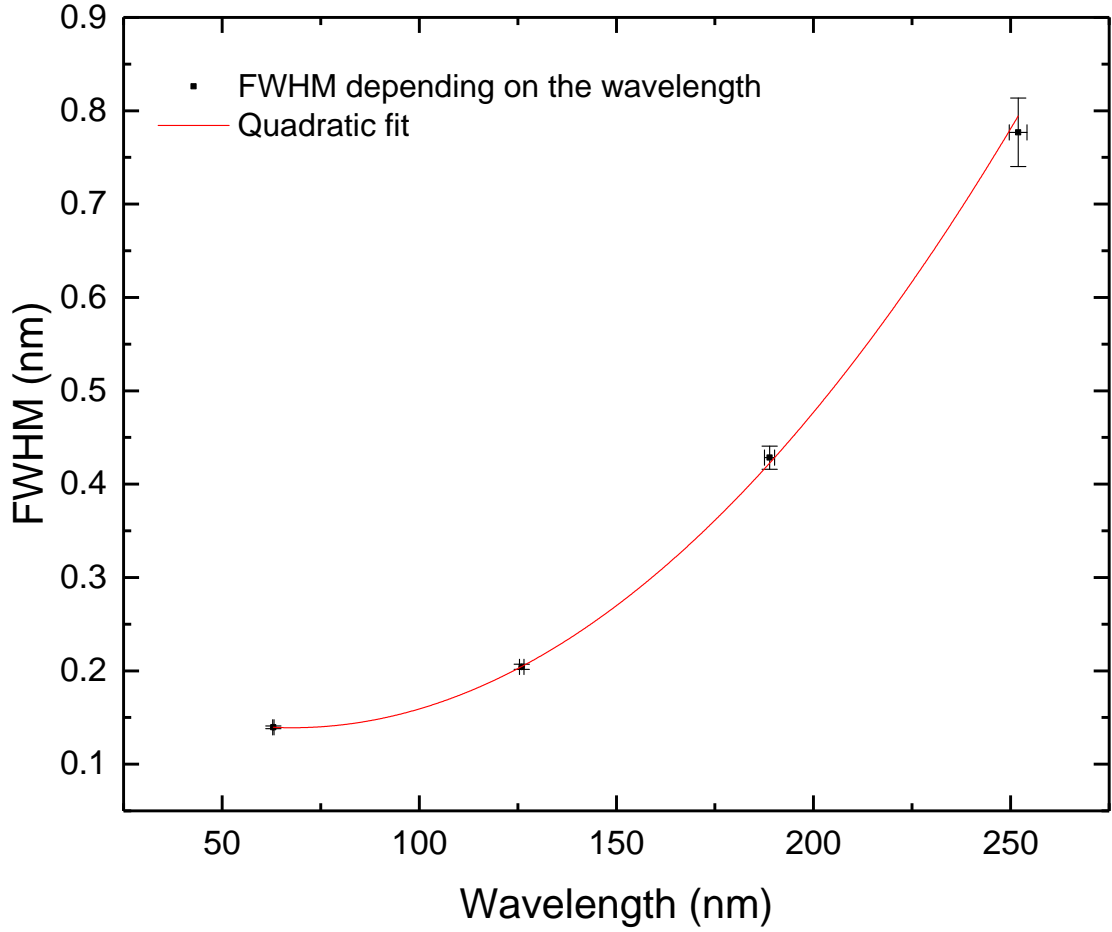

Figure 30: Simplified plot of the FWHM of the spectral peaks depending on the wavelength. The dataset was obtained from the measurement at $110\,\text{eV}$. Only a line at $62.973\,\text{nm}$ and its higher order reflections were used. An important feature that can be seen here is the increase in the uncertainties with the wavelength.

This result was revisited after a thorough identification of spectral peaks (which the next sections will delve into). Together with the rough estimate of the resolution previously obtained,
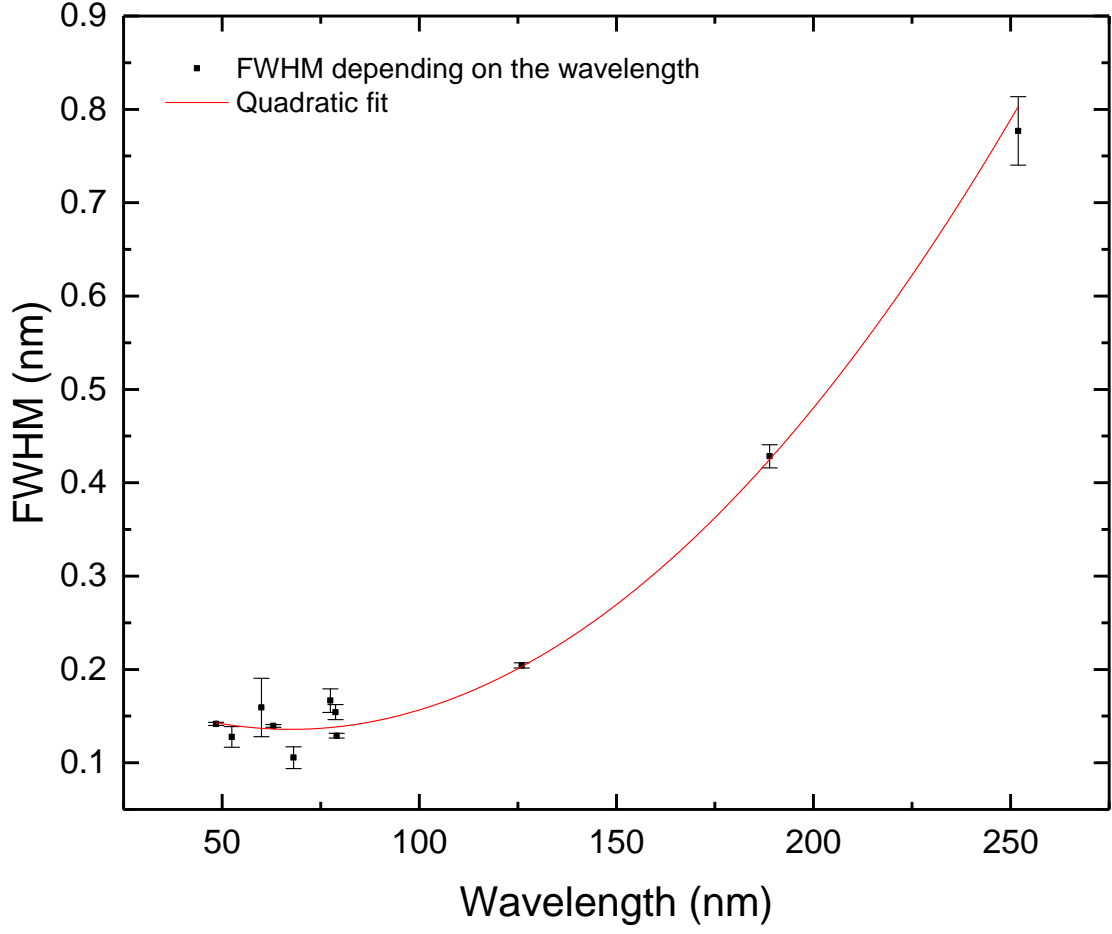
Figure 31: Complete plot of the FWHM of the spectral peaks depending on the wavelength. The dataset was obtained from the measurement at $110\,\mathrm{eV}$. The resolution can be regarded as equivalent to the FWHM in this context.

line identification allowed for a critical selection of peaks composed of single lines. In this manner, needless distortion of the results due to blended lines was to be avoided. Following the same procedure as for the rough analysis, the fit parameters obtained for a function of the form

$$y = a * x^2 + b * x + c, \tag{51}$$

were

$$a = 1.96(2) * 10^{-5}\,\frac{1}{\mathrm{nm}},\ b = -0.0026(3),\ c = 0.23(2)\,\mathrm{nm}, \tag{52}$$

which yielded a resolution limit of

$$\delta\lambda = (0.14 \pm 0.03)\,\text{nm} \tag{53}$$

at a wavelength of approximately 67.33 nm. The overlap between the two results is clear. The reason for the larger error bar in the latter analysis stems from the increased amount of data points scattering to both sides of the resulting fit curve in the region of the minimum.

Table 5: Resolution of the setup depending on the wavelength regime. The left column displays the wavelength regime, the right column shows the values between which the resolution of the setup is encased.

Wavelength regime (nm)	Interval of resolution (nm)
0 - 20	0.22 - 0.18
20 - 40	0.18 - 0.15
40 - 60	0.15 - 0.14
60 - 80	0.14
80 - 100	0.14 - 0.16
100 - 120	0.16 - 0.19
120 - 140	0.19 - 0.24
140 - 160	0.24 - 0.30
160 - 180	0.30 - 0.39
180 - 200	0.39 - 0.48
200 - 220	0.48 - 0.59
220 - 240	0.59 - 0.72
240 - 260	0.72 - 0.86
260 - 280	0.86 - 1.02

Showcased in Tab.5, the wide gap in goodness of our setup depending on the wavelength regime is worthy of mention. In the regime from 200 nm to 280 nm, it becomes impossible to clearly resolve two lines less than 0.5 nm appart. This constitutes a major setback should this regime be crucial for future measurements. However, this was to be expected: attending to the informations on the blaze angle displayed in Tab.2, the reflection efficieny of the grating at large wavelengths is expected to be low. The optimal regime for this grating is found at around 80 nm, which 5 showcases clearly.

An important note is that data points beyond 100 nm for the quadratic fit are comparatively

scarce; a much more trustworthy fit could be obtained by employing appropriate ions with clearer spectral lines in that range. This should help to reduce the uncertainties of the fit. In any case, it should be mentioned that improvements are expected: the automatic adjustment of the MCP position depending on the grating angle should result in a flatter parabola with a lower offset, i.e. a better and more constant resolution throughout the whole range of wavelengths detectable by the spectrometer. The reason for this resides in the optimized focusing, which was so far lacking for the most part of the spectrum and only fulfilled for the regime around 60 nm. Optimized focusing should help narrow down the width of the diffraction lines and improve the resolution.
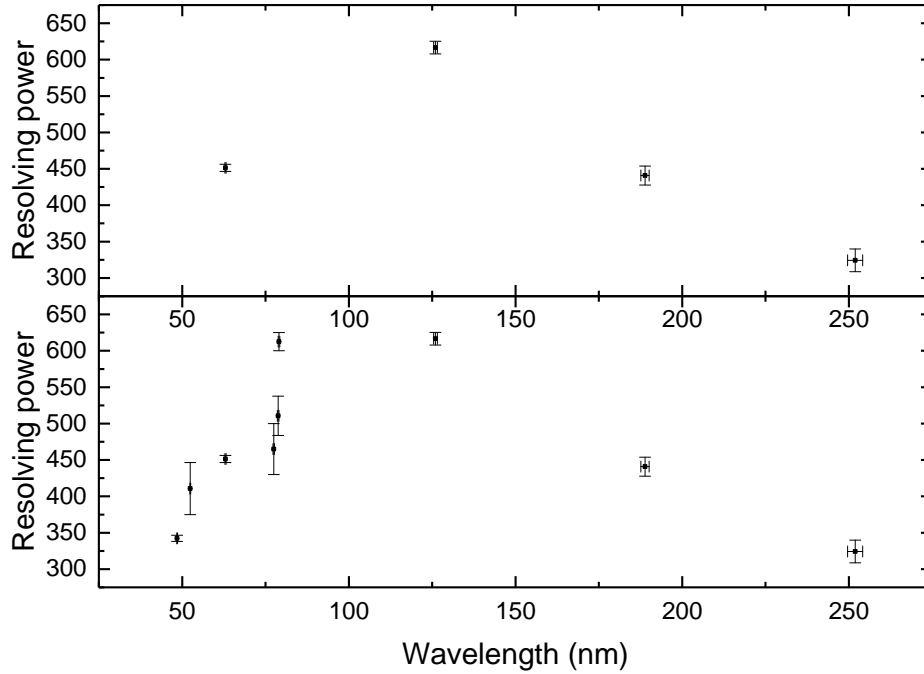

Figure 32: Rough (top) and complete (bottom) plots displaying the evolution of the resolving power along the spectrum. As in Fig.30, only one original peak and three further higher order reflections of the measurement at 110 eV were used for the rough analysis, while further individual peaks were added later.

A look at the resolving power R of the setup further supports the statements made on the goodness with which the setup operates. A rough analysis (see Fig.32, top) shows that it reaches

a maximum between 60 nm and 190 nm. The inclusion of additional data points (Fig.32, bottom) suggests to narrow down the regime to between 80 nm and 125 nm, achieving a resolving power of at least R = 617(9) as calculated for the peak at 125.9 nm. Naturally, this raises the question of why the maximal resolving power measured is not found closer to 80 nm. This could stem from an overestimation of $\delta\lambda$ for the line at around 80 nm, i.e. if the peaks attributed to single lines even after identification in chapter 7 were in fact blended peaks. The line at 125 nm, however, was a solitary one, hence its FWHM could be obtained much better. Measurements of ions with intense and well-resolved lines between 80 nm and 125 nm could, in any case, shed more light on this issue.

7 VUV data of oxygen - line identification

In this chapter, the analysis of the recorded spectra is discussed. In order to keep a good overview of what is a large amount of data, this chapter has been divided into four subsections. In 7.1, all of the initially identified lines up to O^{4+} are displayed in several tables together with information relevant to each observed transition (see Tab.6, 7, 11): a label to identify the line in the spectra; the charged state of the oxygen ion; the theoretical values of wavelength and photon energy. Further discussion of the findings takes place in 7.2. In 7.3, in a further table, the quantitative comparison of measured wavelengths and the literature values is displayed (Tab.10). In 7.4, lines not initially identified, which could be candidates for O^{5+} lines, are displayed in Tab.11 and 12 with all important pieces of information. The recorded spectra can be found in the appendix.

7.1 Overview of identified lines up to O^{4+}

The calibration process described in the previous chapter allowed for spectral analysis of the measurements performed on oxygen at several electron beam energies. The line positions in time channels were once again obtained by fitting Gaussian curves with the amplitude, the width and the mean as free parameters onto the spectral peaks, following the procedure outlined in [17]. The time channel positions were then converted into wavelengths; the wavelength uncertainties followed from Gaussian error propagation. Should new calibrations be performed in the future, this procedure allows to easily draw from existent data in order to check the wavelengths of the peaks in already measured oxygen spectra. Fitting directly onto the wavelength spectra would not allow this, and spectra would have to be recorded yet again.

In the following, a tabular overview of the possible lines that were observed is presented. The peaks in the spectra are labeled with capital letters. Candidates for each of the lines have been listed. The wavelengths in bold indicate the wavelengths whose observation is believed to have been more probable on the basis of the line position and the relative intensity displayed by NIST.

Table 6: Tabular summary of the theoretical wavelengths that are believed to have been observed.

Line label	λ (nm) (NIST)	Photon energy (eV)	Charged state	LL conf.	LL term	UL conf.	UL term
A	**43.498**	28.50342	O^{2+}	$2s^22p^2$	$^1S_0$	$2s^22p(^2P^*)3s$	$^1P^*_1$
B	**50.7683**	24.42158	O^{2+}	$2s^22p^2$	$^3P^*_1$	$2s2p^3$	$^3S^*_1$
	50.8182	24.3976	O^{2+}	$2s^22p^2$	$^3P^*_2$	$2s2p^3$	$^3S^*_1$
C	**52.5795**	23.58033	O^{2+}	$2s^22p^2$	$^1D_2$	$2s2p^3$	$^1P^*_1$
D	53.78319	23.05259	O^{1+}	$2s^22p^3$	$^2D^*_{3/2}$	$2s2p^4$	$^2P_{1/2}$
	53.82636	23.03410	O^{1+}	$2s^22p^3$	$^2D^*_{5/2}$	$2s2p^4$	$^2P_{3/2}$
	53.8318	23.03178	O^{1+}	$2s^22p^3$	$^2D^*_{3/2}$	$2s2p^4$	$^2P_{3/2}$
	53.90855	22.99898	O^{1+}	$2s^22p^3$	$^4S^*_{5/2}$	$2s^22p^2(^3P)3s$	$^4P_{5/2}$
	53.95489	22.97923	O^{1+}	$2s^22p^3$	$^4S^*_{3/2}$	$2s^22p^2(^3P)3s$	$^4P_{3/2}$
E	55.333	22.40692	O^{3+}	$2s^22p$	$^2P^*_{1/2}$	$2s2p^2$	$^2P_{3/2}$
	55.4075	22.37679	O^{3+}	$2s^22p$	$^2P^*_{1/2}$	$2s2p^2$	$^2P_{1/2}$
	55.4514	22.35907	O^{3+}	$2s^22p$	$^2P^*_{3/2}$	$2s2p^2$	$^2P_{3/2}$
	55.5261	22.32899	O^{3+}	$2s^22p$	$^2P^*_{3/2}$	$2s2p^2$	$^2P_{1/2}$
F	**59.9598**	20.67789	O^{2+}	$2s^22p^2$	$^1D_2$	$2s2p^3$	$^1D^*_2$
G	60.8398	20.3788	O^{3+}	$2s^22p$	$^2P^*_{1/2}$	$2s2p^2$	$^2S_{1/2}$
	60.9829	20.33098	O^{3+}	$2s^22p$	$^2P^*_{3/2}$	$2s2p^2$	$^2S_{1/2}$

Table 7: Tabular summary of the observed (continuation of Table 6)

Line label	λ (nm) (NIST)	Photon energy (eV)	Charged state	LL conf.	LL term	UL conf.	UL term
H	60.97	20.33528	O^{2+}	$2s2p^3$	$^3D_2^*$	$2p^4$	$^3P_0$
	61.004	20.32394	O^{2+}	$2s2p^3$	$^3D_2^*$	$2p^4$	$^3P_1$
I	**62.973**	19.68847	O^{4+}	$1s^22s^2$	$^1S_0$	$1s^22s2p$	$^1P_1^*$
L	70.385	17.61514	O^{2+}	$2s^22p^2$	$^3P_2$	$2s2p^3$	$^3P_1$
	70.385	17.61503	O^{2+}	$2s^22p^2$	$^3P_2$	$2s2p^3$	$^3P_2$
M	71.85036	17.25589	O^{1+}	$2s^22p^3$	$^2D_{5/2}^*$	$2s2p^4$	$^2D_{5/2}$
	71.85663	17.25438	O^{1+}	$2s^22p^3$	$^2D_{3/2}^*$	$2s2p^4$	$^2D_{3/2}$
N	75.8678	16.34214	O^{4+}	$1s^22s2p$	$^3P_1^*$	$1s^22p^2$	$^3P_2$
	75.9441	16.32572	O^{4+}	$1s^22s2p$	$^3P_0^*$	$1s^22p^2$	$^3P_1$
	76.0228	16.30882	O^{4+}	$1s^22s2p$	$^3P_1^*$	$1s^22p^2$	$^3P_1$
	76.0445	16.30416	O^{4+}	$1s^22s2p$	$^3P_2^*$	$1s^22p^2$	$^3P_2$
	76.1128	16.28953	O^{4+}	$1s^22s2p$	$^1P_1^*$	$1s^22p^2$	$^1S_0$
	76.2003	16.27083	O^{4+}	$1s^22s2p$	$^3P_2^*$	$1s^22p^2$	$^3P_1$
O	**77.4518**	16.00792	O^{4+}	$1s^22s2p$	$^3P_1^*$	$1s^22p^2$	$^3P_0$

Table 8: Tabular summary of the observed (continuation of Tables 6 and 7)

Line label	λ (nm) (NIST)	Photon energy (eV)	Charged state	LL conf.	LL term	UL conf.	UL term
P	77.9734	15.90083	O^{3+}	$2s2p^2$	$^2D_{5/2}$	$2p^3$	$^2D^*_{3/2}$
	77.9821	15.89906	O^{3+}	$2s2p^2$	$^2D_{3/2}$	$2p^3$	$^2D^*_{3/2}$
	77.9912	15.8972	O^{3+}	$2s2p^2$	$^2D_{5/2}$	$2p^3$	$^2D^*_{5/2}$
	77.9997	15.89547	O^{3+}	$2s2p^2$	$^2D_{3/2}$	$2p^3$	$^2D^*_{5/2}$
Q	**78.7711**	15.73981	O^{3+}	$2s^22p$	$^2P^*_{1/2}$	$2s2p^2$	$^2D_{3/2}$
R	79.0109	15.69204	O^{3+}	$2s^22p$	$^2P^*_{3/2}$	$2s2p^2$	$^2D_{3/2}$
	79.0199	15.69025	O^{3+}	$2s^22p$	$^2P^*_{3/2}$	$2s2p^2$	$^2D_{5/2}$
S	**80.22**	15.45552	O^{3+}	$2s2p^2$	$^2S_{1/2}$	$2p^3$	$^2P^*_{3/2}$
	80.2255	15.45446	O^{3+}	$2s2p^2$	$^2S_{1/2}$	$2p^3$	$^2P^*_{1/2}$
T	83.2927	14.88536	O^{2+}	$2s^22p^2$	$^3P_0$	$2s2p^3$	$^3D^*_1$
	83.3742	14.87081	O^{2+}	$2s^22p^2$	$^3P_1$	$2s2p^3$	$^3D^*_2$
U	**83.5096**	14.8467	O^{2+}	$2s^22p^2$	$^3P_2$	$2s2p^3$	$^3D^*_2$
	83.5292	14.84322	O^{2+}	$2s^22p^2$	$^3P_2$	$2s2p^3$	$^3D^*_3$

7.2 Anomalies in the spectra - premature appearance of charged states

The first observation is that the peaks exhibited by our measurements generally correspond to transitions within the n = 2 shell. In fact, all but two of the identified lines correspond to mono-electronic transitions between $2s$ and $2p$ subshells, the only exceptions being two of the proposed transitions for line C. The further energetic splitting of the subshells provides a wide range of possible transitions, many of them very close enough energy-wise. This poses a challenge to the spectrometer, as a very good resolution is necessary to separate these lines.

Table 9: Ionization energies for according to the databases by J. Scofield [37] and NIST [38]. The NIST values were rounded up to the second decimal.

Charged state	Scofield I_p (eV)	NIST I_p (eV)
O	13.6	13.62
O^{1+}	35.1	35.12
O^{2+}	54.9	54.94
O^{3+}	77.3	77.41
O^{4+}	113.8	113.90
O^{5+}	138.1	138.12

A further observation is that, although the magnitude of the ionization energies was roughly confirmed (displayed in Tab.9), in some of the measurements lines belonging to the immediate next charged state appear prematurely. Two very clear examples are provided by the measurements at 50 eV and 70 eV of electron beam energy. At 50 eV, the emergence of O^{3+} is not expected. However, the clear detection of lines E, Q and R is a proof of its presence in the trap region. The measurement at 70 eV provided a clear peak of line I and a dim feature corresponding to line N, characteristic of the charged state O^{4+} and thus first expected at energies beyond 77.41 eV, according to NIST. These findings can stem from fundamentally two different sources:

- the real electron beam energy was either generally higher than the noted one, which depends on the accuracy of the power supply;

- the FLASH-EBIT managed to produce metastable states which were subject to further excitation and ionization before decay could occur.

To explore the first possibility, it is worth remembering that the electron beam energy arises

mainly from three contributions, i.e. the potentials of the cathode and the central drift tube as well as the common potential of the drift tube platform. A check of the data confirmed that, for all the measurements, the voltages added up to the noted beam energy: the central drift tube and the platform were always driven at $0\,V$, whereas the cathode would be set at the negative value of the requested electron beam energy. Furthermore, the contributions arising from the space charges of the beam and the ion cloud cannot provide a satisfying explanation: the space beam potential only lowers the beam energy, and the ion cloud potential can only partially counteract the latter effect. The possible explanation for an increased electron beam energy has to be based on inaccuracies of the power supply. Both the cathode and the central trap drift tube were considered as sources of these inaccuracies, proposing that the voltages displayed by the user interface could differ from the real voltages provided by the power supplies. Simple measurements of their output voltages with respect to the ground with a multimeter showed no significant discrepancies between the real and the displayed values - in no case a difference which could explain the observations.

The search for metastable O^{2+} and O^{3+} states required calculations of the energy levels and the radiative decay rates with the Flexible Atomic Code software (FAC) [39]. For these calculations, the $1s$ and $2s$ shells were defined as closed. Hence, only transitions of the electrons initially in the $2p$ shell would be considered. The excitation configurations taken into account range from those within the n = 2 shell, within which the vast majority of identified transitions took part, up to $3d$ and $4s$. The ground states were defined as $2p^2$ for O^{2+} and $2p$ for O^{3+}. The obtained levels and transitions were analyzed thoroughly in search of states which would only present very low decay rates[2].

For O^{3+}, one excited state alone with only one transition - to the ground state - came into question (marked in green in Fig.35). The decay rate was $4.34 * 10^{-4}\,s$, seven orders of magnitude lower than the next lowest rate. However, given the energy difference of only $0.05\,eV$ between the states, this finding did not provide a convincing explanation for the appearance of O^{4+} more than $7\,eV$ below the ionization energy of O^{3+}. In the case of O^{2+}, again one metastable state in the $2p$ shell was found. It had three possible decay channels, their decay rates found between $10^1\,s$ and $10^{-3}\,s$. Moreover, the energy difference of this state with respect to the ground state would be of almost $6.91\,eV$, according to FAC (slightly lower according to NIST, see Fig.34).

---

[2]The lifetime τ_i of a state i is proportional to the inverse decay rate λ_i.

O^{2+} ions in this state could very well be ionized by the electron beam at $50\,\mathrm{eV}$, prompting the premature appearance of O^{3+}.

In the following, Grotrian diagrams (Fig.33-36) displaying the observed transitions and the discussed metastable states have been plotted as a further overview.
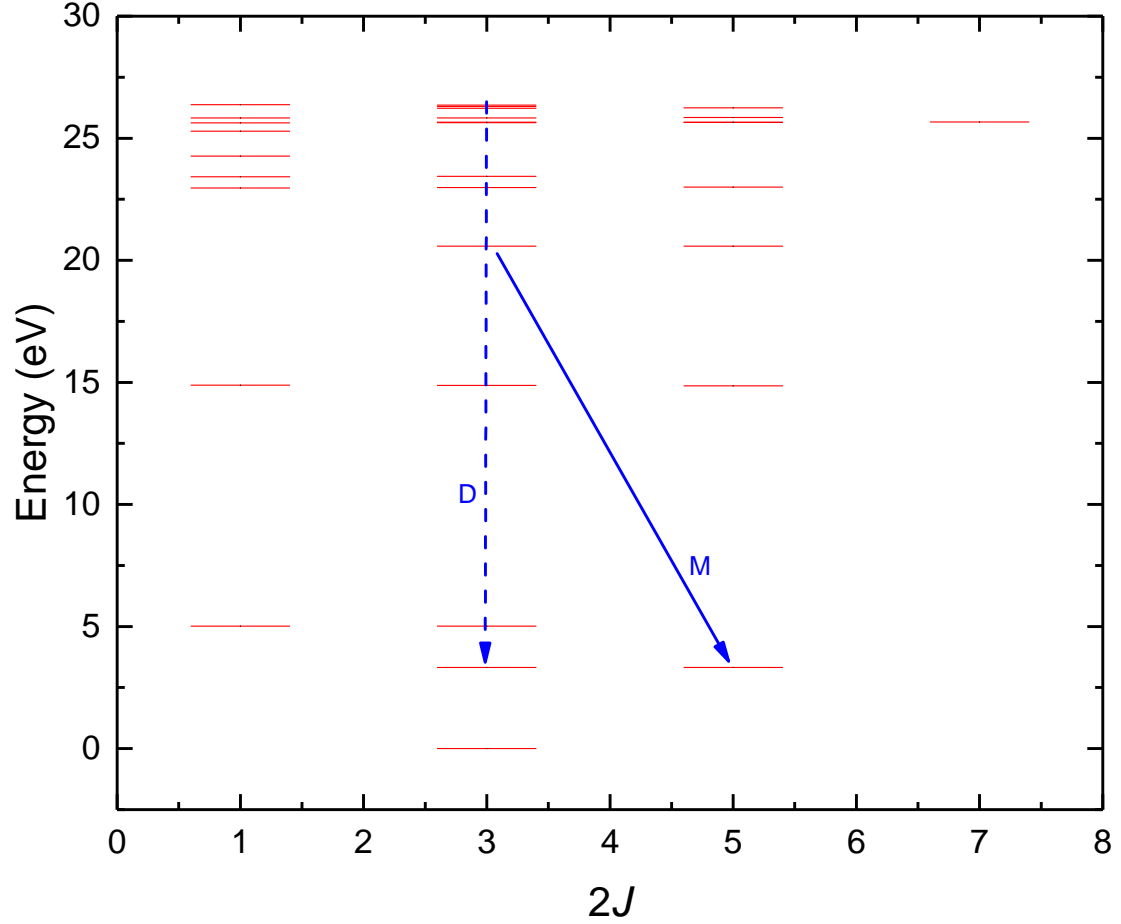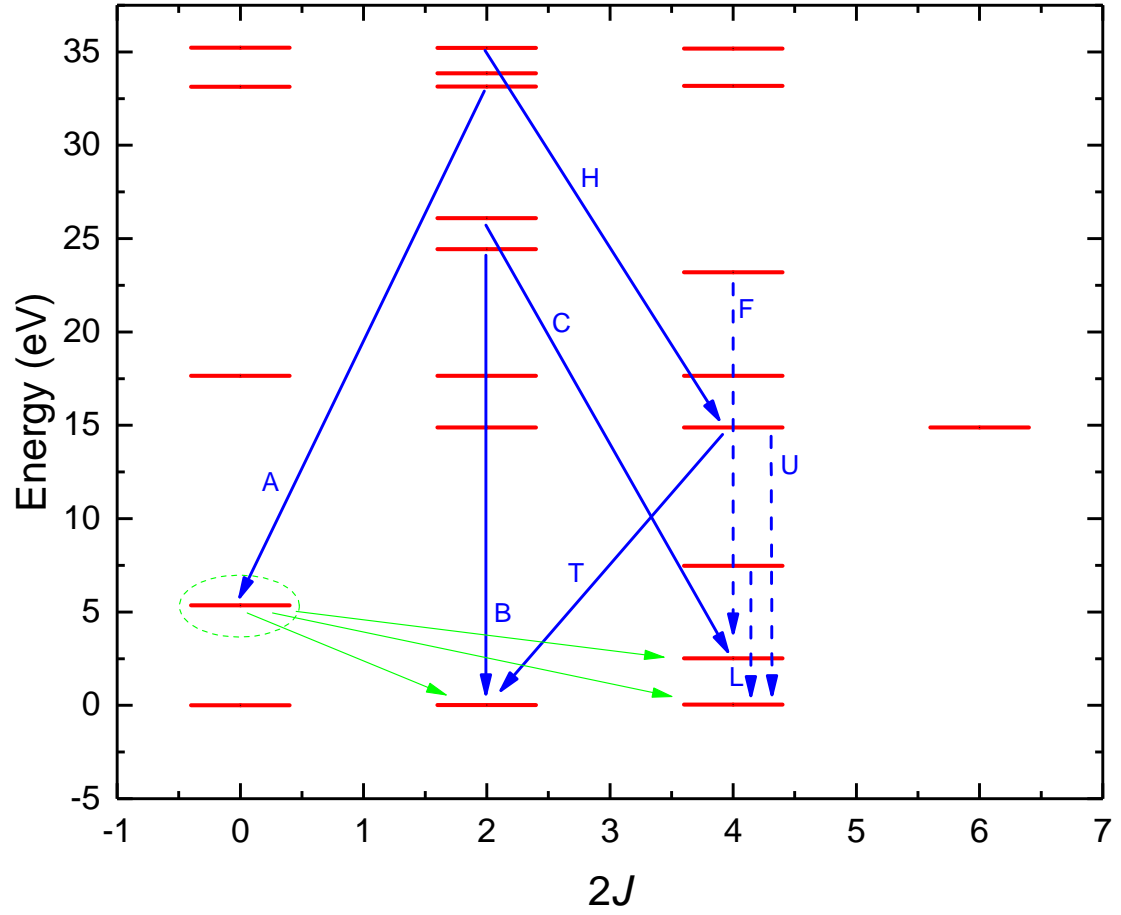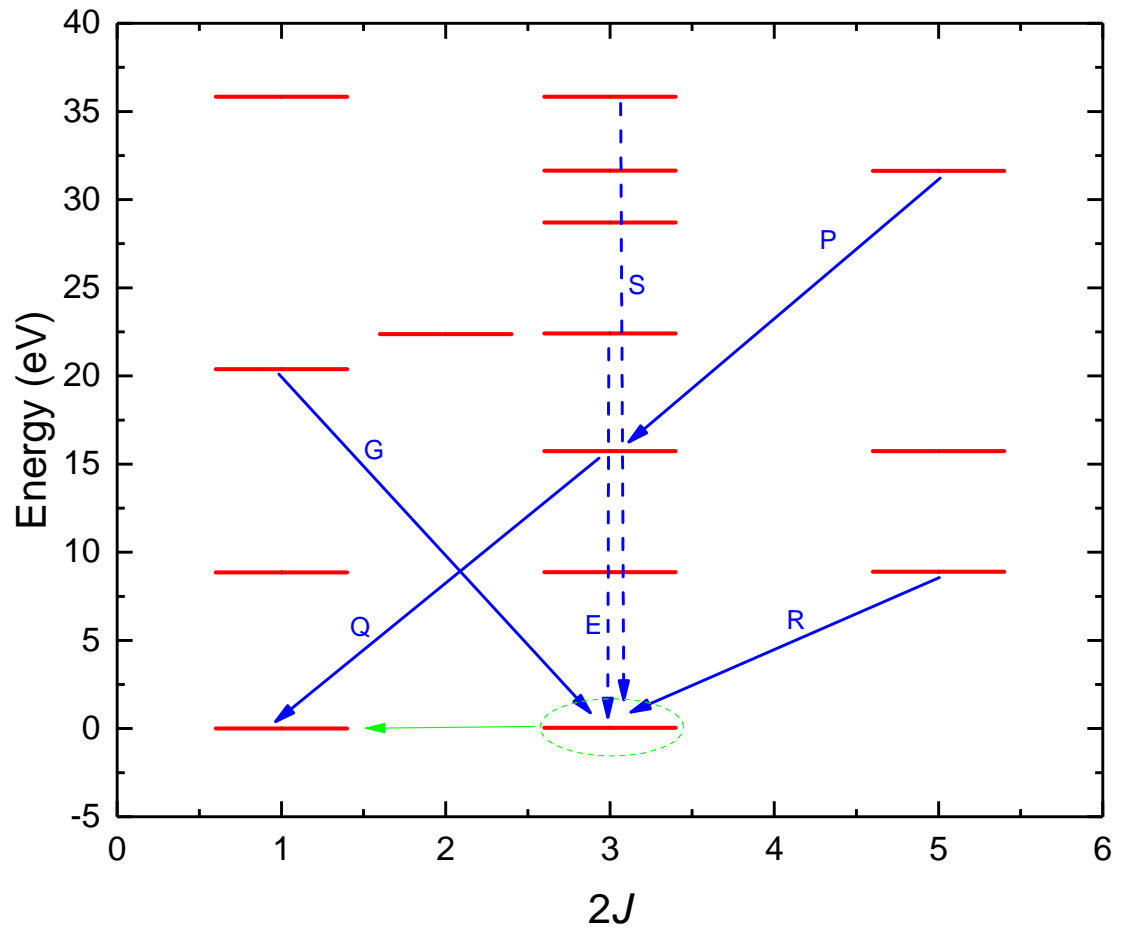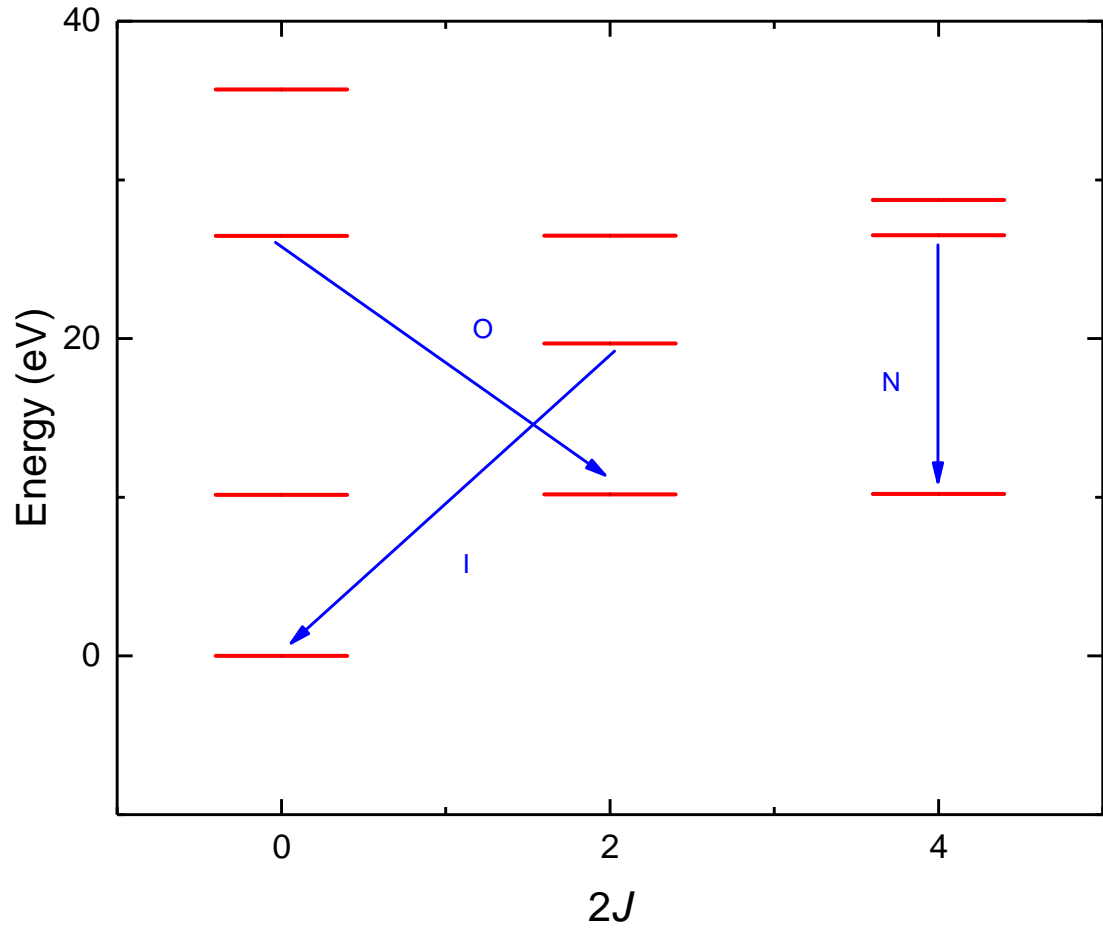

Figure 33: Energy levels of O^{1+} displayed in a Grotrian level diagram. The identified transitions from Fig.10 relevant for this charged state are marked with arrows and labeled with capital letters.

Figure 34: Energy levels of O^{2+} displayed in a Grotrian level diagram. The identified transitions from Fig.10 relevant for this charged state are marked with blue arrows and labeled with capital letters. In green, the proposed metastable state and its transitions are marked.

Figure 35: Energy levels of O^{3+} displayed in a Grotrian level diagram. The identified transitions from Fig.10 relevant for this charged state are marked with blue arrows and labeled with capital letters. In green, the proposed metastable state and its transitions are marked.

Figure 36: Energy levels of O^{4+} displayed in a Grotrian level diagram. The identified transitions from Fig.10 relevant for this charged state are marked with arrows and labeled with capital letters.

7.3 Comparison of the measured wavelengths with literature values

In order to provide a comprehensible comparison between the measurement results and literature data from NIST, the measured values had to be processed. Given a spectrum i, the position x_i of a peak and its uncertainty Δx_i are obtained through the usual fitting procedure. After acquiring these data in all the spectra where the peak is visible, the weighted average and its uncertainty can be calculated [21],

$$\mu = \frac{\sum(\frac{x_i}{\Delta x_i^2})}{\sum(\frac{1}{\Delta x_i^2})}, \quad \Delta\mu = \sqrt{\frac{1}{\sum(\frac{1}{\Delta x_i^2})}}, \tag{54}$$

where the sum runs over the index i of the spectra. The results of this operation can be seen in Tab.10, where the columns "λ (nm)" and "Measured λ (nm)" contain exactly this information. The last column displays the deviation of the literature value from the weighted average of our measurements in terms of the obtained uncertainty. This column allows us to draw some conclusions on the quality of the measurements and identification. For example, none of the identified peaks display a discrepancy beyond three sigmas between the NIST and the measured value. If the measured values for a line can be assumed to scatter around the real value following a normal distribution, the former are found around the latter within the uncertainty interval with a probability of over 0.997. This should be deemed a very positive result.

Table 10: Comparison of the measured and identified wavelengths with literature values from NIST. The fifth column displays the difference between the literature value from NIST and our experimental value.

Line label	NIST λ (nm)	Measured λ (nm)	Measured Δλ (nm)	Difference lit-exp (nm)	Deviation (σ)
A	43.4980	43.47064	0.02094	0.02736	1.30659
B	50.7683	50.76707	0.05366	0.00123	0.02292
C	52.5795	52.41363	0.06234	0.16587	2.66076
D	53.8318	53.85128	0.13004	-0.01948	0.14980
E	55.4514	55.42422	0.04057	0.02718	0.67010
F	59.9598	59.95507	0.05710	0.00473	0.08277
G	60.9829	60.96638	0.05483	0.01652	0.30138
H	61.0040	60.96638	0.05483	0.03762	0.68621
I	62.9730	62.98145	0.05141	-0.00845	0.16429
L	70.3850	70.35810	0.07944	0.02690	0.33855
M	71.8566	71.91722	0.20205	-0.06059	0.29988
N	76.0445	76.06424	0.07019	-0.01974	0.28126
O	77.4518	77.48237	0.11455	-0.03057	0.26688
P	77.9997	78.12524	0.07746	-0.12554	1.62062
Q	78.7711	78.80658	0.08346	-0.03548	0.42514
R	79.0199	79.08780	0.07157	-0.06790	0.94876
S	80.2200	80.16139	0.24317	0.05861	0.24102
T	83.3742	83.37555	0.26133	-0.00135	0.00518
U	83.5096	83.49536	0.09883	0.01424	0.14407

71

Three values, however, do differ from the NIST data by notably higher values than the rest. It is possible to argue that lines A, C, and P were wrongly identified. According to NIST, line A - a solitary O^{2+} line - could be surrounded by several O^{1+} peaks. However, the closest of them finds itself at $0.15\,\text{nm}$, which in this wavelength range corresponds exactly to the resolution of the setup. Hence, a wrong identification should not have happened as a result of the blending of these lines. Furthermore, at the electron beam energies measured, the presence of O^{1+} in the trap should be very unlikely.

The deviation of line C is even more difficult to explain, since the literature value provided in the table is the only one even close to the measured wavelength (even taking into account theoretical calculations, i.e. the Ritz wavelengths found in NIST). The detection of the line at energies as high as $150\,\text{eV}$ makes it unlikely for it to belong to O^{2+}. An alternative assignation would be possible: it could correspond to a W^{6+} line with a literature value for the wavelength of 52.5338 according to NIST. Tungsten is an expected background source. However, whereas the oxygen measurement at $110\,\text{eV}$ does show the line, the background measurement performed at the same energy does not. The lack of an appropriate peak in the background spectra also makes it impossible to deem the background as the origin line P, although its identification as an oxygen peak may also not be satisfying. Thes identifications remain therefore unclear.

Another observation is that there does not seem to be a bias in the deviations. From nineteen identifications, the measured value appears lower than the theoretical one ten times. In and of itself, it might be dangerous to draw conclusions from this. It is clear that the arbitrariness in obtaining the deviations in table 10 should not be underestimated. As tables 6, 7 and 11 show, in many occasions, one literature value had to be chosen among several ones which would have suited the measured wavelength well. In this sense, wrong identifications are possible. The choice depended on the proximity to our experimental value as much as on the relative intensity displayed by the NIST database, and often enough the choice was not clear. Assuming the arbitrariness in the choice of the literature value was the same throughout the identification process (even for the lines that were identified seemingly univocally in tables 6, 7 and 11), the unbiased distribution of the deviations seems to support the likewise unbiased nature of the calibration obtained in chapter 5. This is not to say that the calibration cannot be improved, as it certainly affects the order magnitude of the deviations. After all, the calibration uncertainties directly influence the uncertainties of the wavelengths.

7.4 Analysis of previously unidentified lines

The set of spectra recorded in the context of this thesis provided a number of lines (Tab.11, 12) which in first instance could not be identified as belonging to any of the oxygen ions up to O^{4+}. From this, five possibilities follow:

- known lines for oxygen ions up to O^{4+} were detected at wavelengths differing enough from literature values;

- the unidentified lines stem from other elements that entered the trap;

- known lines for oxygen ions up to O^{4+} were detected at unexpected intensities;

- lines for oxygen ions up to O^{4+}, not existent in known databases, were found;

- lines for O^{5+} were found.

Regarding the first option, it is possible to draw from the previous results to conclude that significant deviations of the obtained wavelengths from literature values are very unlikely. The measurements performed show consistent results all over the spectrum and there is no reason to suggest any malfunctions in the setup or missteps in the analysis of the data. The relevance of the second option cannot be understated, however. The fact that time constraints only allowed for the measurement of two background spectra at $110\,\text{eV}$ and $150\,\text{eV}$ constitutes a major setback for the identification of background sources. Reasonable suggestions for the latter are barium and especially tungsten, which can exit the gun and access the trap over time. A brief look at the two background spectra and the ionization energies shows that W^{3+}, potentially appearing at already $24\,\text{eV}$, could, in fact, originate lines X_7 and X_8. In this sense, the evolution of relative abundances of coexisting tungsten species as a function the electron beam energy might be an interesting topic of research, given the first appearance of these lines in a measurement that should permit the creation of the next three ionization stages (Fig.37).

Lines X_6 and X_7 however should not be dismissed as O^{5+} lines. Whereas the peaks can clearly be seen in the background spectra, it is undeniable that their intensities decrease to less than half the original intensity. For peaks consisting only of tungsten lines this does not make sense: closing the injection should not have any effect whatsoever on the tungsten abundance in the trap, since the only possible tungsten source resides in the electron gun. The intensity loss of the peaks could be explained if the peaks were consisting of several, blended lines belonging to appropriate tungsten and oxygen ions. NIST does provide two suggestions for the latter in

the form of Ritz wavelengths, i.e. theoretical calculations, which are attributed to O^{5+}. The wavelength difference between the tungsten and the oxygen lines in literature is not negligeable, but the comparatively large uncertainty in the measurement of these two peaks would allow this interpretation to be consistent. In any case, the resolution of the setup in this part of the spectrum should not permit resolving the oxygen and the tungsten peaks separately (Tab.5). It would also be possible to disregard tungsten completely and assign these peaks only to oxygen. Other clear oxygen lines are also still visible in the background spectra. This is only natural, since the vacuum in the trap is not absolute and oxygen may always enter the setup.
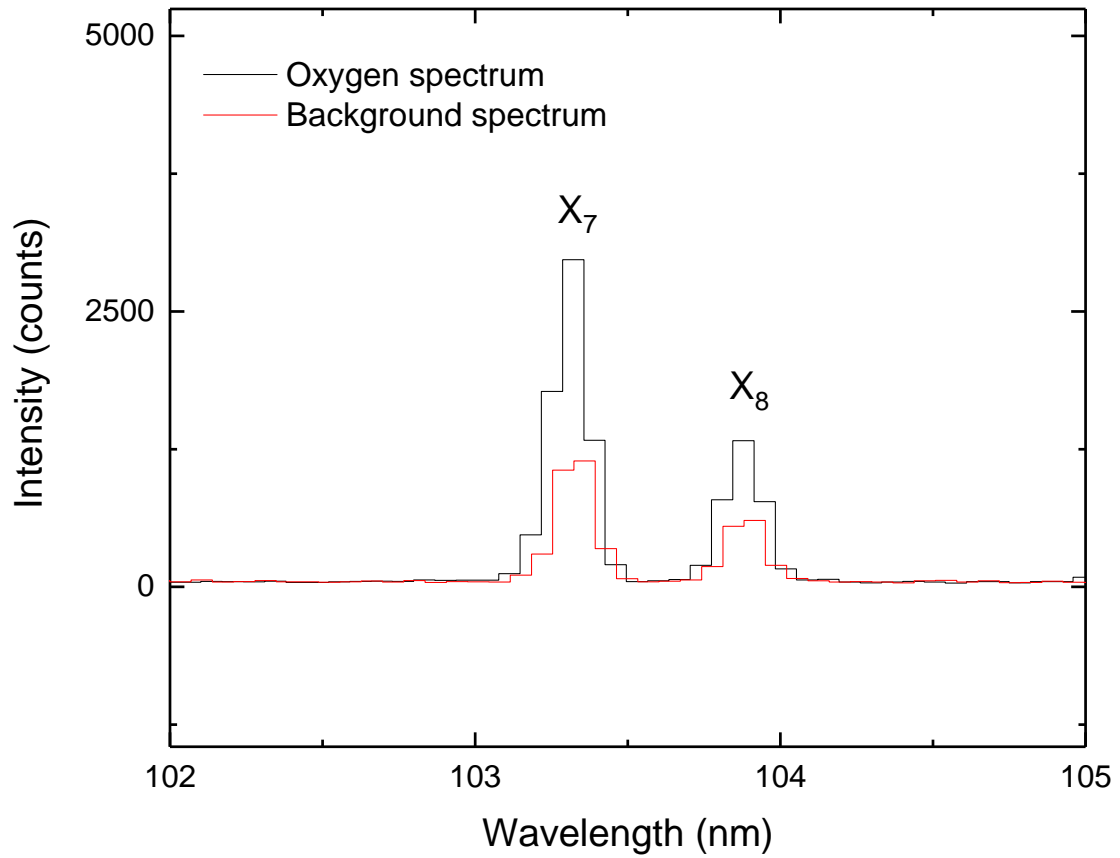
Figure 37: Oxygen and background spectra at a beam energy of $150\,\mathrm{eV}$ showing peaks X_7 and X_8.

Tables 11 and 12 display the wavelengths of other previously unidentified lines with proposed ions and transitions. Two further proposals for O^{5+} lines can be found in lines X_4 and Y_4.

Concerning X_4, the proposed literature value is the only one taken from an alternative database [40]; configuration and term data are largely missing for this transition. The same lack of information applies to Y_4, which did not coincide with any known data for oxygen, tungsten or barium. Line Y_3 is probably the same as line P in 10.

It should be noted that many of the proposed ions in these tables are unlikely to be the source of the observed lines. O, O^{1+} or W^{3+}, for example, should not be found in the trap at the energies at which the lines were detected - the charged states should, in fact, be much higher. More time and further work are necessary to provide a satisfying identification. Especially background measurements for more electron beam energies would be of advantage since the evolution of the lines in background spectra could clarify the charged states that originate the background lines.

Table 11: Tabular summary of the observed wavelengths with proposed identifications. The - represents missing information.

Line label	λ (nm) (exp.)	$\Delta\lambda$ (nm) (exp.)	Ion	LL conf.	LL term	UL conf.	UL term	λ (nm) (NIST)	Deviation (σ)
X_1	42.68147	0.04007	O^{1+}	$2s^22p^3$	$^2P^0_{1/2}$	$2s^22p^2(^1D)4d$	$^2D_{3/2}$	42.6537	0.69298
			Ba^{5+}	$5s^25p^3$	$^4S^0_{3/2}$	$5s^25p^2(^1D)4d$	$^2P_{1/2}$	42.6781	0.0840
X_2	48.48985	0.03994	O^{1+}	$2s^22p^3$	$^2D^0_{5/2}$	$2s^22p^2(^3P)3d$	$^2F_{5/2}$	48.5086	0.46957
X_3	71.4397	0.07537	O^{3+}	$2s2p(^3P^0)3d$	$^2F^0_{7/2}$	$2s^2(^1D)3d$	$^2F_{7/2}$	71.3573	1.09332
X_4	84.51422	0.1335	O^{3+}	$2s2p(^3P^0)3d$	$^2P^0_{3/2}$	$2p^2(^3P)3d$	$^2P_{1/2}$	84.4762	0.28478
			O^{3+}	$2s2p(^3P^0)3d$	$^2P^0_{1/2}$	$2p^2(^3P)3d$	$^2P_{3/2}$	84.584	0.52268
			O^{5+}	-	$^2D^0_{3/2}$	-	$^2P^0_-$	84.49	0.18141
			O^{5+}	-	$^2D^0_{5/2}$	-	$^2P^0_-$	84.50	0.10651
X_5	97.22389	0.15431	O	$2s^22p^4$	$^3P_2$	$2s^22p^3(^4S^0)4d$	$^3D^0_1$	97.1738	0.32461
X_6	97.83808	0.24691	O	$2s^22p^4$	$^3P_0$	$2s^22p^3(^4S^0)5s$	$^3S^0_1$	97.8617	0.09566
X_7	103.32385	0.13671	O^{5+}	$1s^22s$	$^2S_{1/2}$	$1s^22p$	$^2P^0_{3/2}$	103.1912	0.9703
			W^{3+}	$5d^3$	$^4F_{5/2}$	$5d^2(^3F)6p$	$^4P^0_{7/2}$	103.3221	0.01283
X_8	103.88840	0.13813	O^{5+}	$1s^22s$	$^2S_{1/2}$	$1s^22p$	$^2P^0_{1/2}$	103.7613	0.92013
			W^{3+}	$5d^3$	$^4F_{5/2}$	$5d^2(^1D)6p$	$^2D^0_{3/2}$	103.8917	0.02391

Table 12: Tabular summary of the observed wavelengths with proposed identifications (continuation of Tab.11). The - indicate the missing information as a result of not identifying the lines.

Line label	λ (nm) (exp.)	$\Delta\lambda$ (nm) (exp.)	Ion	LL conf.	LL term	UL conf.	UL term	λ (nm) (NIST)	Deviation (σ)
Y_1	65.54305	0.12251	Ba^{8+}	$4f5s$	$^3F_3^0$	$4f5p$	$^1F_3$	65.3987	1.17828
Y_2	74.27166	0.10647	-	-	-	-	-	-	-
Y_3	78.16245	0.11631	-	-	-	-	-	-	-
Y_4	106.55423	0.40986	-	-	-	-	-	-	-

8 Summary and outlook

The goal of the experiments carried out in the context of this thesis was to provide a characterization of the normal incidence monochromator spectrometer at the FLASH-EBIT. This characterization should provide a basis on which to expand with regards to future measurements of highly charged trans-iron ions.

Two parameters affecting both the data intake and the data analysis were updated in order to make full use of the setup. One of these parameters is the distance between the grating and the MCP. An optimal focus distance is of paramount importance, as well-resolved peaks may allow distinguishing blended lines from each other. It was possible to provide an expression for the optimal focus distance as a function of the wavelength. In the near future, this expression will be implemented into a computer program that will allow a motor to continuously adjust the position of the MCP as the grating rotates. In this way, an optimal focus for all wavelengths should be achieved, and hence a better resolution.

The other updated parameter was the angle by which the spectral lines appear tilted with respect to the vertical axis on the MCP. This angle greatly affects the data analysis, as the tilt correction is a necessary step in order to obtain the one-dimensional spectra that underlie the process of line identification. As long as the setup is not changed, the angle value obtained for the tilt should be employed for all the Python scripts performing the tilt correction and line projection. A calibration establishing a quantitative equivalence between wavelengths and positions along the dispersive axis was also provided in this thesis. The calibration was achieved by measuring and identifying lines of a well-studied element like oxygen. In particular, it was a measurement at $110\,\mathrm{eV}$ of electron beam energy and a trap depth of $\sim 50\,\mathrm{V}$ which provided a spectrum with enough clearly identifiable peaks to undertake the calibration procedure with success. This measurement also served as a basis for an analysis of the resolution achieved by the setup prior to the implementation of the program regulating the optimal focus distance between grating and MCP. Further measurements on oxygen at diverse electron beam energies were used to assess the quality of the calibration and the precision of the setup. The identification of lines in the interval 40-90 nm, for which the distance of the MCP with respect to the grating was optimized, showed no significant discrepancies with literature values as found in the NIST database. FAC calculations were performed in order to explain the premature appearance of the charged states O^{2+} and O^{3+}. Only for the former could a metastable state be found which provides a solid explanation. Lastly, the detection of lines which cannot be interpreted convincingly as background contributions

suggest the finding of at least two O^{5+}-transitions. These appear only as theoretical predictions in the NIST database; their detection would hence constitute a confirmation of the calculations.

The identification of lines in the ultraviolet regime of Tc^{3+}-Tc^{6+}, as expected to appear on the surface of the white dwarf RE 0503-289, is a long-term goal. Technetium experiments will be preceded by measurements on molybdenum and ruthenium. Drawing from predictions that arise from their similar nuclear charges and possible electronic configurations, these measurements will shed light on the mostly uncharted territory of trans-iron ion spectra and allow to predict the behaviour of technetium while preparations to inject a radioactive element continue.

Appendix

This section contains all of the oxygen spectra taken in for the sake of this thesis. All of the identified peaks have been labeled with their respective letters. The different colours correspond to different charged states - the legends on each spectrum display further information. A line of nth order is noted by $(n-1)$ asterisks, i.e. a first-order line has no asterisk, a second-order line has one asterisk and so on. For a better visualization of the peaks, the vertical axis was displayed logarithmically.

It should be noted that the spectra recorded at $160\,\text{eV}$ and $200\,\text{eV}$ displayed problems, probably arising during the processing of the data with the Python program. Due to this reason, both spectra are not shown here.
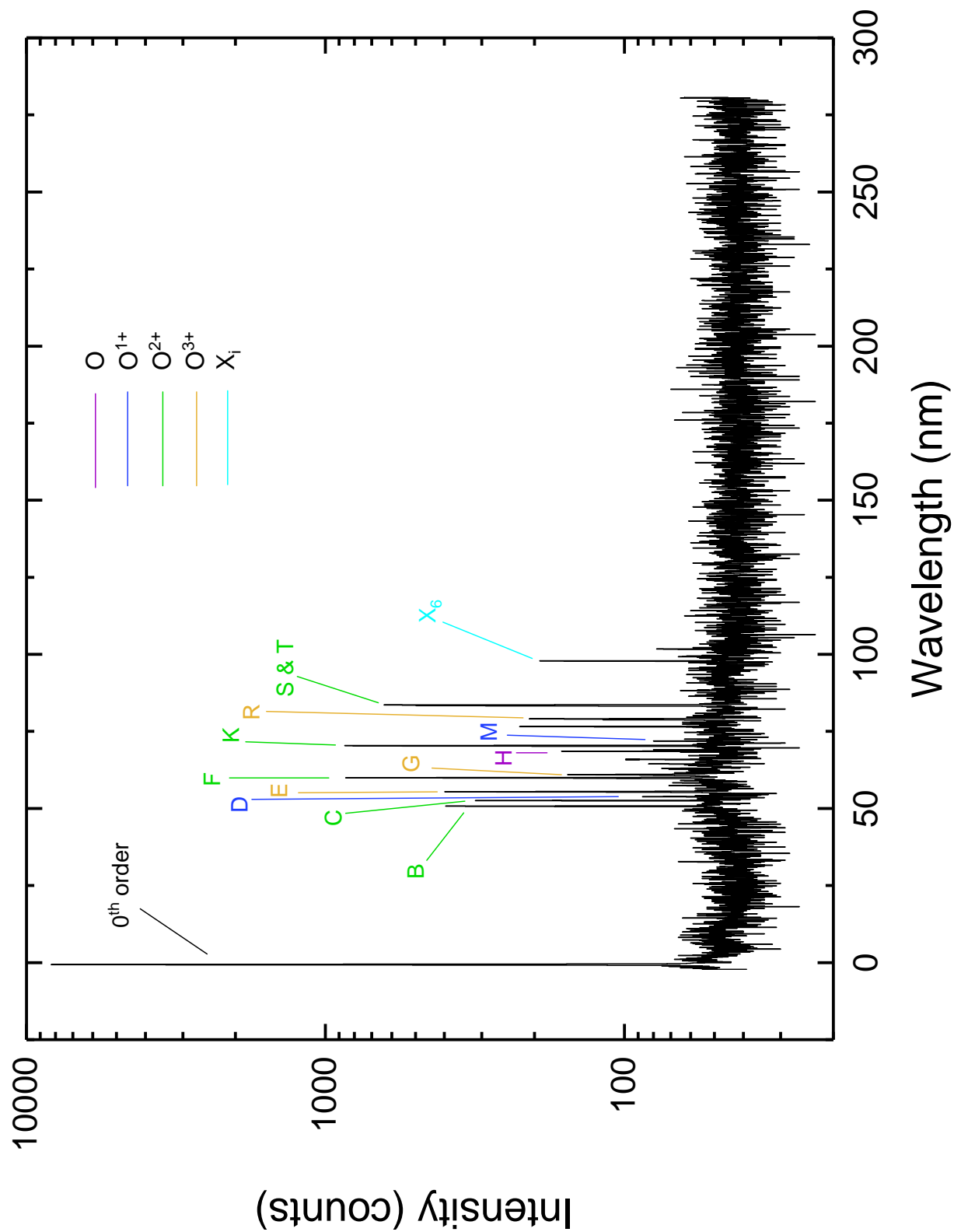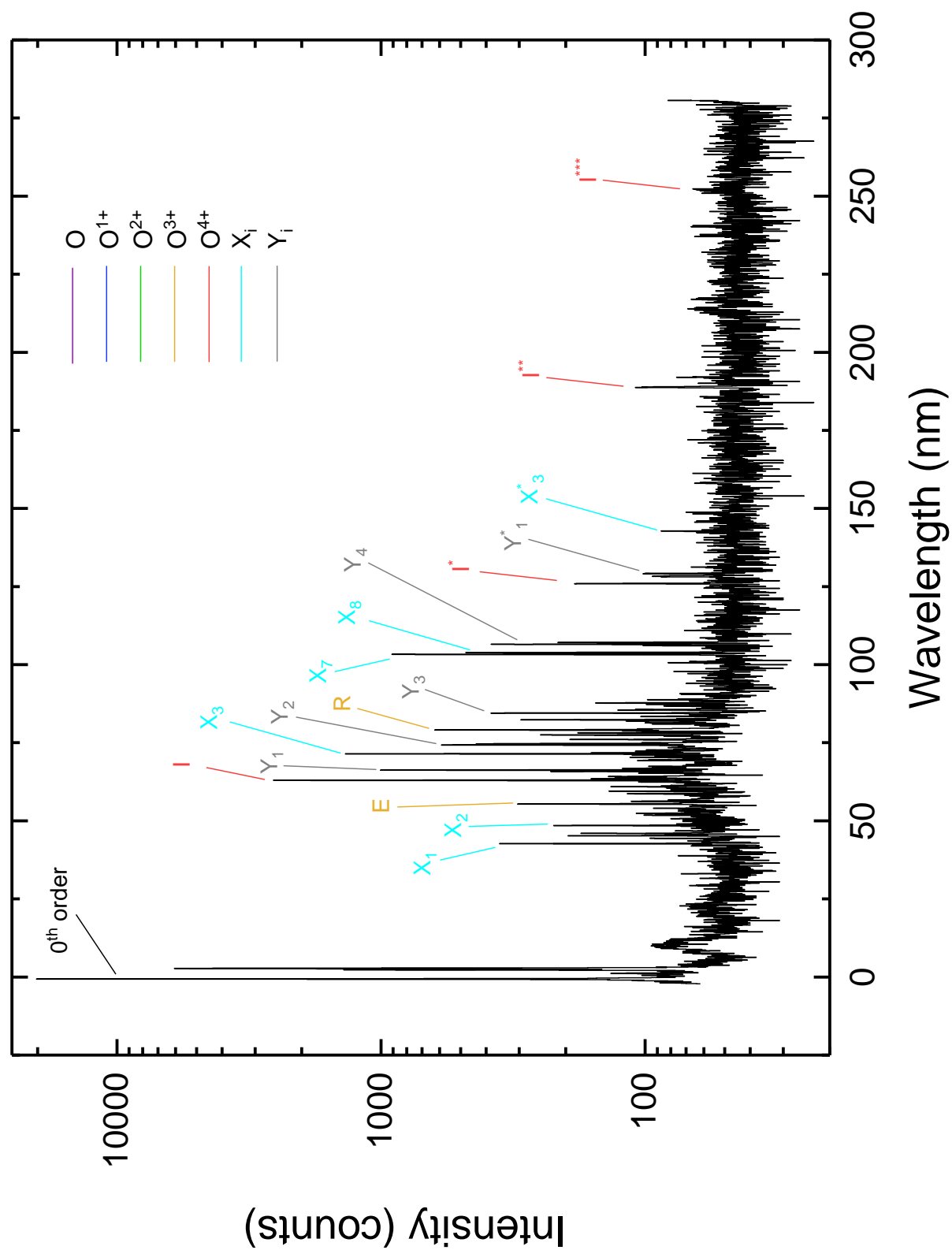
Figure 38: Spectrum of oxygen at an electron beam energy of 50 eV. Intensity displayed logarithmically.
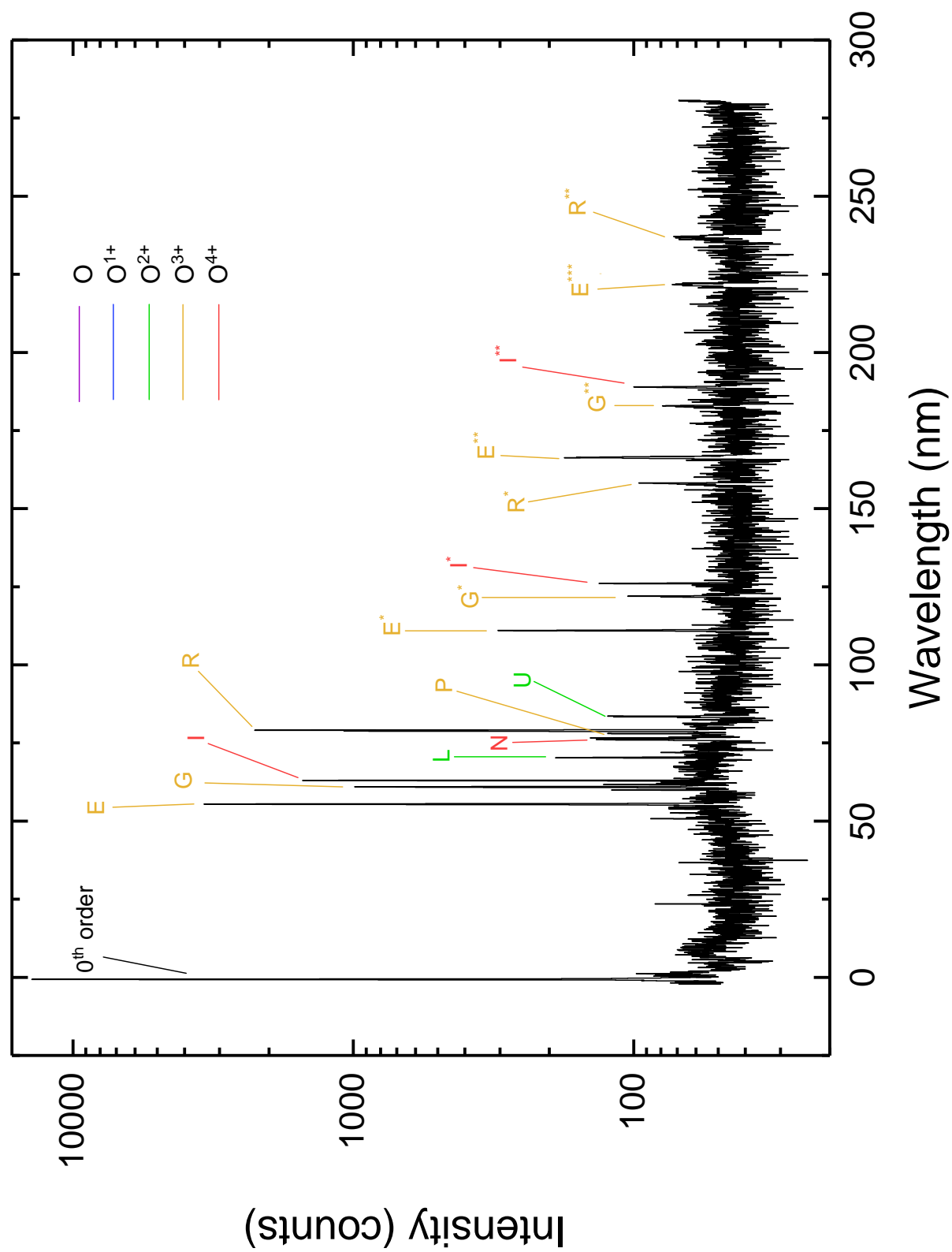
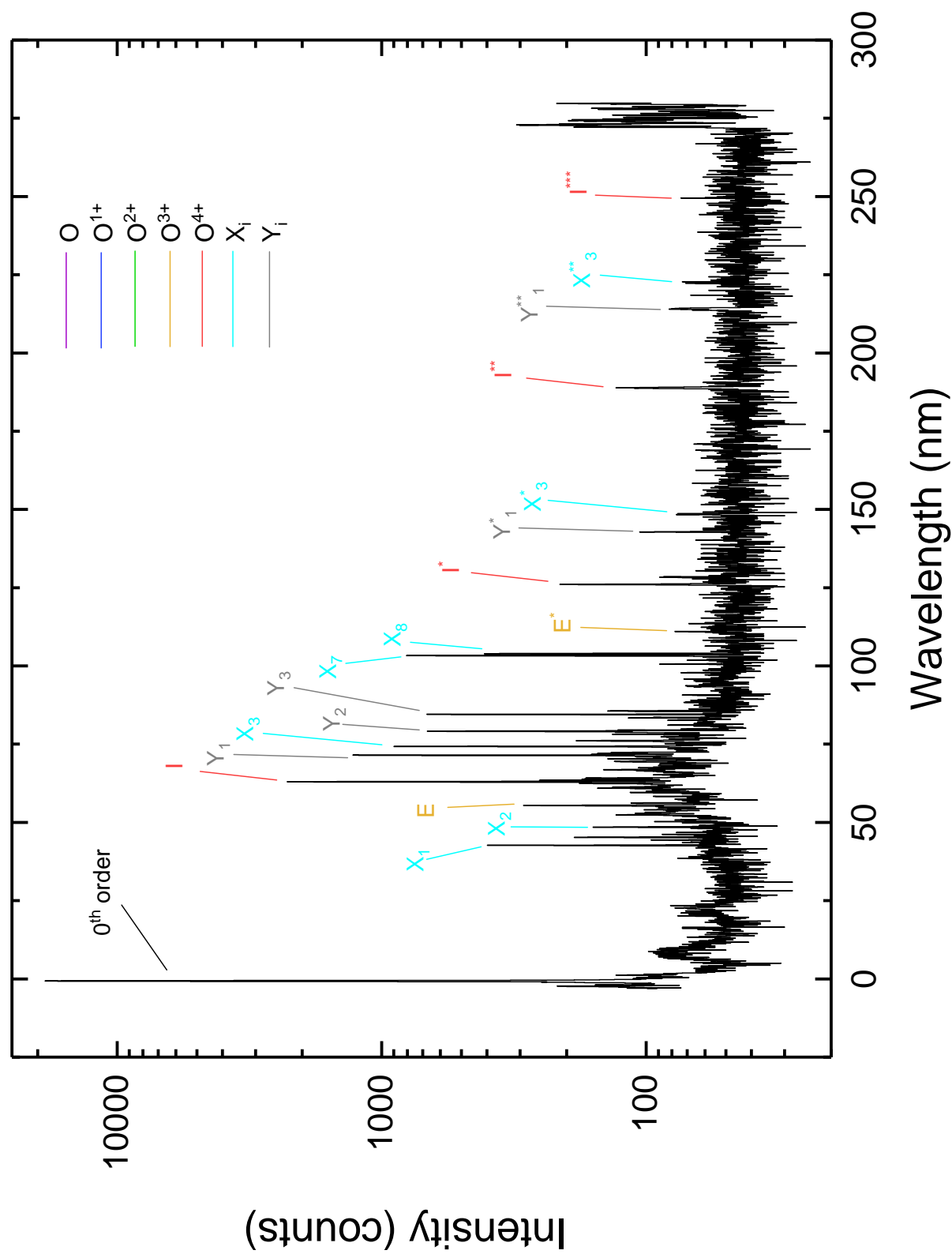Figure 39: Spectrum of oxygen at an electron beam energy of 70 eV. Intensity displayed logarithmically.
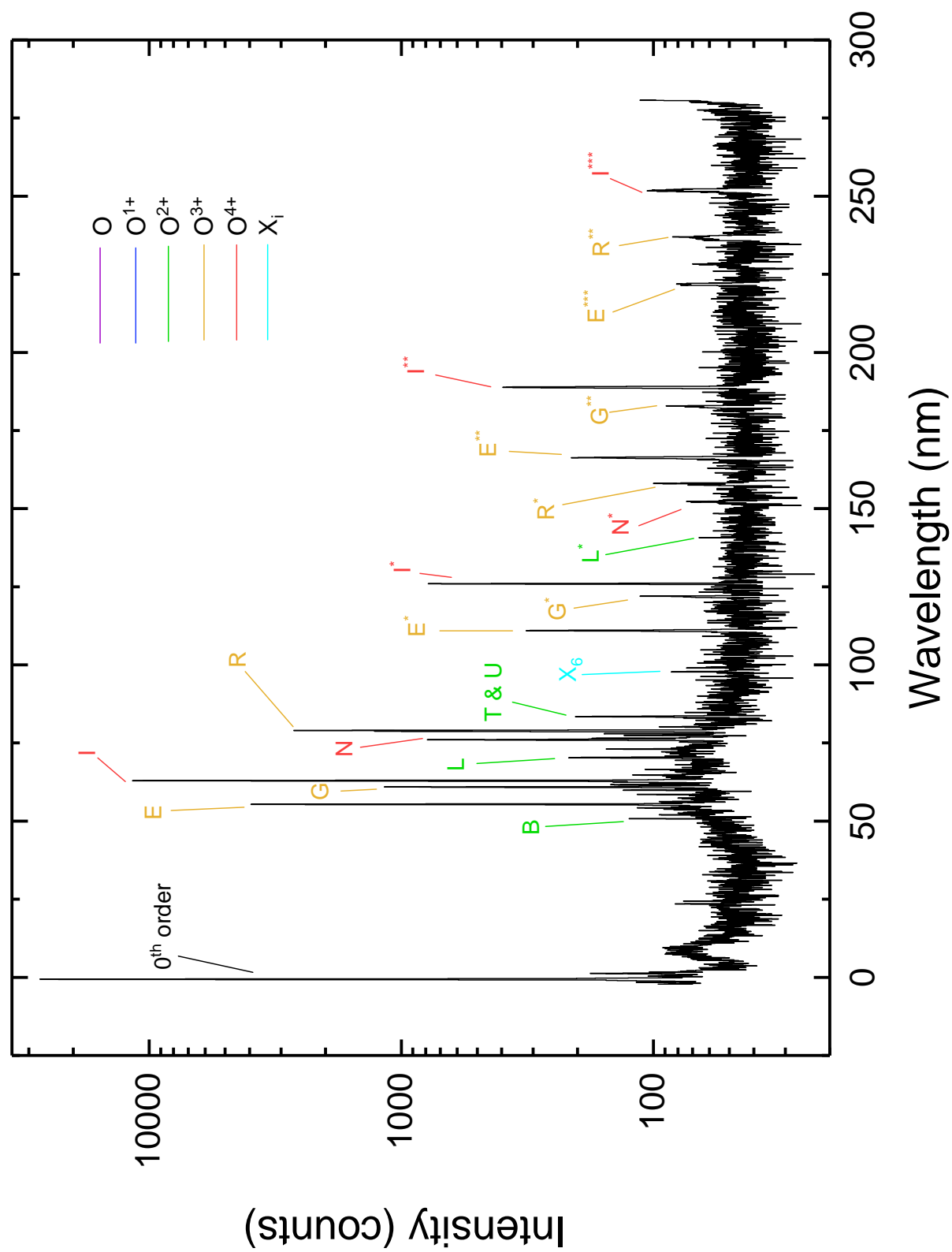
Figure 40: Spectrum of oxygen at an electron beam energy of 90 eV. Intensity displayed logarithmically.
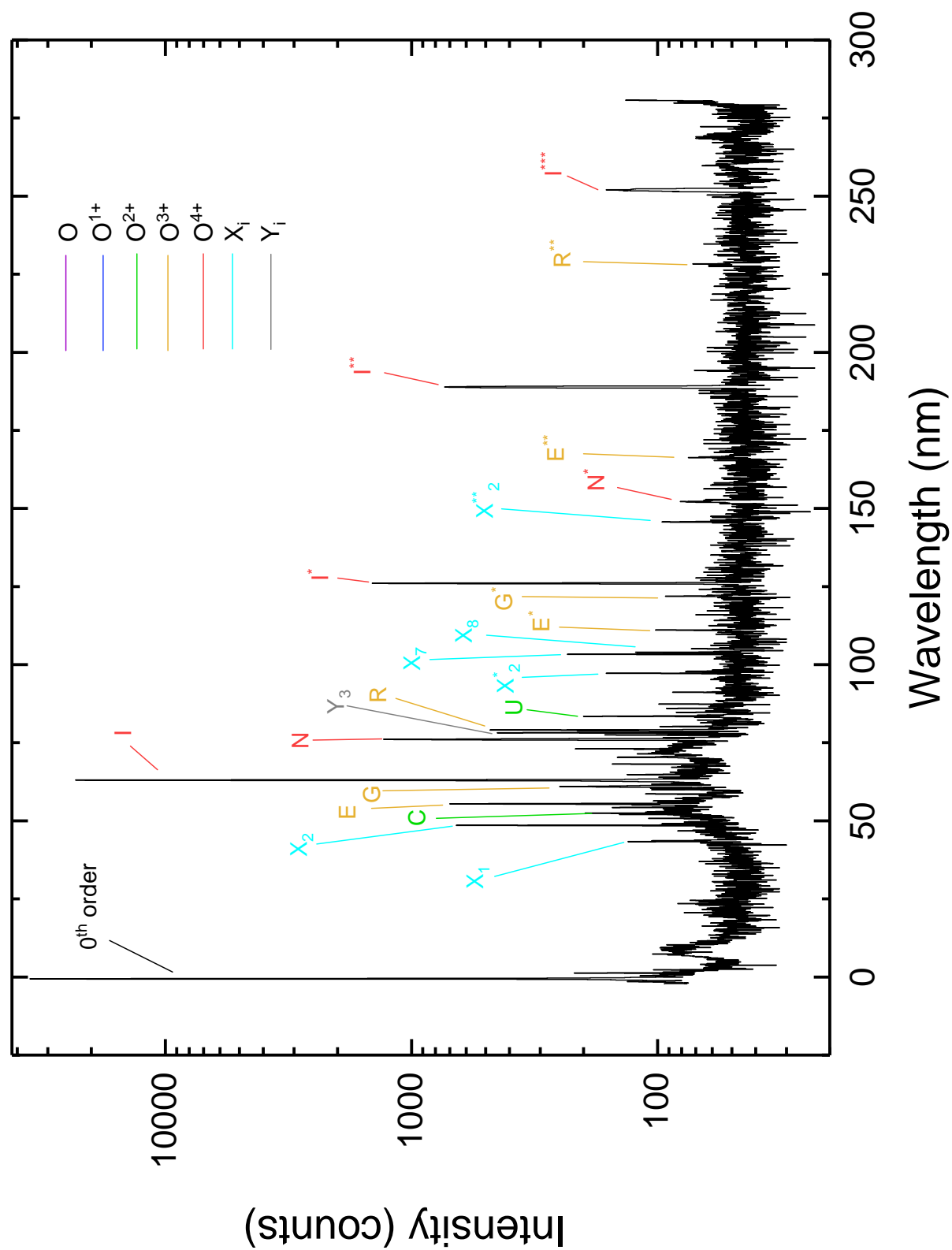
Figure 41: Spectrum of oxygen at an electron beam energy of 110eV.
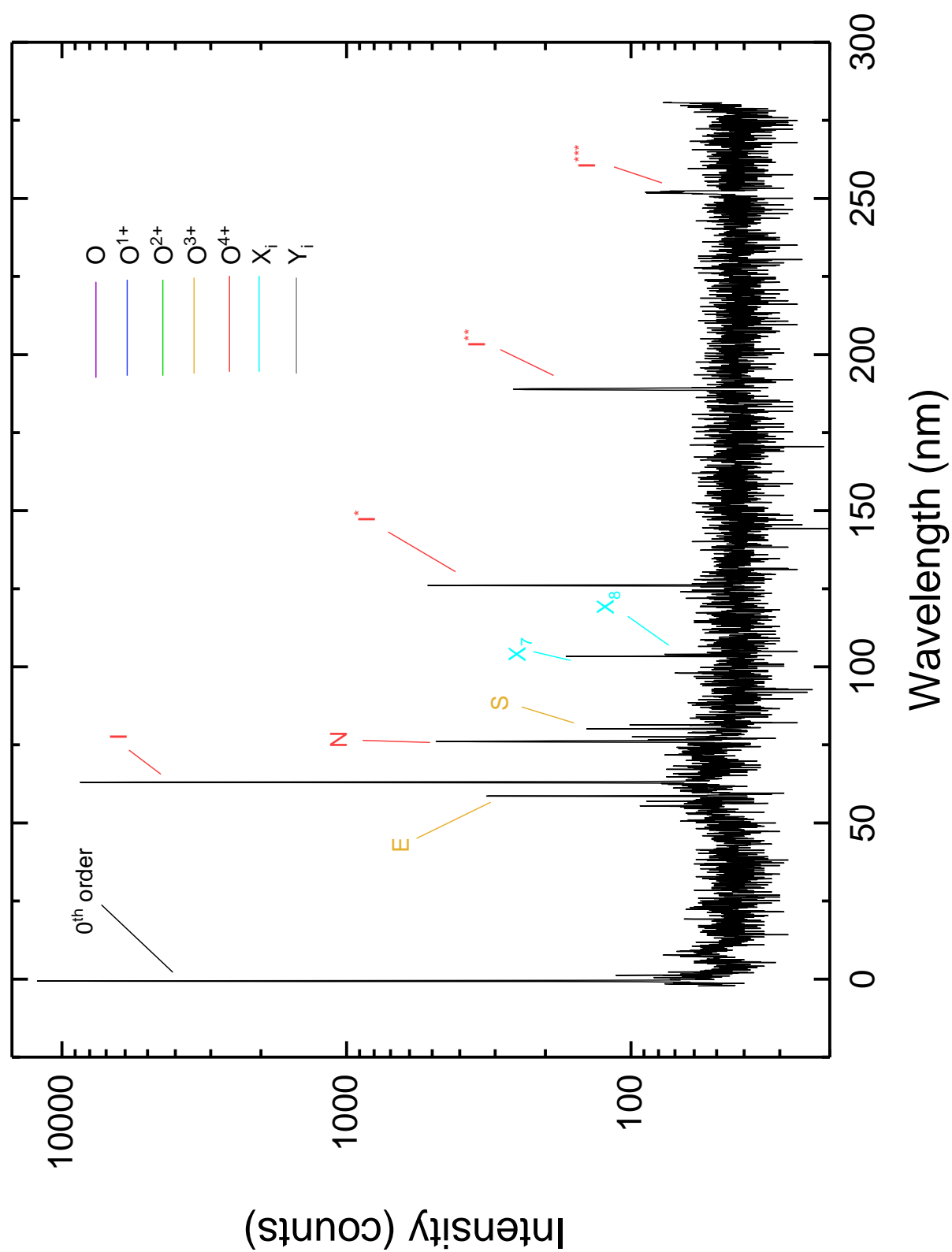
Figure 42: Background spectrum at an electron beam energy of 110 eV.
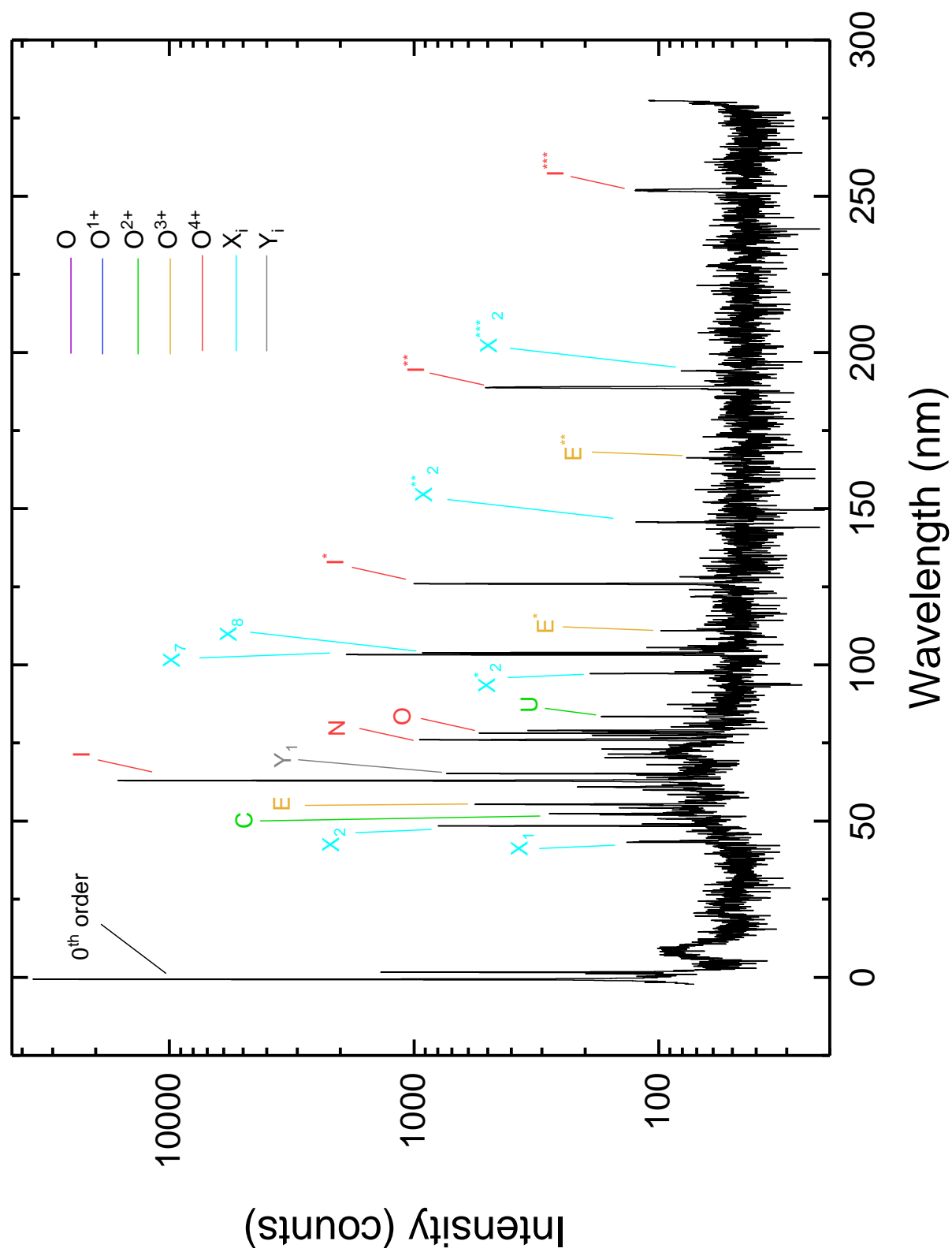
Figure 43: Spectrum of oxygen at an electron beam energy of 120 eV. Intensity displayed logarithmically.
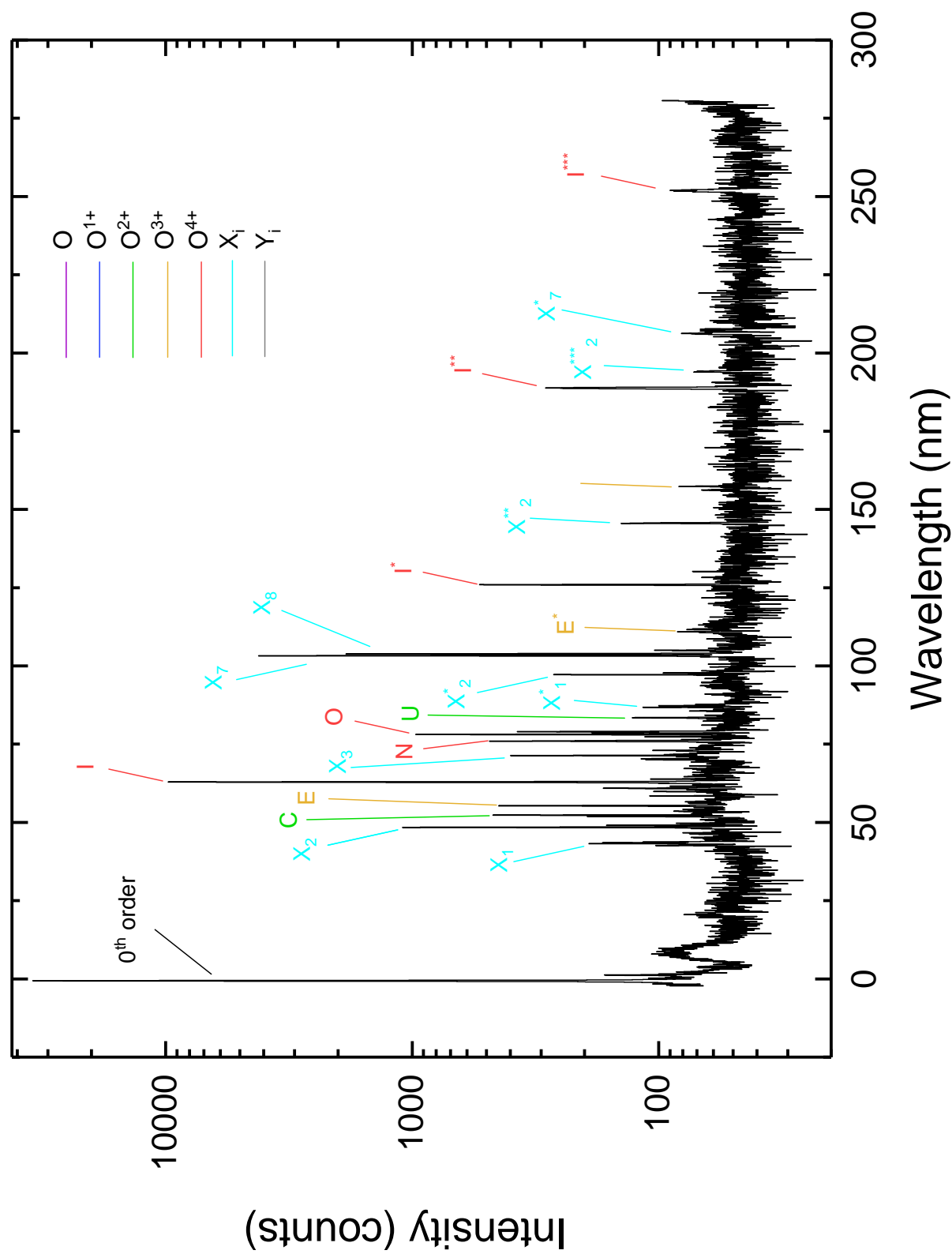
Figure 44: Spectrum of oxygen at an electron beam energy of 130 eV. Intensity displayed logarithmically.
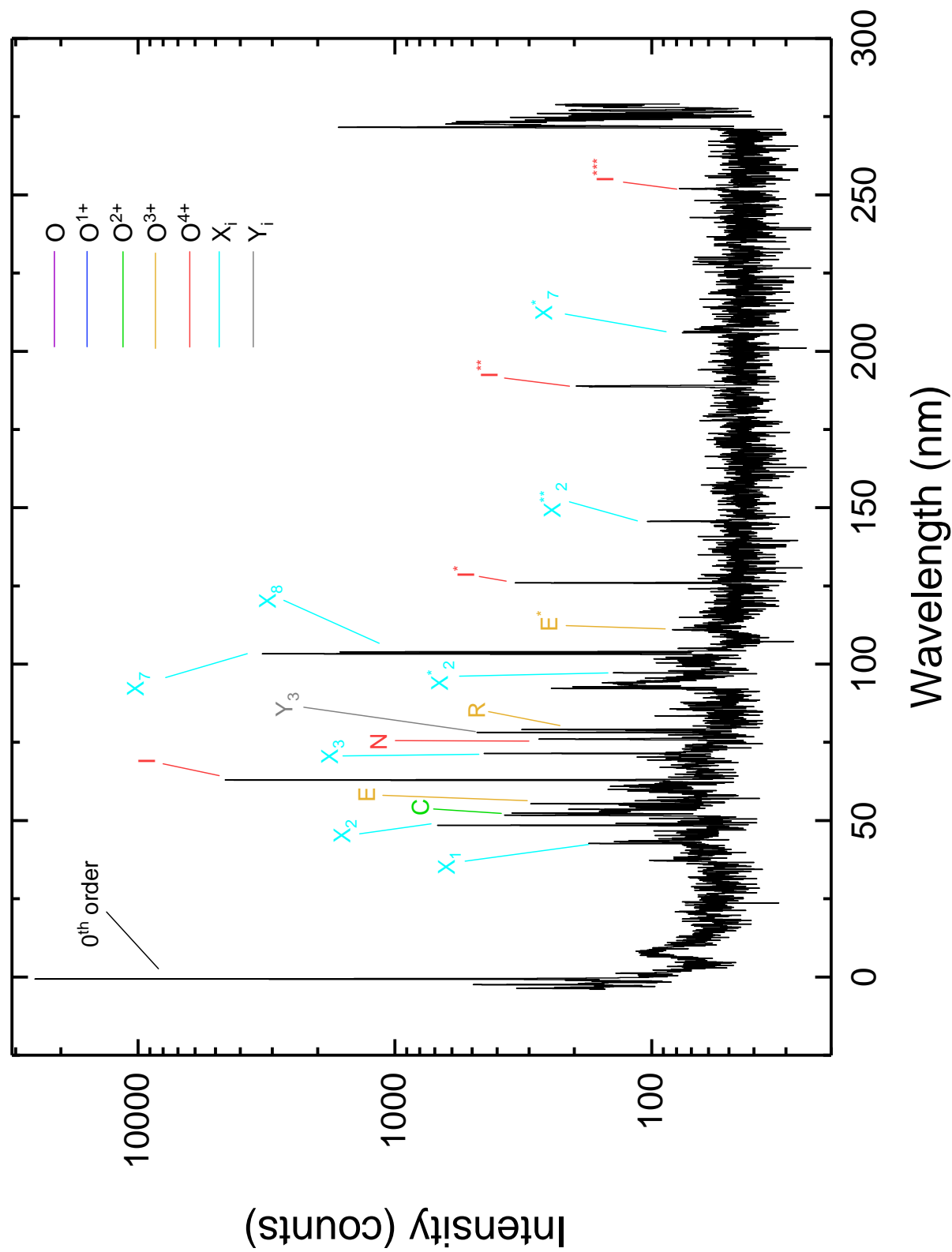
Figure 45: Spectrum of oxygen at an electron beam energy of 140 eV. Intensity displayed logarithmically.
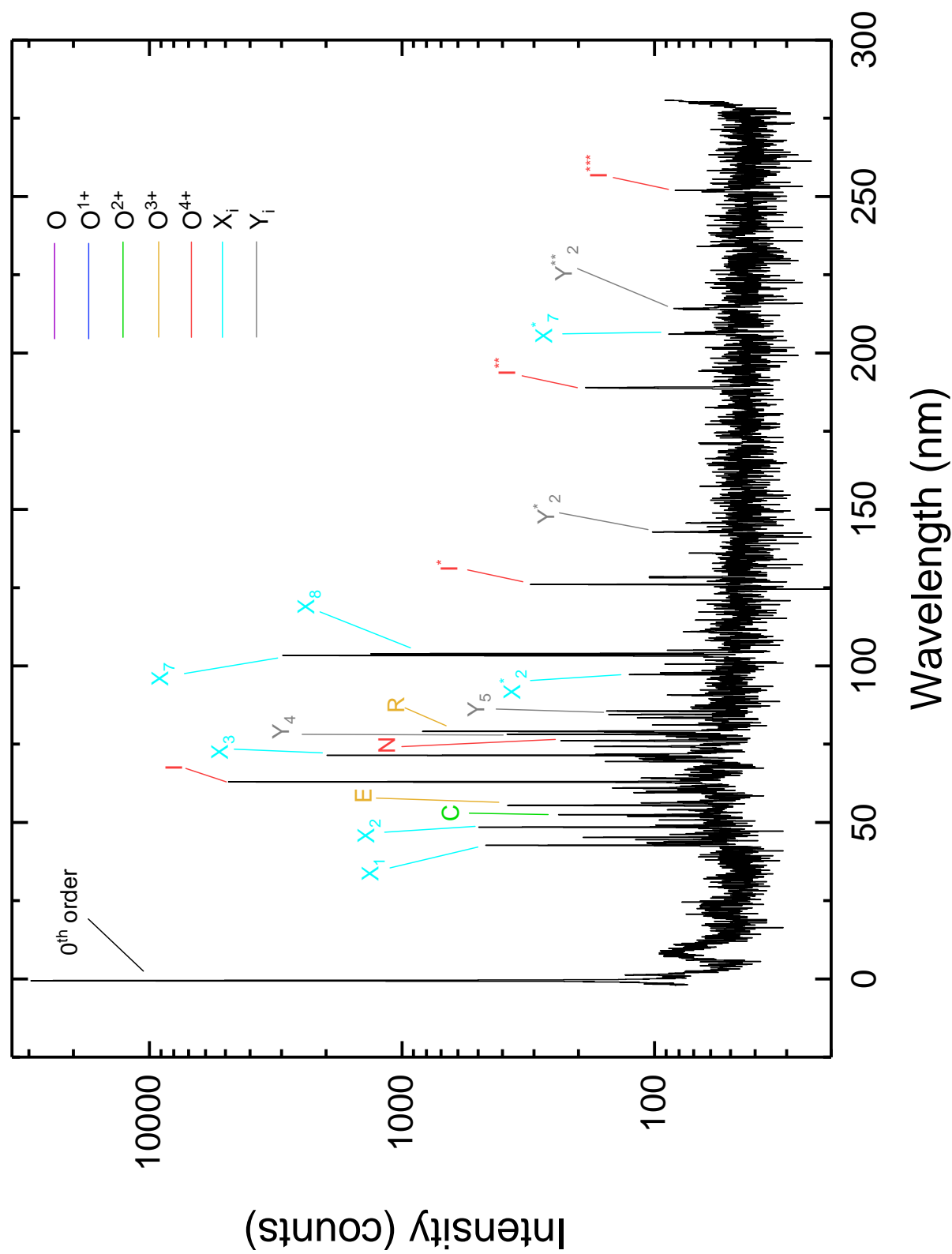
Figure 46: Spectrum of oxygen at an electron beam energy of 150 eV. Intensity displayed logarithmically.
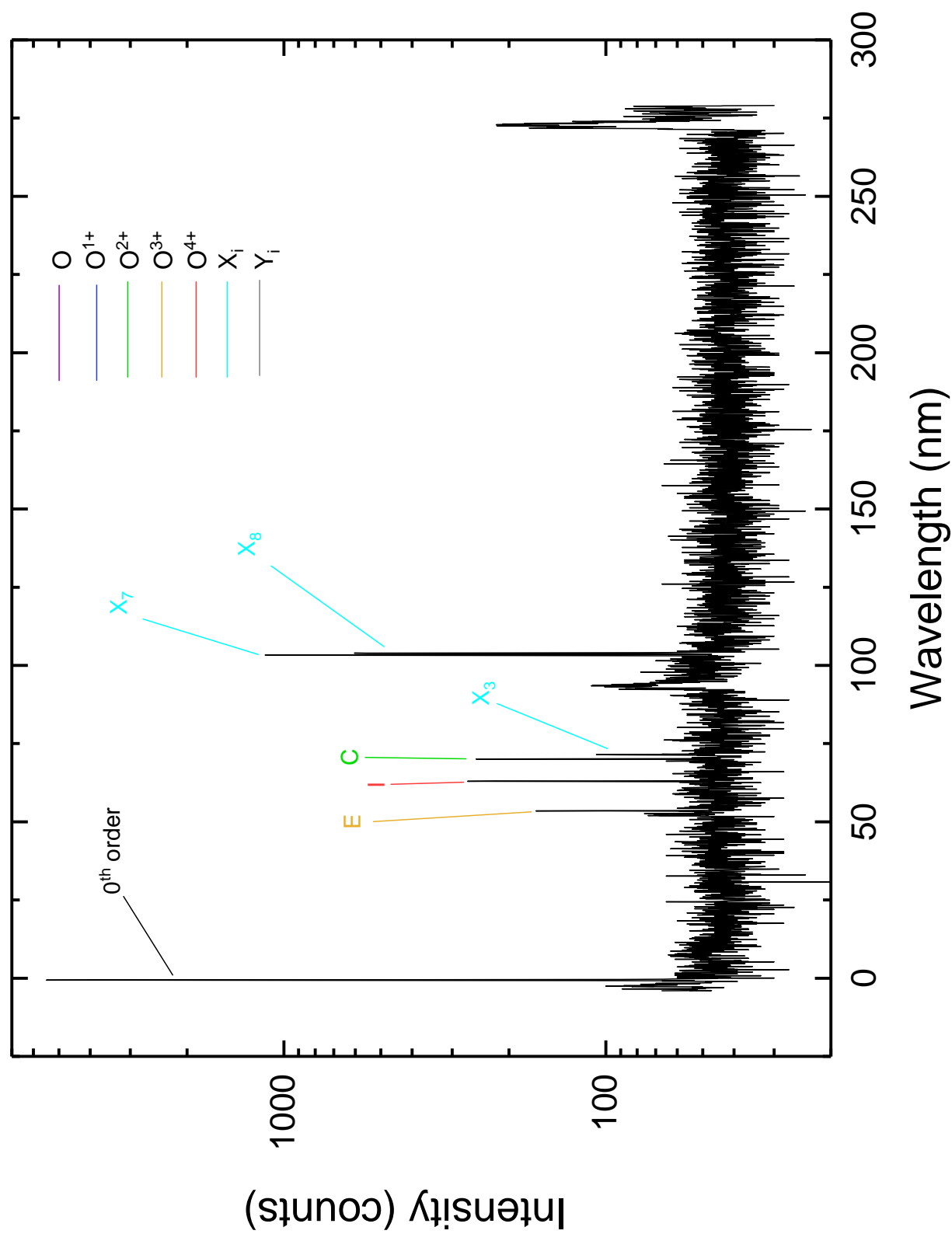
Figure 47: Background spectrum at an electron beam energy of 150 eV.

Figure 48: Spectrum of oxygen at an electron beam energy of 170 eV. Intensity displayed logarithmically.

Figure 49: Spectrum of oxygen at an electron beam energy of 180 eV. Intensity displayed logarithmically.

Figure 50: Spectrum of oxygen at an electron beam energy of 190 eV. Intensity displayed logarithmically.

References

[1] I. Newton, *Opticks, or, a treatise of the reflections, refractions, inflections & colours of light.* Courier Corporation, 1952.

[2] W. H. Wollaston, "Xii. a method of examining refractive and dispersive powers, by prismatic reflection," *Philosophical transactions of the Royal Society of London*, vol. 92, pp. 365–380, 1802.

[3] "Spectroscopy in astronomy." "https://cnx.org/contents/1f92a120-370a-4547-b14e-a3df3ce6f083@3".

[4] G. Kirchhoff and R. Bunsen, "Chemische analyse durch spectralbeobachtungen," *Annalen der Physik*, vol. 186, no. 6, pp. 161–189, 1860.

[5] J. J. Balmer, "Notiz über die spectrallinien des wasserstoffs," *Annalen der Physik*, vol. 261, no. 5, pp. 80–87, 1885.

[6] F. Paschen, "Zur kenntnis ultraroter linienspektra. i.(normalwellenlängen bis 27000 å.-e.)," *Annalen der Physik*, vol. 332, no. 13, pp. 537–570, 1908.

[7] "Ebit history." "https://www.nist.gov/pml/quantum-measurement/atomic-spectroscopy/ebit-history". Accessed: 2018-12-02.

[8] P. Massey and M. M. Hanson, "Astronomical spectroscopy," in *Planets, Stars and Stellar Systems*, pp. 35–98, Springer, 2013.

[9] P. W. Merrill, "Spectroscopic observations of stars of class," *The Astrophysical Journal*, vol. 116, p. 21, 1952.

[10] K. Werner, T. Rauch, E. Ringat, and J. W. Kruk, "First detection of krypton and xenon in a white dwarf," *The Astrophysical Journal Letters*, vol. 753, no. 1, p. L7, 2012.

[11] S. Dreizler and K. Werner, "Spectral analysis of hot helium-rich white dwarfs.," *Astronomy and Astrophysics*, vol. 314, pp. 217–232, 1996.

[12] M. Barstow, J. Holberg, T. Fleming, M. Marsh, D. Koester, and D. Wonnacott, "A rosat survey of hot da white dwarfs in non-interacting binary systems," *Monthly Notices of the Royal Astronomical Society*, vol. 270, no. 3, pp. 499–515, 1994.

[13] K. Werner and J. R. Crespo, "Search for technetium in extremely hot evolved stars."

[14] J. Gillaspy, *Trapping highly charged ions: Fundamentals and applications.* Nova Publishers, 2001.

[15] W. Demtröder, *Experimentalphysik 3: Atome, Moleküle und Festkörper.* Springer-Verlag, 2016.

[16] J. D. Gillaspy, "Highly charged ions," *Journal of Physics B: Atomic, Molecular and Optical Physics*, vol. 34, no. 19, p. R93, 2001.

[17] M. L. Täubert, "Extreme ultraviolet spectroscopy of highly charged ruthenium ions," 2017.

[18] M. Bartelmann, *Theoretical astrophysics: an introduction.* John Wiley & Sons, 2013.

[19] S. Bernitt, J. R. Crespo López-Urrutia, and W. Quint, *Resonante Anregung astrophysikalischer Röntgen-Übergänge in hochgeladenen Eisenionen mit dem Freie-Elektronen-Laser LCLS.* PhD thesis, Ruprecht-Karls-Universität Heidelberg, 2013.

[20] O. Soria *et al.*, "Isotopic effect in b-like an be-like argon ions," 2005.

[21] C. Shah, *Measuring and modeling of anisotropic and polarized x-ray emission following resonant recombination into highly charged ions.* PhD thesis, 2016.

[22] S. Dobrodey, *Untersuchung von K-LL-Resonanzen dielektronischer Rekombination und simultaner Innerschalen-Vakuum-Ultraviolett Übergänge in hochgeladenem Eisen mit einer Elektronenstrahl-Ionenfalle.* PhD thesis, Ruprecht-Karls-Universität Heidelberg, 2014.

[23] S. Epp, J. R. Crespo López-Urrutia, and M. F. DeKieviet, *Röntgen-Laserspektroskopie hochgeladener Ionen in einer EBIT am Freie-Elektronen-Laser FLASH.* PhD thesis, Ruprecht-Karls Universität Heidelberg, 2007.

[24] T. Baumann, *Spektroskopische Untersuchungen resonanter Rekombinationsprozesse an hochgeladenem Silizium in einer Elektronenstrahl-Ionenfalle.* PhD thesis, 2012.

[25] L. Brillouin, "A theorem of larmor and its importance for electrons in magnetic fields," *Physical Review*, vol. 67, no. 7-8, p. 260, 1945.

[26] G. Herrmann, "Optical theory of thermal velocity effects in cylindrical electron beams," *Journal of Applied Physics*, vol. 29, no. 2, pp. 127–136, 1958.

[27] G. Liang, T. Baumann, J. C. López-Urrutia, S. Epp, H. Tawara, A. Gonchar, P. Mokler, G. Zhao, and J. Ullrich, "Extreme-ultraviolet spectroscopy of fe vi-fe xv and its diagnostic application for electron beam ion trap plasmas," *The Astrophysical Journal*, vol. 696, no. 2, p. 2275, 2009.

[28] J. A. Samson, "Techniques of vacuum ultraviolet spectroscopy," 1967.

[29] H. Bekker, J. R. Crespo López-Urrutia, and W. Quint, *Optical and EUV spectroscopy of highly charged ions near the 4 f–5s level crossing.* PhD thesis, Ruprecht-Karls-Universität Heidelberg, 2016.

[30] G. Reichardt, T. Noll, I. Packe, P. Rotter, J.-S. Schmidt, and W. Gudat, "Adaption of the bessy i-3m normal incidence monochromators to the bessy ii source," *Nuclear Instruments and Methods in Physics Research Section A: Accelerators, Spectrometers, Detectors and Associated Equipment*, vol. 467, pp. 458–461, 2001.

[31] "Zeeman effect." "https://www.physi.uni-heidelberg.de/Einrichtungen/FP/anleitungen/F44.pdf".

[32] J. Barnstedt, "Advanced practical course: Microchannel plate detectors," *Kepler Center for Astro and Particle Physics*, 2009.

[33] H. E. Committee *et al.*, "Photomultiplier tubes: Basics and applications," 1999.

[34] "National institute of standards and technology." "https://physics.nist.gov/PhysRefData/ASD/lines_form.html".

[35] "Statistics how to." "http://www.statisticshowto.com/adjusted-r2/".

[36] A. Wilkinson and A. McNaught, "Iupac compendium of chemical terminology, (the" gold book")," *International Union of Pure and Applied Chemistry*, 1997.

[37] Scofield ,J., "Ionization Energies," *LLNL Internal Report*, 1975.

[38] "National institute of standards and technology." "https://physics.nist.gov/PhysRefData/ASD/ionEnergy.html".

[39] M. F. Gu, "The flexible atomic code," *Canadian Journal of Physics*, vol. 86, no. 5, pp. 675–689, 2008.

[40] "The atomic line list v2.04." "http://www.pa.uky.edu/~peter/atomic/query.cgi".

Acknowledgments

Erklärung

Ich versichere, dass ich diese Arbeit selbstständig verfasst und keine anderen als die angegebenen Quellen und Hilfsmittel benutzt habe.

Heidelberg, den 28. Februar 2018